The Characterization of Deep Convection in the Tropical Tropopause Layer Using Active and Passive Satellite Observations

A Thesis
Presented to
The Academic Faculty

By

Alisa H. Young

In Partial Fulfillment of the
Requirements for the
Degree of Doctor of Philosophy in the
School of Earth and Atmospheric Sciences

School of Earth and Atmospheric Sciences
Georgia Institute of Technology
August 2011

The Characterization of Deep Convection in the Tropical Tropopause Layer Using Active and Passive Satellite Observations

Approved by:

Dr. Judith A. Curry, Advisor
School of Earth and Atmospheric Science
Georgia Institute of Technology

Dr. Robert X. Black
School of Earth and Atmospheric Science
Georgia Institute of Technology

Dr. Irina N. Sokolik
School of Earth and Atmospheric Science
Georgia Institute of Technology

Dr. John J. Bates
Remote Sensing and Applications Division
NOAA/NESDIS/NCDC

Dr. Peter J. Webster
School of Earth and Atmospheric Science
Georgia Institute of Technology

Date Approved: June 23, 2011

ACKNOWLEDGEMENTS

I am deeply grateful for all the time, energy, and guidance of my advisors Dr. Judith A. Curry and Dr. John J. Bates. While the development of this thesis has at times been very challenging, this body of work is not only the result of my steadfastness but it is also the result of your own persistence and diligence in carefully guiding me to become a better scientist and researcher.

I would also like to thank Dr. Irina N. Sokolik, who has also given much of her time and expertise to me through classroom instruction and memorable group meetings. For guidance especially in the earlier stages of my thesis work, I would like to thank Zhengzhao (Johnny) Lou, who provided valuable insight on CloudSat measurements. I also acknowledge Karen Rosenlof, who graciously provided observations that were needed for several of the analysis presented in Chapter 5. To Priti Brahma and Yassin Jeilani, thank you both for helping me to work through many of the professional challenges I have faced. Your wisdom and encouragement has helped me to better understand and also conquer difficult barriers. I am also indebted to Lei Shi and Ken Knapp, who were very helpful in the early phases of my thesis work.

Finally, I would like to thank my heavenly father, for the favor that He has given me. I would also like to thank my beloved family, Alphanso Young, Alphanso Young Jr., and Reagan M. Young for their love and support while I have worked to complete my doctoral degree. In addition, I would also like to thank my father and mother, John and Desiree Holley and siblings, David, Tamar, and Dannon for their continued guidance, love, and support.

TABLE OF CONTENTS

LIST OF TABLES

LIST OF FIGURES

LIST OF ABBREVIATIONS

Ac	Altocumulus
As	Altostratus
AIRS	Atmospheric Infrared Sounder
AR1	Assessment Report 1
AR2	Assessment Report 2
AR3	Assessment Report 3
AR4	Assessment Report 4
AVHRR	Advanced Very High Resolution Radiometer
AMSU	Atmospheric Microwave Sounding Unit (-A)
BT	Brightness Temperature
$BT_{6.7}$	Infrared Water Vapor Brightness Temperatures at 6.7 μm
BT_{11}	Infrared Brightness Temperatures at 11 μm
BTD	Brightness Temperature Difference
GCM	Global Climate Model
CALIPSO	Cloud-Aerosol Lidar and Infrared Pathfinder Satellite Observations
CAPE	Convective Available Potential Energy
Cb	Deep Convective
CBL	Convective Boundary Layer
CERES	Clouds and the Earth's Radiant Energy System
Ci	Cirrus
CPR	Cloud Profiling Radar (CloudSat)
CPT	Cold Point Tropopause
Cu	Cumulus
dBZe	Decibels of Reflectivity
DJF	December-January-February
EL	Equilibrium Level
HALOE	Halogen Occultation Experiment
HIRS	High Resolution Infrared Sounder
IPCC	Intergovernmental Panel on Climate Change
IR	Infrared
IRW	Infrared Window
IRWBT	Infrared Window Brightness Temperature
IRWVBT	Infrared Water Vapor Brightness Temperature
ISCCP	International Satellite Cloud Climatology Project
ITCZ	Intertropical Convergence Zone
JJA	June-July-August
LIS	Lightning Imaging Sensor (LIS)
LNB	Level of Neutral Buoyancy
LRT	Lapse Rate Tropoppause
LSWV	Lower Stratospheric Water Vapor
LW	Longwave
LWP	Liquid Water Path
MAM	March-April-May
MLS	Microwave Limb Sounder

MODIS	Moderate Resolution Infrared Sounder
NCDC	National Climatic Data Center
NOAA	National Oceanic and Atmospheric Administration
Ns	Nimbostratus
ppmv	parts per million volume
PR	Precipitation Radar
Qclear	Level of zero radiative heating
QBO	Quasi-biennial Oscillation
Sc	Stratocumulus
SON	September-October-November
St	Stratus
SW	Shortwave
SWV	Stratospheric Water Vapor
SST	Sea Surface Temperature
STEP	Stratospheric Tropospheric Exchange Project
TOGA COARE	Tropical Ocean Global Atmosphere Coupled Ocean Atmosphere Response Experiment
TMI	Tropical Rainfall Monitoring Mission Microwave Imager
TRMM	Tropical Rainfall Monitoring Mission
TTL	Tropical Tropopause Layer
UARS	Upper Atmospheric Research Satellite
UT/LS	Upper Tropospheric/Lower Stratospheric
VIRS	Visible Infrared Scanner
WS1	Weather State 1

LIST OF SYMBOLS

α	Alpha value; a number between 0 and 1 such that $p \leq \alpha$ is considered significant where p is a p-value.
τ	Cloud optical depth
μm	Micrometer
$\hat{\phi}_N$	Autocorrelation of the noise, N
$\hat{n}*$	Number of years to detect trend at the 95% significance level according to Weatherhead et al., [1998]
$\hat{\sigma}_N$	Standard deviation of noise, N.
p-value	Probability of obtaining a test statistic at least as extreme as the one that was actually observed, assuming that the null hypothesis is true.

SUMMARY

Several studies suggest that deep convection that penetrates the tropical tropopause layer may influence the long-term trends in lower stratospheric water vapor. This thesis investigates the relationship between penetrating deep convection and lower stratospheric water vapor variability using historical infrared (IR) observations. However, since infrared observations do not directly resolve cloud vertical structure and cloud top height, and there has been some debate on their usefulness to characterize penetrating deep convective clouds, CloudSat/Calipso and Aqua MODIS observations are first combined to understand how to best interpret IR observations of penetrating tops.

The major findings of the combined CloudSat/Calipso and Aqua MODIS analysis show that penetrating deep convection predominantly occurs in the western tropical Pacific Ocean. This finding is consistent with IR studies but is in contrast to previous radar studies where penetrating deep convective clouds predominantly occur over land regions such as equatorial Africa. Estimates on the areal extent of penetrating deep convection show that when using IR observations with a horizontal resolution of 10 km, about two thirds of the events are large enough to be detected. Evaluation of two different IR detection schemes, which includes cold cloud features/pixels and positive brightness temperature differences (+BTD), show that neither schemes completely separate between penetrating deep convection and other types of high clouds. However, the predominant fraction of +BTD distributions and cold cloud features/pixels $\leq$ 210 K is due to the coldest and highest penetrating tops as inferred from collocated IR and radar/lidar observations. This result is in contrast to previous studies that suggest the majority of cold cloud features/pixels $\leq$ 210 K are cirrus/anvil cloud fractions that coexist with deep convective clouds. Observations also show that a sufficient fraction of penetrating deep

convective cloud tops occur in the extratropics. This provides evidence that penetrating deep convection should be documented as a pathway of stratospheric-tropospheric exchange within the extratropical region.

Since the cold cloud feature/pixel ≤ 210 K approach was found to be a sufficient method to detect penetrating deep convection it was used to develop a climatology of the coldest penetrating deep convective clouds from GridSat observations covering years 1998-2008. The highest frequencies of the coldest penetrating deep convective clouds consistently occur in the western-central Pacific and Indian Ocean. Monthly frequency anomalies in penetrating deep convection were evaluated against monthly anomalies in lower stratospheric water vapor at 82 mb and show higher correlations for the western-central Pacific regions in comparison to the tropics. At a lag of 3 months, the combined western-central Pacific had a small but significant anticorrelation, where the largest amount of variance explained by the combined western-central Pacific region was 8.25%. In conjunction with anomalies in the 82 mb water vapor mixing ratios, decreasing trends for the 1998-2008 period were also observed for tropics, the western Pacific and Indian Ocean. Although none of these trends were significant at the 95% confidence level, decreases in the frequency of penetrating deep convection over the 1998-2008 shows evidence that could explain in part some of the 82 mb lower stratospheric water vapor variability.

CHAPTER 1

INTRODUCTION

1.1 Introduction and Review

According to the cold trap hypothesis, tropical tropopause temperatures largely control the annual and inter-annual variability of lower stratospheric water vapor. However, studies using balloon-borne [Oltmans et al., 2000] and satellite observations [Rosenlof et al., 2001; Randel et al., 2006; Solomon et al., 2010] show multi-decadal trends in lower stratospheric water vapor from 1980-2009 that are inconsistent with trends in tropical tropopause temperatures for the same periods. Using radiative transfer models, these trends have been evaluated and were shown to considerably impact surface climate [Forster and Shine, 2002; Solomon et al., 2010]. These trends are still largely unexplained. It therefore remains important to evaluate cross tropopause transport via episodes of strong convection, since several studies provide evidence (e.g., Chaboureau et al., 2007; Corti et al., 2008; Khaykin et al., 2009; Wang et al., 2009) that this type of deep convection impacts the lower stratospheric water vapor budget and as suggested by Rosenlof and Reid [2008] may influence long-term trends in lower stratospheric water vapor variability.

To address the role of deep convection on lower stratospheric water vapor, several studies have monitored deep convection reaching the gate to the lower stratosphere, known as the tropical tropopause layer (TTL). While this approach provides useful approximations on frequency and regional dominance, the only existing observations that may be used to address the influence of strong convection on long-term (1980─2009) lower stratospheric water vapor variability are based on historical passive sensor satellite radiances. It has been challenging to use observations from passive sensors to quantify this relationship for two reasons. Firstly, deep

convective clouds penetrating the TTL contain overshooting deep convection with diameters of 1─10 km. It is unclear how well historical observations with a horizontal resolution of 10 km may resolve these events. Secondly, observations from passive sensors do not directly resolve cloud vertical structure and cloud top height. When compared with radar observations that do provide evidence of cloud vertical structure, active and passive observations yield different results (e.g. Alcala and Dessler, 2002 vs. Gettelman et al., 2002). Addressing both these issues is important to better understand the information content that the historical observations may provide.

Given these details, this thesis evaluates deep convection penetrating the TTL using radar and IR observations to explore the hypothesis that penetrating and overshooting deep convection has a strong influence on lower stratospheric water vapor variability. More specifically, CloudSat/Calipso and Aqua MODIS are used to 1) obtain a statistically robust sample of penetrating deep convection and evaluate areal extent to determine how well penetrating deep convection may be resolved from IR sensors (Chapter 3); 2) quantitatively compare IR and radar distributions of penetrating deep convection using traditional IR techniques to determine the extent to which traditional IR techniques capture penetrating deep convection (Chapter 4) and 3) considering the uncertainty of traditional IR techniques, this thesis also examines the spatiotemporal variability of penetrating and overshooting deep convection from 11 years (1998─2008) of GridSat observations to address the role of penetrating deep convection in lower stratospheric water vapor variability (Chapter 5).

The following sections of this introductory chapter further frame the thesis hypothesis by describing known factors that control lower stratospheric water vapor in Section 1.2. In Section 1.3 the climate impacts of lower stratospheric water vapor variability are described. Section 1.4

provides details of penetrating deep convection and the TTL, and Section 1.5 gives an outline of how the hypothesis of thesis work is explored in the remaining chapters.

1.2 Water Vapor in the Stratosphere

Water vapor is a key climate variable. It is the most abundant green house gas and is largely found in the lowermost part of the atmosphere, known as the troposphere. Water vapor comprises between 0–0.4% of the atmosphere's gaseous composition by volume and exists in concentrations that vary as a function of height, latitude, and temperature. Unlike other greenhouse gases that warm Earth's atmosphere and surface, the amount of atmospheric water vapor directly associated with anthropogenic sources is negligible. The predominant source of atmospheric water vapor is evaporation from land and ocean surfaces. Atmospheric water vapor concentration is limited by the saturation specific humidity, which is nearly an exponential function of temperature; as temperature decreases with height in the free troposphere, the mean concentration of water vapor decreases exponentially.

Water vapor in the region above the troposphere, known as the stratosphere, is therefore low (e.g., < 5 parts per million by volume (ppmv)). The water vapor content of the stratosphere is largely a function of tropical tropopause temperatures whereby air passing through the tropical tropopause is dehydrated to the region's local minimum saturation mixing ratio [Brewer, 1949; Fluegistaler et al., 2005; Sherwood and Dessler, 2000]. Other factors controlling water vapor in the stratosphere include methane (CH_4) oxidation and in the lower stratosphere it is also controlled by cross-tropopause transport. The variability of water vapor in the lower stratosphere is of particular concern in this thesis because despite its low concentration, water vapor in this region, contributes disproportionately to the natural greenhouse effect. To illustrate this disproportionality, Solomon et al. [2010] show that for a uniform change of 1 ppmv in 1-km

vertical layers, the adjusted total radiative forcing of surface climate is maximized between the tropical upper troposphere and lower stratospheric regions lying between 14 and 18 km. Thus, small spatiotemporal changes in the concentration of water vapor between 14 and 18 km may considerably impact surface climate. For the upper tropospheric region, these impacts were shown by Sohn and Schmetz [2004]. For the lower stratospheric region, where water vapor has a lifetime of ~ 1 year, these impacts were shown by Solomon et al. [2010], Forster and Shine [2002,] and Shindell et al. [2005]. Given these details, it is important to better evaluate the factors that may be controlling long-term variability of lower stratospheric water vapor. More details of this variability and its impact on climate are provided below.

1.3 Climate Impacts of Lower Stratospheric Water Vapor Variability

While the major processes controlling stratospheric water vapor are understood, the long-term variability in lower stratospheric water vapor has not been explained. Oltmans et al. [2000] used a time series of balloon-borne frost point hygrometer measurements over Boulder, CO, from 1981─2000 and showed upward trends in lower stratospheric water vapor of ~1% per year, totaling ~ 1ppmv. Rosenlof et al. [2001] report a comparable trend that spanned a 40-year period using a combination of datasets. Solomon et al. [2010] also showed a decrease of ~ 0.4 ppmv in lower stratospheric water vapor between 2000 and 2009. However, corresponding trends in tropical tropopause temperatures were not observed for each of these periods [Randel et al., 2004; SPARC, 2000].

Solomon et al. [2010] used a line-by-line radiative transfer model to calculate the radiative impact of the 1980-2009 lower stratospheric water vapor changes. The authors suggest that when compared with the radiative forcing due to carbon dioxide, aerosols, and other greenhouse gases, the 1980─2000 increase of ~ 1-ppmv acted to enhance the decadal rate of

surface warming by 30%, while post-2000 decreases of ~ 0.4 ppmv may have slowed the rate of surface warming by 25%.

In the Intergovernmental Panel on Climate Change (IPCC) third and fourth assessment reports, AR3 and AR4 respectively, the IPCC acknowledge that several studies show long-term trends in stratospheric water vapor between 1980 and 2000. The IPCC also state that these trends would have a significant radiative impact. However, in AR3 and AR4, CH_4 oxidation is the only source of the 1980─2000 trend considered to be a radiative forcing component.

In the illustration of Radiative Forcing components provided by AR4 of the IPCC, the radiative forcing components from natural and anthropogenic sources are provided. according to that information, the fraction of anthropogenic stratospheric water vapor changes due to methane oxidation was estimated to contribute a radiative forcing of +0.07 W m^{-2} (0.02 ─0.12 W m^{-2}) based on results from Hansen et al. [2005] (Smith et al., 2001). Stratospheric water vapor changes unattributable to methane oxidation were not considered because there is a low understanding of the processes that modulate those changes and there is a lack of scientific consensus regarding its treatment. More specifically, it is not clear if lower stratospheric water vapor changes are due to anthropogenic impacts or if they are due to natural variability, which includes changes in tropical tropopause temperatures or dynamics. The latter is also modulated by anthropogenic warming [Webster et al., 2006].

In comparison to the radiative forcing of +0.07 W m^{-2} reported by Hansen et al., [2005], Forster and Shine [2002] show that the 1 ppmv change from 1980─2001 result in a radiative forcing of +0.29 W m^{-2}. This radiative forcing significantly differs from results reported by Hansen et al. [2005]. Radiative forcing values reported by Forster and Shine [2002] are also consistent with Solomon et al. [2010] who report that the 1980-2000 1ppmv change resulted in a

radiative forcing of +0.24 W m^{-2}.

Regarding the decrease of ~ 0.4 ppmv between 2000─2009, Solomon et al. [2010] suggests that this change led to a radiative forcing of -0.098 W m^{-2}. The authors also suggest that this negative forcing, which effectively cools the surface climate, provides some explanation of why global surface temperature rise has slowed in the last decade despite a steady increase in radiative forcing from CO_2 emissions. Thus, a better understanding of the physical processes controlling changes in the concentration of stratospheric water vapor is a vital prerequisite to accurately project future climate change. It is necessary to question: *What other processes impact lower stratospheric water vapor? Are changes in lower stratospheric water vapor due to global warming and climate change?*

While several different sources likely contribute to lower stratospheric water vapor variability, the amount from each source is difficult to quantify. A direct source of water vapor into the lower stratosphere is from aviation [IPCC, 2007]; while other pathways that may alter lower stratospheric water vapor are related to stratospheric chemistry and include changes to methane oxidation rates due to changes in the concentration of stratospheric chlorine, ozone, and the hydroxyl radical [Röckmann et al., 2004]. Other proposed mechanisms relate to changes in tropopause temperatures or circulation [Stuber et al., 2001; Fueglistaler et al., 2004] and cross-tropopause transport [Danielsen, 1993; Rosenlof, 2003; Randel et al., 2004, Chaboureau et al., 2007; Wang, 2009].

The most likely factors associated with cross-tropospheric transport include slow or gradual ascent of water vapor by large-scale motion and turbulent diffusion and rapid ascent by strong convection or volcanic eruption [Joshi and Shine, 2003]. The latter pathway and its association with strong convection is supported by observations of deep convection reaching 18

km (e.g., Alcala and Dessler, 2002) and evidence of tropical tropopause layer and lower stratospheric hydration by ice crystals lofted from deep convection [Corti et al., 2008]. This is the source of lower stratospheric water vapor variability addressed in this thesis. More details associated with this pathway are addressed in the following section.

1.4 Deep Convection in the TTL

Overshooting deep convection occurs when cumulonimbus clouds with strong updrafts protrude their level of neutral buoyancy (LNB). The LNB is the height at which an air parcel is no longer more buoyant than the environment because the air parcel's temperature is equal to the environmental temperature. The overshooting cloud top (see Figure 1.1), which has enough momentum to extend above the LNB, appears as a dome shaped structure rising from the anvil cloud and can occur with any cumulonimbus cloud when atmospheric instability, usually estimated by convective available potential energy (CAPE), is high. Although the term, 'overshooting deep convection' is thermodynamically dependent on the cumulonimbus cloud's ability to overcome its LNB, overshooting deep convection investigated in many research studies (e.g., Rossow and Pearl, 2007; Liu and Zipser, 2005; Gettelman et. al., 2002) are also associated with penetrating deep convection that reach and extend up into the base of the tropical tropopause layer (~14 km). From a technical perspective it is important to note that not all penetrating deep convection belong to the class of overshooting tops, but all overshooting tops do belong to the class of penetrating deep convection.

Penetrating and overshooting deep convection, which are classified in this thesis as deep convective clouds with cloud tops ≥ 14 km, are most often found within the tropics due to equatorial convergence of the northeasterly and southeasterly trade winds and high surface temperatures. More specifically, equatorial convergence of the northeasterly and southeasterly

trade winds cause low-level air to converge, forming low pressure systems associated with the thermally direct equatorial branch of the Hadley cell (meridional) and Walker (zonal) circulations [Riehl, 1979]. These circulations also produce a seasonally migrating band of low pressure systems that are most commonly referred to as the intertropical convergence zone (ITCZ) which is positioned slightly south of the equator in January and near 15°N in July.

As shown in Figure 1.1, overshooting deep convection rises from the convective boundary layer (CBL) into the tropical tropopause layer (TTL), the cold point tropopause (CPT) and possibly into the lower stratosphere. Air within the TTL has tropospheric and stratospheric characteristics. As shown by Folkins et al. [1999], the TTL is the region just below the cold point tropopause where ozone starts to increase due to inefficient mixing of air from deep convection and it also marks enhanced stratification according to the environmental lapse rate. The TTL is the transition zone between ~14 km and 17 km where air starts to assume some of the chemical characteristics of stratospheric air. It is maintained by the interaction of convective transport, convectively generated waves (i.e., gravity waves), radiation, cloud microphysics, and the large-scale stratospheric circulation [Gettleman et al., 2008]. As described by Fueglistaler et al. [2009], the TTL acts as a "gate to the stratosphere" for atmospheric tracers such as water vapor and so-called very-short-lived substances. By evaluating the frequency of deep convection reaching this "gate," it may enable us to answer unresolved questions regarding the role of penetrating deep convective clouds in long-term changes in lower stratospheric water vapor.

Barrett et al. [1973] was one of the first to link deep convection within mesoscale convective systems with upper tropospheric/lower stratospheric water vapor exchange. Such linkages were established using water vapor infrared radiometric measurements made from a U-2 aircraft that flew around and over two penetrating thunderstorms in the southwestern United

States. Barrett et al. conclude that a significant fraction of thunderstorms in the plains and southwest of the U.S. penetrate the tropopause and deposit significant amounts of water vapor in the stratosphere near and downwind of their tops.

Johnston and Solomon [1979] and Danielsen [1982; 1993] hypothesized that an overshooting top's fate as a source or sink to lower stratospheric water vapor strongly depends on the fate of ice particles, observed to exist in high number densities [Knollenberg et al., 1993], within the overshoot. It is suggested that these particles are either hydrate (i.e., add water vapor) or dehydrate (i.e., remove water vapor) the lower stratosphere. In the case of hydration, moistening occurs when ice-crystal-laden air within the overshoot entrains warmer stratospheric air that raises the temperature of the overshoot. The ice crystals sublimate and the layer becomes more hydrated. In the case of dehydration, radiatively driven overturning of ice-crystal-laden air within the overshoot facilitates the growth of ice crystals through vapor deposition. Once the ice crystals become large enough, gravitational settling occurs and the final state of the layer is drier than its initial state.

While most of the early in situ measurements supported the hypothesis that overshooting tops would hydrate the lower stratosphere, it is still unclear whether hydration or dehydration globally dominates. Moreover, the existence of upper tropospheric/lower stratospheric sub-saturated and super-saturated conditions further complicates the problem. Jensen et al. [2007] found no evidence to support the hypothesis that overshooting deep convection can dehydrate the tropical tropopause layer when it is initially sub-saturated with respect to ice. The distribution of supersaturated regions was shown by Gettelman et al. [2006]. However, more observational data is needed to understand the mechanics of overshooting deep convection that penetrate these different regions.

Boering et al. [1995] argue that the input of significant amounts of overshooting tropospheric air above the tropical tropopause is unlikely since it would undermine the seasonal variation in CO_2 propagating upward from the tropopause. However, model simulations suggest that this is not true in all scenarios [Dessler and Sherwood, 2003]. Field experiments with isotopic measurements strongly indicate overshooting deep convection, advection, and microphysics all crucial to the stratospheric water budget [Donner et al., 2007]. In addition, Rosenlof and Reid [2008] focused on sea surface temperatures in the so-called warm pool region of the western tropical Pacific Ocean. They conclude that the underlying ocean can have a fairly direct influence on the lower tropical stratosphere. Without quantitative evidence, they also speculate that the connecting link between lower stratospheric water vapor variability and sea surface temperatures in the tropical western Pacific Ocean is probably deep convective towers. Tseilodius et al. [2010] report that analysis of the time series of convective clouds penetrating into the lower stratosphere did not show any significant long term trends. The authors conclude that the influence of convection on stratospheric water vapor trends comes from the overall moistening of the tropical upper troposphere rather than from direct transport of convection penetrating the lower stratosphere. However, their result is somewhat questionable according to the spatial resolution of the ISCCP D1 observations used in their study.

While several field experiments [Thunderstorm Project, Stratospheric Tropospheric Exchange Project (STEP), Tropical Ocean Global Atmosphere Coupled Ocean Atmosphere Response Experiment (TOGA COARE)] provide detailed information on tropical deep convective clouds, these localized studies do not offer a comprehensive picture of the annual and inter-annual variability of penetrating deep convection throughout the tropics. To gain this view, observations from space-borne passive sensor satellite radiometers are used. For these

observations, two approaches are commonly used to evaluate the frequency and distribution of penetrating/overshooting deep convection from passive sensors. They include cold cloud features (e.g., Mapes and Houze, 1993; Liu et al., 2007; Rossow and Pearl, 2007) derived from ~11 μm brightness temperatures, and positive brightness temperature differences (+BTD) between the water vapor absorption band at ~6.7 μm and the IR window at ~11 μm (e.g., Schmetz et al., 1997; Soden, 2000; Setvak et al., 2003; 2007; Chung et al., 2008). While these techniques have been used to show the seasonality and regional dominance of penetrating deep convective clouds, passive sensor satellite observations do not provide cloud vertical structure and the extent to which these techniques are able to sample penetrating deep convective clouds with diameters of 1-10 km is unclear (Fujita, 1982). Furthermore when IR based distributions of penetrating deep convection were compared with radar observations that do provide evidence of cloud vertical structure, active and passive observations yield different results (e.g., Alcala and Dessler, 2002 and Gettelman, 2002). Addressing both these issues is important to better understand the information content that the historical observations may provide.

Given that passive sensor studies use infrared (IR) cloud brightness temperatures and active sensor studies rely on rather direct measurements of cloud vertical structure, radar observations are used to better interpret the extent to which deep convective clouds penetrating the TTL are sampled from IR observations. Liu et al. [2007] provide the first study to evaluate deep convection penetrating the TTL from radar and IR using the Tropical Rainfall Monitoring Mission (TRMM) Precipitation Radar (PR). However, this instrument is designed to observe cloud vertical structure as determined by its sensitivity to precipitation size particles. This proves problematic for penetrating deep convection reaching the TTL since its occurrence is critically determined by cloud top structure most often characterized by the distribution of cloud

size particles within the cloud top. In contrast to the TRMM PR, the CloudSat Cloud Profiling Radar is sensitive to cloud particles. Furthermore, the combination of CloudSat with Cloud-Aerosol Lidar and Infrared Pathfinder Satellite Observations (CALIPSO), which provide a more highly resolved description of cloud top height, and IR observations from the Aqua Moderate Resolution Infrared Sounder (MODIS) yield retrievals of penetrating deep convective clouds superior to retrievals from any one or two instruments.

1.5 Exploring Hypothesis

This thesis evaluates deep convection penetrating the TTL using radar and IR observations to explore the hypothesis that penetrating and overshooting deep convection has a strong influence on lower stratospheric water vapor variability. An overview of how this hypothesis is explored is provided below.

1.5.1 Overview of CloudSat, Calipso, and Aqua-MODIS Data Products

Collocated measurements from CloudSat, Calipso, and Aqua-MODIS enable satellite-based radar, lidar, and passive remote sensing measurements to be used in concert to better detect and characterize penetrating and overshooting deep convection. However, these instruments and their corresponding products are relatively new and the benefits of CloudSat vs. TRMM observations may not be clear. In Chapter 2, the strengths and weaknesses of the CloudSat Cloud Profiling Radar are compared to the Tropical Rainfall Monitoring Mission (TRMM) Precipitation Radar to identify the potential insight CloudSat may provide in comparison to TRMM. In addition, CloudSat/Calipso and Aqua MODIS data products are described to clearly outline how these datasets advance this research. CloudSat products described in Chapter 2 include 2B-GEOPROF, 2B-Lidar-GEOPROF, and 2B-CLDCLASS products. MODIS products include CloudSat developed MODIS-AUX (Aqua MODIS LIB

product) and MAC06S0 (Aqua MODIS L2 Cloud Product) products.

1.5.2 Characterization of Penetrating Deep Convection

In Chapter 3, an overview is given of TRMM and CloudSat studies that have characterized penetrating and overshooting deep convective clouds. After evaluating the limitations of these studies, CloudSat and Calipso data products are used to capture penetrating and overshooting deep convection that reach the base of the tropical tropopause layer (~14 km). The observations are characterized by cloud top height, cloud base height, maximum reflectivity, areal size distribution, seasonality, and spatial frequency distribution. CloudSat and Calipso detections of penetrating and overshooting deep convection are also combined with Aqua MODIS products to evaluate penetrating deep convective clouds using traditional IR techniques. As described in Section 1.4 these techniques include the cold cloud feature/pixel technique and the +BTD signature. Results obtained in Chapter 3 provide a statistically robust characterization of penetrating and overshooting deep convection from radar and IR observations. The observations of penetrating deep convection provided in this chapter are also used to estimate the areal size distribution of penetrating deep convective clouds. The areal size distribution of penetrating tops is needed to determine the extent to which historical IR observations, with 10 km resolution, are able to resolve this particular type of cloud.

1.5.3 Evaluation of Traditional IR Techniques

Observations of cold cloud features and positive BTD signatures are compared with penetrating deep convective clouds that were gathered in Chapter 3. The comparison of these three different sets of observations are used to statistically characterize the extent to which traditional passive sensor approaches are able to exclusively capture overshooting deep convection and to evaluate, to the extent possible, the percentage of other types of high level

clouds (i.e., anvil clouds, pileus clouds, jumping cirrus, lower level deep convection, etc.) that may be present in the IR distributions. In addition, Chapter 4 also compares the microphysical and optical properties of penetrating deep convection with other types of high clouds. By evaluating these properties the capabilities and information content of IR-based distributions of penetrating deep convection are better understood and their capability to detect penetrating deep convective cloud tops is revealed. The results gathered in Chapter 4 are then used to quantitatively characterize the relationship between cold cloud features and observations of penetrating deep convective clouds. These results are used in Chapter 5 to develop a climatology of penetrating and overshooting deep convective cloud tops.

1.5.4 Climatology of Penetrating Deep Convection

In Chapter 5, cold cloud pixels and positive BTD signatures are evaluated from GridSat observations covering the period between 1998 and 2008 to develop a climatology of penetrating deep convective cloud tops. GridSat observations that have been derived from the International Satellite Cloud Climatology Project (ISCCP) and developed by the National Climatic Data Center (NCDC) of the National Oceanic and Atmospheric Administration (NOAA) are also described. GridSat observations are especially used in Chapter 5 because they have high temporal resolution, a spatial resolution of ~ 10 km, and unlike Aqua MODIS observations, they provide observations of penetrating deep convective cloud tops that cover the onset of a downward trend in lower stratospheric water vapor that occurred around 2000 [Solomon et al., 2010]. While the diurnal, intraseasonal, and interannual variability of penetrating deep convective cloud tops is evaluated, the major focus of Chapter 5 is to compare the interannual variability of penetrating deep convection with the interannual variability of lower stratospheric water vapor for the 1998-2008 period. By performing this evaluation we

ultimately evaluate the impact of penetrating deep convective cloud tops on lower stratospheric water vapor. This evaluation is first carried out over the entire tropics and separate regional analysis focused on the Indian Ocean, west Pacific, central Pacific, East Pacific, South America, the Atlantic, and Africa.

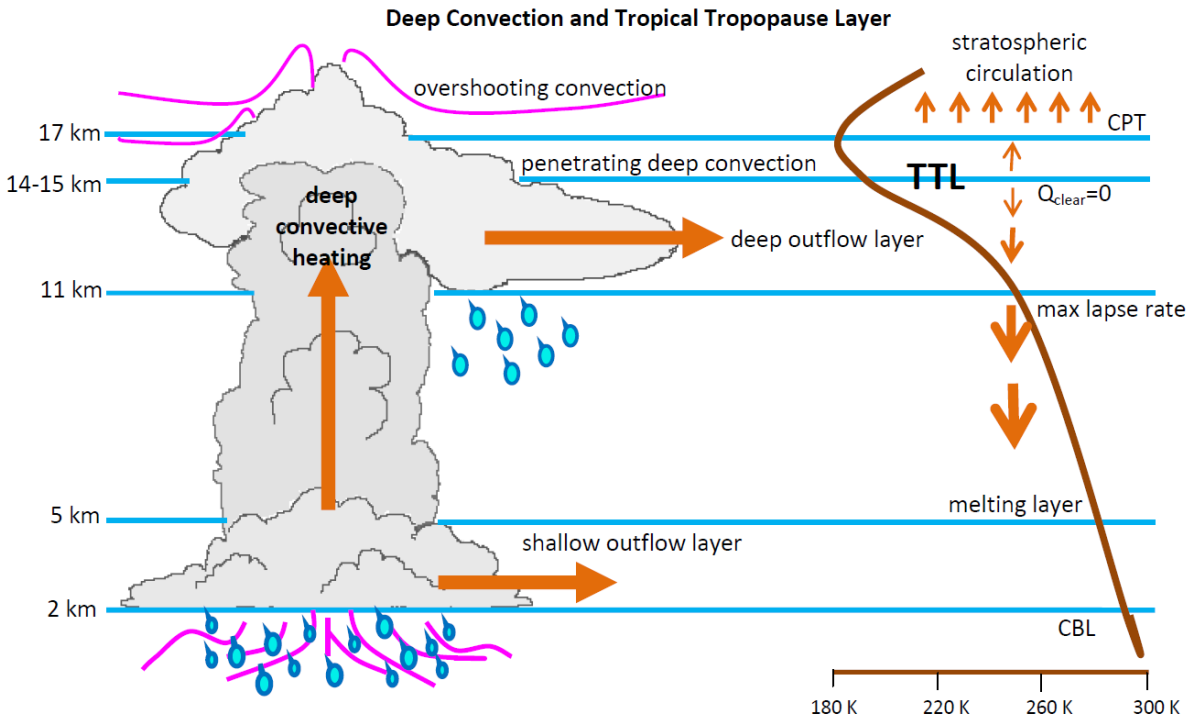

Figure 1.1: Schematic diagram of upward mass flux of tropical overshooting deep convection penetrating from the convective boundary layer (CBL) into the tropical tropopause layer (TTL), cold point tropopause (CPT) and on into the lower stratosphere. The diagram also shows the anvil of the deep convective cloud identified within the deep convection outflow layer located between 11 km and 15 km as well as a shallow outflow layer where shallow convective clouds are primarily detrained. At ~15 km, the level of zero net radiative heating is distinguished as Qclear=0. As indicated by the one directional arrows above and below this level, there is net downward motion associated with clear sky radiative cooling and subsidence just below this level and net radiative heating and upward vertical motion just above this level.

CHAPTER 2
OVERVIEW OF CLOUDSAT, CALIPSO, AND AQUA MODIS DATA PRODUCTS

2.1 Introduction

The TRMM Precipitation Radar has been used to evaluate deep convection reaching the base of the TTL both independently (e.g., Liu et al., 2005) and in conjunction with collocated observations from passive IR sensors (e.g., Alcala et al., 2002; Liu et al., 2007). However, as its name would imply, the TRMM Precipitation Radar is sensitive to precipitation size particles. This sensitivity prevents the TRMM Precipitation Radar from fully resolving the portion of cloud vertical structure that is determined by smaller cloud particles typically found at the boundaries of the cloud, which includes the cloud top. Thus it is important to determine, how observations from the CloudSat Cloud Profiling Radar may be used to provide more details of cloud vertical structure in comparison to the TRMM Precipitation Radar. After comparing CloudSat and TRMM radars in Section 2.2, the remaining sections in this chapter provide details of CloudSat/Calipso and Aqua MODIS observations. The information provided in this chapter outlines how these datasets advance this thesis. It identifies how key observations from these instruments are obtained and clarifies common limitations and concerns.

2.2 Comparison of TRMM and CloudSat Radar Characteristics

The TRMM Precipitation Radar launched in late 1997 and the CloudSat Cloud Profiling Radar launched in April 2006 are the only radars that have operated in space. The technical details of both these radars are provided in Table 2.1, where differences in geographic coverage, temporal resolution, scan characteristics, and radar characteristics are provided.

As indicated in Table 2.1, the TRMM PR has a radar sensitivity of 12 dBZ and operates at a frequency of 13.8 GHz. Given these characteristics, TRMM detects particles with a mean mass diameter of ~ 275 μm [Alcala and Dessler, 2002] and is capable of detecting fairly light to intense rain rates. As such, TRMM has shown exceptional capabilities in characterizing the intensity and distribution of rain, rain type, storm depth, and the height at which snow melts into rain. Although it has also been used to evaluate deep convective clouds reaching the TTL [Alcala and Dessler, 2002; Luo et al., 2005; 2007], the mean mass diameter detectable by TRMM is much larger than the mean mass diameter of ice crystals that have been found in the overshooting tops of deep convective clouds during field studies (e.g., Knollenberg et al., 1993;). The smaller particles that comprise the cloud top must be detected to truly evaluate cloud vertical structure and determine when deep convective clouds penetrate the TTL and potentially modify the lower stratospheric water vapor content.

In comparison to the TRMM PR, the CloudSat Cloud Profiling Radar has a sensitivity of -28 dBZ and operates at a frequency of 94 GHz. These specifications enable CloudSat to detect much smaller sized cloud droplets and ice crystals on the order of ~30 μm. To illustrate the capabilities of CloudSat and TRMM, nearly coincident images of CloudSat and TRMM cross sections of a deep convective cloud centered at 19.85°N, 87.93°W are provided in Figure 2.1 (cf., Li and Schumaker, 2010). As indicated in Figure 2.1, many features of the vertical cloud structure provided by CloudSat are unapparent in the TRMM cross section.

Since CloudSat provides more details on cloud vertical structure and especially the details of the cloud top, it is better suited for penetrating deep convection studies, where cloud top structure is a key determinant of deep convection entering the tropical tropopause layer (TTL). On the other hand, CloudSat is not as optimally suited to monitor deep convection within

the regional focus of this thesis, which includes the tropics and extratropics. Although CloudSat's high inclination angle allows it to monitor polar regions unobserved by TRMM, this high inclination angle also prevents the CPR from sampling the tropical atmosphere as often. Moreover, CloudSat is a nadir pointing radar, while TRMM is a cross-track scanning radar with a swath width of 247 km. These scanning differences allow TRMM to sample much larger volumes of the tropical atmosphere in comparison to CloudSat. Finally, CloudSat's sun-synchronous polar orbit, which has an equatorial crossing of 1:30 a.m./p.m., limits CloudSat from fully resolving the diurnal cycle of deep convection. This issue is more serious over land than over ocean since Soden [2000] and Liu and Zipser [2005] show that continental deep convection has a pronounced peak in frequency during late afternoon. This likely impacts the geographical distribution of penetrating and overshooting deep convection from CloudSat and is addressed in Chapter 3. Yet despite these limitations, CloudSat has been operating in space for several years and provides a statistically robust set of observations for most cloud types. A description of CloudSat Standard Products and collocated Aqua MODIS data products that are used in this thesis are provided below.

2.3 Products from CloudSat Cloud Profiling Radar (CPR)

CloudSat Standard Data Products are distributed by the CloudSat Data Processing Center located at the Cooperative Institute for Research in the Atmosphere at Colorado State University. Process Description/Interface Control Documents for the Standard Data Products may be obtained at http://www.cloudsat.cira.colostate.edu/dataICDlist.php. A brief description of the products used and evaluated in this thesis is provided below.

2.3.1 CloudSat 2B-GEOPROF Product

The 2B-GEOPROF product is the primary product used in most CloudSat studies. Version R04 is used in this thesis to provide direct observations of cloud vertical structure, evaluate cloud top height and cloud base height and validate that penetrating and overshooting deep convection are indeed being observed. The cloud geometric profile contained in the 2B-GEOPROF product includes the cloud mask, reflectivity-field, and gaseous absorption provided on a height grid with 125 vertical range bins that correspond to heights from below sea level up to ~ 25 km. The 2B-GEOPROF product is developed from range-resolved profiles of backscattered power obtained from the CPR. These measurements represent a 0.16 second average (i.e., 540 pulses) of returned power that corresponds to a horizontal resolution of 2.5 km along track by 1.4 km across track while the instantaneous field of view of the CPR is 1.8 km x 1.4 km. The vertical range resolution of the CPR is 500 m but it is oversampled to generate a range gate spacing of 250 m. This enables the effective vertical range resolution from CloudSat to be equivalent to that of TRMM and indicates that any cloud top height provided from CloudSat has an error of ± 250 m.

To identify the presence or absence of clouds, the significant echo mask or cloud mask contains values between 0 and 40 where increasing cloud mask values indicate a reduced probability of false cloud detection. Values between 30 and 40 that are used in this thesis ensure that the vertical cloud structure and cloud top heights are associated with the highest confidence levels of cloud detection.

2.3.2 CloudSat 2B-CLDCLASS Product

In conjunction with the 2B-GEOPROF product, the 2B-CLDCLASS product is used in this thesis to identify the presence and vertical extent of deep convective clouds and other types

of high clouds. According to Sassen and Wang [2007] the 2B-CLDCLASS product is developed by converting vertical profiles of radar reflectivity into cloud type. To determine cloud type, algorithms are commonly used to classify clouds based on cloud spectral, textural, and physical features. Although cloud classification schemes are limited by instrument sensitivity and subject to misinterpretation, observational features help to organize clouds into categories with unique characteristics of composition, radiative forcing, and heating/cooling effects [Hartmann et al., 1992; Chen et al., 2000]. The International Satellite Cloud Climatology Project (ISCCP) approach to cloud classification [Rossow and Schiffer, 1999] uses the combination of cloud top pressure and cloud optical depth to classify clouds into either cumulus (Cu), stratocumulus (Sc), stratus (St), altocumulus (Ac), altostratus (As), nimbostratus (Ns), cirrus (Ci), cirrostratus (Cs), or deep convective (Cb) clouds.

In contrast to the ISCCP cloud classification, the 2B-CLDCLASS product classifies clouds by using vertical and horizontal cloud properties, the presence or absence of precipitation, cloud temperature, and upward radiance from MODIS measurements to identify eight basic cloud types. These cloud types include cloud types provided from the ISCCP classification scheme, provided in Figure 2.2 with the exception that cirrus, cirrocumulus, and cirrostratus represent the class of high clouds. The characteristic cloud features for these eight major cloud types have been derived from numerous studies and are featured in Table 2.2. According to Table 2.2, deep convective clouds are categorized as clouds with cloud base heights between 0─3 km, intense shower of rain or hail possible (as suggested by its reflectivity values), a horizontal dimension of 10 km, a thick vertical dimension, and liquid water path (LWP) > 0.

Although the 2B-CLDCLASS cloud type identification algorithm is based on many of the characteristics provided in Table 2.2, it more specifically uses role-based classification methods

that assign different threshold values to characteristic parameters provided according to Table 2.3. In this approach, results of the radar cloud mask are first used to find cloud clusters that are present in both horizontal and vertical directions. Once a cloud cluster is found, cloud height, temperature, maximum dBZ, and occurrence of precipitation are determined. According to Kahn et al. [2008], cloud types As, Ns, Cb, and Cu (congestus) are well detected and classified with the radar-only algorithm. However, the class of Ci clouds is well-classified but under-detected because of the existence of small ice particles that the CPR is unable to detect. While observations of cirrus clouds become more important to this thesis in Chapter 4, CloudSat observations of high clouds, which include cirrus, cirrostratus, and cirrocumulus provide suitable samples to compare with deep convection (e.g., Sassen et al., 2008).

Although deep convective (Cb) clouds addressed in this thesis are well detected from the 2B-CLDCLASS product, adequate characterization of penetrating and overshooting deep convection from space-borne active and passive remote sensing platforms requires that the view of the cloud top and corresponding microphysical and optical properties of deep convective clouds are not contaminated by other cloud types. Thus it is important to account for very thin cirrus, which may develop over deep convective clouds as a consequence of gravity wave breaking and other dynamical processes ─ a detail that may have been missed in other studies using CloudSat observations of penetrating and overshooting deep convection (e.g., Chung et al., 2008; Luo et al., 2008).

2.3.3 CloudSat 2B-Lidar-GEOPROF product

CloudSat will often miss tenuous cloud condensate at the tops of some clouds or clouds composed only of very small ice crystals or liquid water droplets. To accurately represent the condensate at the tops of deep convective clouds and thereby identify the height to which ice

crystals may be detrained into the tropical tropopause layer and lower stratosphere, observations from Calipso, which trails CloudSat by ~15 seconds, are integrated into this analysis via the CloudSat 2B-Lidar-GEOPROF product.

To develop this product radar and lidar data streams are optimally merged to produce the most accurate description of hydrometeor layers within the atmospheric column observed by the CPR. The approximate vertical and horizontal resolutions of the lidar are compared to the CPR in Table 2.4. As indicated by Table 2.4, the lidar has higher vertical and horizontal resolutions and advances this thesis work by providing highly accurate estimations of cloud top height within $\pm$ 30 m.

Combined radar and lidar cloud masks are used to best estimate hydrometeor layers in the vertical column along the spatial dimension defined by the CPR. The output of this layer product includes the base and top heights of up to five distinct hydrometeor layers as well as some indication as to whether those layers were observed by the radar, the lidar, or both the radar and lidar. For this thesis work, this provision allows observations of penetrating and overshooting deep convective clouds to be limited to atmospheric columns with only one cloud layer thereby reducing possible contamination of very thin cirrus which may give a false estimation of cloud top height (as mentioned in Section 2.2.2). Here vertically connected CloudSat bins with cloud mask values ($\geq$ 30) define a cloud layer. A layer boundary is defined as the first encounter of a cloudy range level (of either the radar or lidar) following the occurrence of a cloud-free range level by the radar or a cloud range level with a lidar hydrometeor fraction < 0.5. More details of this description are provided in Appendix A.

For each cloud layer identified by the 2B-Lidar-GEOPROF product, the following conventions are defined:

- Due to its finer vertical resolution, the lidar is always deferred to in reporting a layer boundary. This point should be considered when interpreting differences between radar and radar-lidar cloud top heights reported for observations of penetrating deep convection provided in Chapter 3.
- If a layer top is identified by the lidar and the layer is not optically thin (i.e., $\tau <\sim 3$), the lidar will attenuate before a distinct layer base is identified. Under these circumstances, the layer base is defined by the radar observations.
- For clouds with heavy precipitation, attenuation of the radar may give a cloud-base that is too high. However for most conditions, the "cloud-base" is too low. This happens because radar attenuation through the cloud layer is not very strong and the radar continues to detect precipitation below the cloud; such that the reported "cloud base" is actually the "precipitation base". On the other hand, when the attenuation is large, there tends to be a lot of multiple-scattering which yields "false" return power below the cloud layer. Strong attenuation can be assessed based on the presence or absence of surface echoes within the radar reflectivity profile as in Battaglia and Simmer [2008]. This will be addressed in Chapter 3.

For the estimation of cloud top height, no apparent limitations have been provided for the 2B-Lidar-GEOPROF product. Limitations that have been reported relate to the Calipso vertical cloud-aerosol feature mask, which is used as an input for the 2B-Lidar GEOPROF product. This limitation suggests that the cloud-aerosol mask correctly identifies a layer as cloud or aerosol about 90% of the time. The most common misclassification occurs when portions of dense aerosol layers within the lower troposphere are labeled as cloud. However, this does not appear to be problematic for the application of the 2B-Lidar GEOPROF product in the detection of

penetrating and overshooting deep convection unless observations are reported for atmospheric regions impacted by volcanic eruptions that produce dense aerosol layers that may be confused with high level clouds.

2.4 Products from Aqua MODIS

Aqua MODIS is a passive cross-track-scanning imaging radiometer designed to take measurements in spectral regions adhering to a number of heritage sensors including those associated with the historical IR observations that will be used in Chapter 5. In addition, Aqua MODIS provides high radiometric sensitivity (12 bit) in 36 spectral bands ranging in wavelength from 0.4 μm to 14.4 μm. Bands 1 and 2 are imaged at a nominal resolution of 250 m at nadir, bands 3-7 and 26 are imaged at 500 m, and the remaining 28 emissive bands are imaged at a horizontal resolution of 1 km. A ± 55° scanning pattern at an orbit of 705 km achieves a 2,330-km swath width and provides global coverage every one to two days. This wide coverage also means that although MODIS has a high horizontal resolution at nadir, its horizontal resolution increases up to ~12 km x 6 km at the edge of the satellite swath.

Along with the other A-train satellites, Aqua MODIS has a north to south equatorial crossing of 1 p.m. While the MODIS instrument also flies on the Terra satellite, the Aqua MODIS instrument was specifically chosen for this thesis work because it trails CloudSat by ~ 60 seconds. Given this small temporal degree of separation, the Aqua MODIS instrument provides collocated passive sensor satellite radiances of penetrating deep convective clouds detected by CloudSat so that radar and IR observations of penetrating and overshooting deep convection will be captured near-simultaneously. While high horizontal and radiometric resolution makes Aqua MODIS very different from conventional satellite radiometers with lower radiometric resolutions (i.e., 8 bit), it helps us to assess sub-pixel variability not resolved by

conventional satellite radiometers, which if necessary may be evaluated at resolutions that are more consistent with the historical IR observations. Aqua MODIS products used in this thesis include the Level 1B (MOD02_1KM) radiances and the Level 2 Cloud (MYD06_L2) product respectively packaged as MODIS-AUX and MAC06S0 for specific use with CloudSat applications.

2.4.1 MODIS-AUX Product

In this thesis, the CloudSat MODIS-AUX product is used to provide IR based distributions of penetrating deep convective clouds. It is also used to evaluate the brightness temperatures corresponding to radar observations of penetrating deep convective clouds and other types of high clouds that may contaminate IR observations of penetrating and overshooting deep convection. The MODIS-AUX product contains Level 1B MODIS (MOD02_1KM_L1B) radiance and cloud mask data that overlap and surround each CloudSat (CPR) footprint. Operating one CloudSat ray at a time, the subset-to-reference algorithm uses the geolocation of the CPR footprint as a reference to find the closest MODIS pixel to the CloudSat footprint. A 3-pixel across-track by 5-pixel along-track grid that is centered on the CloudSat footprint defines the 15-element vector of MODIS L1B radiances associated with each CPR footprint. The radiance values are provided with scale factors, offsets, and radiance uncertainty indexes for Aqua MODIS bands 1-7, 17-20, and 26-36. Figure 2.3 schematically represents the intersection of the 15─element MODIS vector overlapping a CPR footprint. Additional information on the MODIS instrument calibration and characterization can be found in the MODIS L1B Algorithm Theoretical Basis Document.

2.4.2 MODIS L2 Cloud Product (MAC06S0)

The MAC06S0 product is used to identify the optical and microphysical properties of penetrating and overshooting deep convection and other types of high clouds. The MAC06S0 product is the only product used in this study that is not a part of the CloudSat standard suite of products; it can be obtained from ftp://atrain.sci.gsfc.nasa.gov/data/s4pa/MAC/. The MAC06S0 product provides 3 x 11 pixel subsets corresponding to data from the Aqua MODIS L2 Cloud product (MYD06_L2) and has a horizontal resolution of 15 km x 10 km for most variables. Data from the MAC06S0 product consists of cloud optical and microphysical properties derived from infrared, visible and near infrared radiances, which are provided for various types of high clouds in Chapter 4. Addressing the microphysical and optical properties of penetrating deep convective clouds has never been done in any other studies, and may shed further insight on the evaluation of penetrating deep convective clouds from space-borne passive sensors. Optical and microphysical properties provided by the MODIS L2 Cloud Product evaluated in this thesis includes cloud top pressure and temperature, cloud phase (where water=1, ice=2, and mixed=3), cloud fraction, optical thickness, and effective radius. These particular variables were chosen to better evaluate the factors controlling how observations of penetrating deep convective clouds are viewed from passive IR and radar observations.

The Algorithm Theoretical Basis Document provided by [King et al., 1997] can be used to find more specifics on the retrievals of each variable. However, it is of technical importance to note that cloud top pressure and temperature are specifically generated using the CO_2 slicing algorithm that corrects for possible cloud semi-transparency. The CO_2 slicing method takes advantage of differing partial CO_2 absorption in several of the MODIS infrared channels (33-36) located within the 15-micron CO_2 band. The CO_2 slicing method is addressed in Chapter 4 when

cloud top temperatures and cloud brightness temperatures are compared. Such comparison provides a better understanding of how different classes of high-level clouds are represented from these two perspectives in order to better gauge the extent to which penetrating deep convective clouds are sampled from traditional IR techniques. The CO_2 slicing method has been used in operational processing of GOES (Geostationary Operational Environmental Satellite) and HIRS (High resolution Infrared Radiometer Sounder) data, and has been found to have accuracies of approximately 50 mb for clouds above ~700 mb.

2.5 Summary and Discussion

The TRMM precipitation radar has been used in several investigations of penetrating and overshooting deep convection [Alcala and Dessler, 2002; Liu and Zipser., 2005; Liu et al., 2007]. However, characteristics of the TRMM PR considerably differ from the CloudSat Cloud Profiling Radar. As previously described, CloudSat provides more details of the vertical cloud structure and especially the cloud top. Thus, CloudSat observations provide an opportunity to more definitively capture and evaluate penetrating and overshooting deep convection entering the TTL and lower stratosphere.

CloudSat, Calipso, and Aqua MODIS observations that will be used in subsequent chapters of this thesis have been described. The advantages of each of these three instruments have been documented and approaches used to obtain various types of measurements (i.e., radar reflectivity, cloud top pressure, cloud top temperature, etc.) from each instrument have been provided. As described, the combination of all three data sets provide unparalleled global sampling of optical and microphysical properties of clouds and is especially well suited for the detection of penetrating deep convective clouds. While each instrument has limitations, these limitations do not represent significant issues with regard to the objectives of this thesis.

Table 2.1: The radar characteristics of CloudSat and TRMM show differences in geographic coverage, temporal resolution, scan characteristics, radar characteristics, and list auxiliary instruments in or associated with the payload.

		TRMM PR	CloudSat CPR
Geographic Coverage	Latitudinal Coverage	38°N-38°S	90°N-90°S
	Longitudinal Coverage	180°W-180°E	180°W-180°E
	Orbit	Equatorial	Polar
	Swath Width	247 km	n/a
Temporal Resolution	Repeat Cycle	16 days	16 days
	Orbits per day	16	16
Scan Characteristics	Scanning Geometry	Cross Track ±17°	Nadir Pointing
	Swath Width	247 km	0
	Vertical Res.	250 m	500 m
	No. Vertical Range Gates	80 (0-20 km)	125 (0-25 km)
	Horizontal Res.	5 km	1.8 km x 1.4 km
Radar Characteristics	Radar Sensitivity	12 dBZ	-28 dBZ
	Operating Frequency/Band	13.8 GHz/Ku	94 GHz/W
	Mean Diameter Size	~275 μm	~30 μm
	Satellite Altitude	350 km	705 km
	Pulse Width	1.07 μs	3.3 μs
	Antenna Power	≥ 500 W	700 W
Instruments in/associated with Payload		TRMM Microwave Imager (TMI)	Calipso
		Visible Infrared Scanner (VIRS)	Aqua MODIS
		Clouds and the Earth's Radiant Energy System (CERES)	Aura Microwave Limb Sounder (MLS)
			Atmospheric Infrared Sounder (AIRS)
		Lightning Imaging Sensor (LIS)	Atmospheric Microwave Sounder Unit (AMSU-A)

Table 2.2: (cf., Wang and Sassen, 2007) Characteristic cloud features for the major cloud types derived from numerous (midlatitude) studies.

Cloud Class	Cloud Features	
High Cloud /Cirriform (1)	Base	>7.0 km
	Rain	no
	Horizontal Dimension	10^3 km
	Vertical Dimension	moderate
	LWP	=0
As (2)	Base	2.0-7.0 km
	Rain	none
	Horizontal Dimension	10^3 km, homogeneous
	Vertical Dimension	moderate
	LWP	~0, dominated by ice
Ac (3)	Base	2.0-7.0 km
	Rain	virga possible
	Horizontal Dimension	10^3 km, homogeneous
	Vertical Dimension	shallow or moderate
	LWP	>0
St (4)	Base	0-2.0 km
	Rain	none or slight
	Horizontal Dimension	10^3 km, homogeneous
	Vertical Dimension	shallow
	LWP	>0
Sc (5)	Base	0-2.0 km
	Rain	drizzle or snow possible
	Horizontal Dimension	10^3 km, inhomogeneous
	Vertical Dimension	shallow
	LWP	> 0
Cu (6)	Base	0-3.0 km
	Rain	drizzle or snow possible
	Horizontal Dimension	1 km, isolated
	Vertical Dimension	shallow or moderate
	LWP	> 0
Ns (7)	Base	0-4.0 km
	Rain	prolonged rain or snow
	Horizontal Dimension	10^3 km
	Vertical Dimension	thick
	LWP	> 0
Deep Convective clouds (8)	Base	0-3.0 km
	Rain	intense shower of rain or hail possible
	Horizontal Dimension	10 km
	Vertical Dimension	thick
	LWP	> 0

Table 2.3: (cf., Wang et al., 2007) Cloud ID rules based approximately on the properties for the 98th percentile of data for each cloud type that was sampled during first 6 months while CloudSat was in orbit.

Type	Z_{max}	Precipitatin	Length (km)	Highest Z_{max} frequency	Other
Cirrus	<-3 dBZ, T < -22.5°C	No	2→>1000	-25 dBZ @ -40°C	
Altostratus	<10dBZ, -20°<T<-5°C; =-30 dBZ @ -45°C	No	50→ > 1000	-10 dBZ @ -25°C	
Altocumulus	<0 dBZ, -20°<T<-5°C; =-30dBZ @ -35°C	Yes/No	2→ > 1000	-25 dBZ @ -10°C	T_{top} > -35°C
St	<-5dBZ, -15°<T<25°C	Yes/No	50→ > 1000	-25 dBZ @ -10°C (Bright Band)	Altitude of Z_{max} < 2 km AGL;
Sc	<-5 dBZ, -15°<T<25°C	Yes/No	2→ > 1000	-25 dBZ @ -10°C (Bright Band)	Altitude of Zmax < 2 km AGL; spatially inhomogeneous
Cumulus	< 0 dBZ, -5°<T<25°C	Yes/No	2-25	-25 dBZ @ -15°C (Bright Band)	ΔZ > 2 km
Deep (cb)	< -5 dBZ, -20°<T<25°C	Yes	10-50	10 dBZ @ 5°C	ΔZ > 6 km
Ns	-10 < Z < 15, -25°<T<10°C	Yes	>100	+5 dBZ @ 0°C	ΔZ > 4 km

Table 2.4: Approximate vertical and horizontal resolutions of the CloudSat CPR and the Calipso Lidar.

	Cross Track	Along Track	Vertical
CPR	1.4 km	2.5 km	0.25 km
Lidar	0.3 km	1 km- < 8.2 km 0.3 km > 8.2 km	0.03 km < 8.2 km 0.075 km > 8.2 km

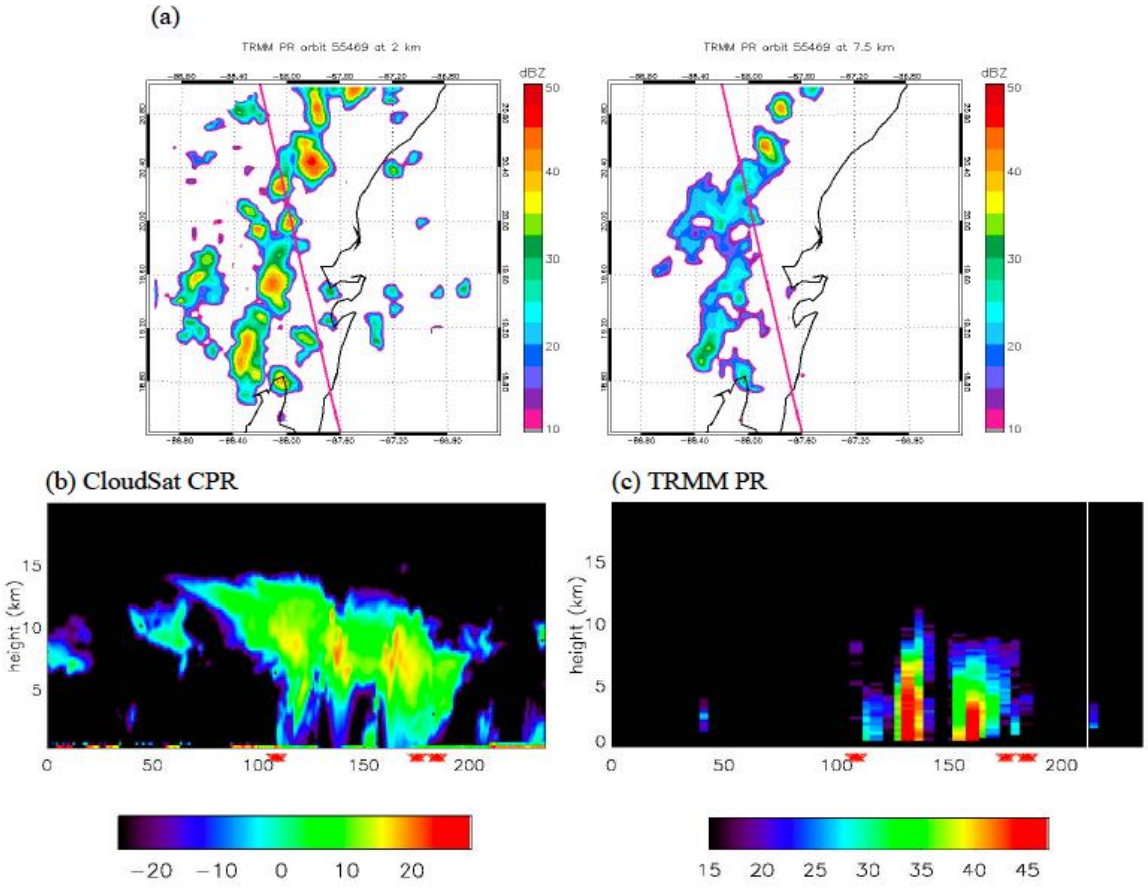

Figure 2.1: (cf., Li and Schumaker, 2010) Images of a coincident CloudSat and TRMM overpass showing a) TRMM PR horizontal cross sections at 2 and 7.5 km for orbit 55469 with CloudSat track in magenta, and vertical cross sections of b) CloudSat CPR and (c) TRMM Precipitation Radar. The scan time of the images is around 19:23 local time on 10 August 2007. CloudSat is about 5 minutes in front of TRMM with the track centered at 19.85°N, 87.93°W. The color bars are reflectivity in dBZ.

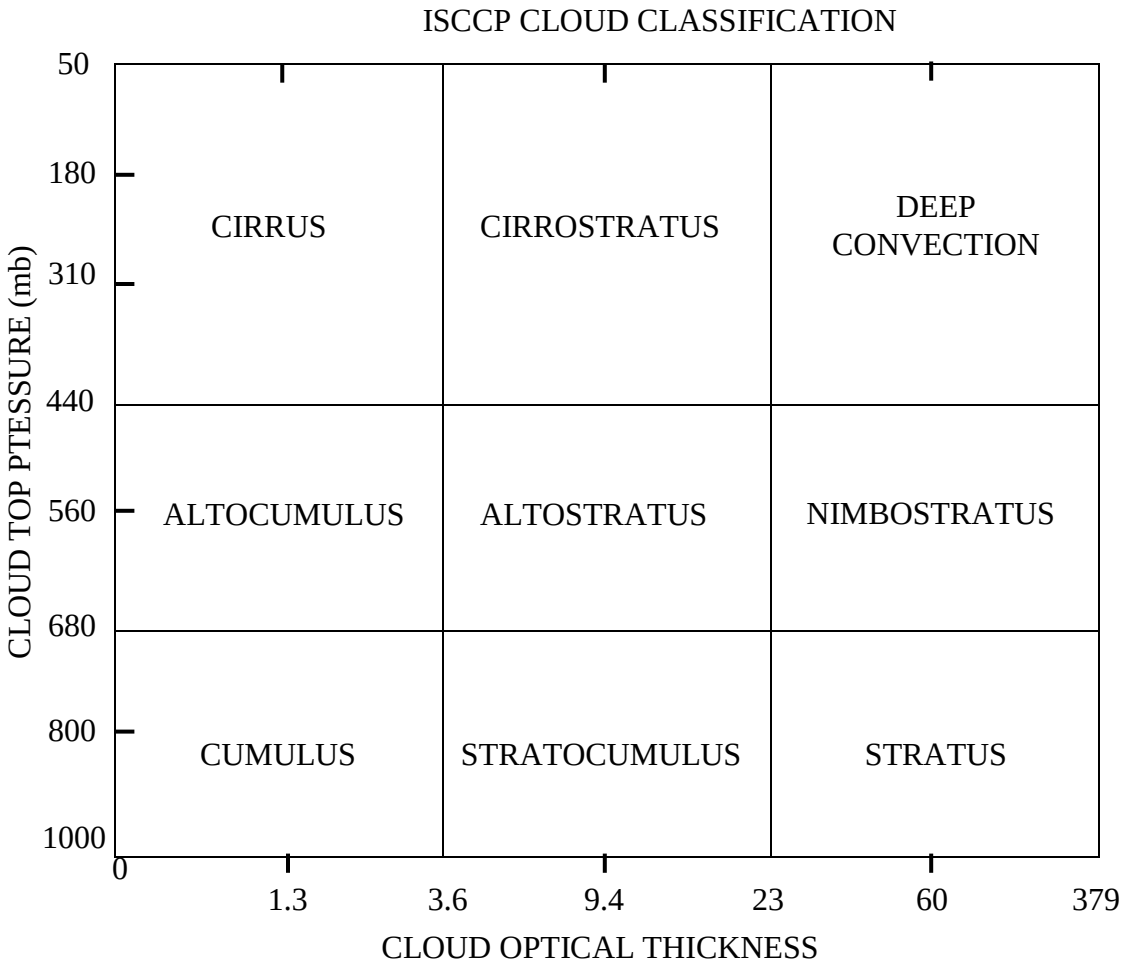

Figure 2.2: Cloud classification in the ISCCP D-series dataset.

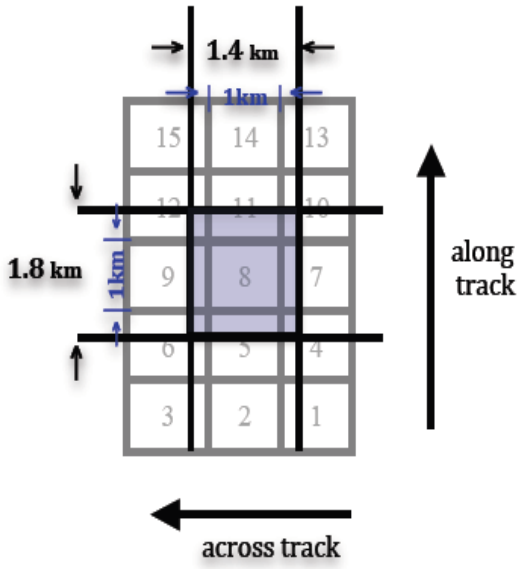

Figure 2.3: Schematic representation of MODIS-AUX 3 km x 5 km subset associated with 15 pixels that surround and overlap the CPR footprint, which is highlighted in light blue.

CHAPTER 3

CHARACTERIZATION OF PENETRATING DEEP CONVECTION

3.1 Penetrating Deep Convection from Previous CloudSat and TRMM Studies

Deep convection that penetrates the tropical tropopause layer (TTL) plays an important role in affecting the heat budget [Sherwood et al., 2003; Kuang and Bretherton, 2004] and moisture distributions [Danielsen, 1982; Sherwood and Dessler, 2000] of the tropical upper troposphere and lower stratosphere.

Although deep convection reaching the TTL has most commonly been monitored from passive sensor sounders and imagers, these observations do not provide direct measurements of cloud vertical structure. Instead, cloud vertical structure is derived using combinations of radiative transfer modeling and a priori assumptions about the surface and atmospheric state. The advent of space-borne radar has added a complementary view of penetrating deep convection from passive sensor observations that may be used to better evaluate cloud vertical structure and cloud top properties inferred from IR data.

Simpson et al. [1998] was the first to observe deep convection extending into the TTL using the first space-borne radar, the TRMM Precipitation Radar (PR), during Typhoon Paka in early December 1997. This led to the application of the TRMM PR in studies seeking to evaluate the characteristics of deep convection reaching the TTL. One of such studies includes Alcala and Dessler [2002] who defined deep convection reaching the TTL by reflectivity tops with heights > 14 km and a minimum depth of 1.5 km where all reflectivities exceed 12 dBZ. From this definition, the frequency and seasonality of deep convection reaching the TTL was evaluated over the entire tropics for 4 months (January 1998 and 1999, and July 1998 and 1999). These observations were then compared with IR brightness temperatures ≤ 207.5 K from the TRMM

Visible Infrared Sounder (VIRS). The radar and IR observations showed the same inter-seasonal and inter-annual patterns, including the behavior of the ITCZ and the South Pacific Convergence Zone (SPCZ). While Alcala and Dessler [2002] also show qualitative differences between radar and IR observations that are primarily due to the sensitivities of each instrument, no quantitative comparison between IR and radar observations were made. Although the authors only provide results for four months, they also show considerable differences in the frequency of penetrating deep convection when evaluated from tropical deep convective clouds verses tropical deep convective rain, reported as 5% and 1.5% respectively.

Liu et al. [2007] used observations from the TRMM PR and VIRS between 35°N – 35°S and over the periods 1998-2001 and 2003-2004. In their study the relative frequency distribution of 20 dBZ radar echo heights at 6 km, 10 km, and 14 km were compared with the frequency distribution of cold cloud features, defined by a minimum of 4 VIRS pixels with cloud top brightness temperatures colder than 235 K and 210 K. Liu et al. [2007] show that the distribution of cold cloud features ≤ 210 K was most highly correlated with 20 dBZ radar echo tops at 6 km and they report that only 1% of cold cloud features ≤ 210 K had 20 dBZ echo top heights > 14 km. Liu et al. [2007] also show that 20 dBZ echoes reaching 14 km are concentrated over the tropical land regions of central Africa and equatorial South America, rather than over the tropical west Pacific and Indian Oceans where IR studies typically show that deep convective clouds reaching the base of the TTL are most frequent. While insight from this study provides statistical evidence between radar and IR observations of penetrating deep convective clouds, the 20 dBZ echo top criteria used by Liu et al. [2007] is more rigid than the criteria used by Alcala and Dessler [2002]. As already discussed in Chapter 2, the TRMM PR is sensitive to larger sized particles. Given these details and the criteria that penetrating tops must have 20 dBZ echo tops >

14 km, it is likely the analysis provided by Liu et al. [2007] does not consider all deep convection reaching the TTL.

To evaluate the potential insights of penetrating deep convection from CloudSat, Luo et al. [2008] combined several CloudSat standard data products (ECMWF-AUX, MODIS-AUX, 2B-GEOPROFL, 2B-Lidar-GEOPROF, and 2B-CLDCLASS) to develop a temperature-height classification scheme for tropical (15°N-15°S) penetrating deep convective clouds observed during 2007. The height classification scheme revealed three classes of penetrating deep convection; warm-high, cold-high, and cold-low. The warm-high class is defined by penetrating deep convective clouds with cloud tops that are warmer and higher than the cold point tropopause (CPT). The cold-high class is defined by penetrating deep convective clouds that are colder and higher than the CPT and the cold-low class is defined by penetrating deep convective clouds with cloud tops that are colder but lower than the CPT.

Given these three classes, Luo et al. [2008] suggest that deep convective clouds with cloud brightness temperatures colder than the CPT do not always determine the occurrence of penetrating and overshooting deep convective clouds. The authors also reveal that the warm-high class dominates as ~ 47% of all tropical deep convection reaching 14 km. They interpret the warm-high class to be due to a geometrically thick depth of small ice crystals contained in the upper portions of the deep convective cloud. In this scenario, the IR emission temperature of the warm-high class comes from deeper within the cloud. This allows the IR brightness temperature to be warmer than the CPT while the hydrometeor cloud top height, which corresponds to the height level of the small ice crystals, is higher than the CPT. While Luo et al. [2008] also relate each cloud class to life cycle stages of a deep convective cloud, their study does not evaluate any other properties of penetrating deep convective to better determine how well observations of

penetrating deep convection from CloudSat are spatially resolved from conventional passive sensor satellites.

Although observations of penetrating deep convection used for the temperature-height classification scheme of Luo et al. [2008] were also used to develop a satellite-based method to estimate convective buoyancy (B) and entrainment rate [Luo et al., 2010], these observations are based on snapshots of thunderstorms and their environments. Results of the cloud top temperature-height classification scheme are consistent with Setvák et al. [2003], Levizzani and Setvák [1995], Adler and Mack [1986], Heymsfield and Blackmer [1988], and Heymsfield et al. [1991] who examined storm cloud top structure.

In these earlier studies that only used IR data, cold-warm brightness temperature couplets occurred in cold U-shape and V-shape thunderstorm cloud top features suggesting that deep overshooting convection is often marked by relative maximums in brightness temperature. However, these studies are related to midlatitude systems, and Luo et al. [2008] investigate penetrating deep convective clouds within the tropics (15°N-15°S) where such structure has not been reported. While it is clear that most cross tropopause transport occurs across the TTL, Mulendore et al. [2003; 2005] show that midlatitude systems can reach the lowermost stratosphere via upward diabatic transport from the midlatitude troposphere. Although convection in midlatitudes may account for only a small percentage of the mass of tropospheric air mixed into the lowermost stratosphere, this pathway should not go unchecked.

In this chapter of the thesis, observations of penetrating and overshooting deep convection from CloudSat/Calipso and Aqua MODIS are obtained to address the following:

1. *What additional insight on the characteristics of penetrating and overshooting*

deep convection does CloudSat provide with regard to cross tropopause transport via tropical and extratropical deep convection?

2. *What is the interpretation of CloudSat observations of penetrating deep convection when viewed from passive sensor satellite radiometers according to traditional IR techniques?*
3. *What is the areal size distribution of penetrating deep convection observed from CloudSat and what does it tell us about the capabilities of conventional passive sensor satellite radiometers to distinctly resolve these events?*

3.2 Application of CloudSat, Calipso, and Aqua MODIS Data Products

CloudSat/Calipso and Aqua MODIAS data products described in Chapter 2 are used for the year 2007 and the region between 35°N and 35°S. The CloudSat 2B-CLDCLASS product is used to determine the locations of deep convection. According to the 2B-CLDCLASS product, deep convective clouds have cloud base heights between 0-3 km, a horizontal dimension of 10 km, a thick vertical dimension, liquid water path (LWP) > 0 and as suggested by their reflectivity values (i.e. 10 dBZe at 5° C), an intense shower of rain or hail is possible. For each profile of deep convection that is detected, the 2B-GEOPROF radar product is used to capture hydrometeor cloud top height and cloud base height. The vertical range gates where cloud top height and cloud base heights are detected must have cloud masks values ≥ 30, indicating that relatively strong radar echoes are present. The cloud's vertical boundaries are further characterized using the 2B-Lidar-GEOPROF product which integrates CloudSat with the characteristics of the Calipso Cloud-Aerosol Lidar with Orthogonal Polarization (CALIOP). The 2B-Lidar-GEOPROF product provides the most accurate estimate of hydrometeor layer base and top for up to five layers in each vertical CPR profile, allowing observations of deep convection to be limited to

atmospheric columns with only one cloud layer. Penetrating and overshooting deep convective clouds are obtained from deep convective clouds with radar cloud top heights ≥ 13 km and lidar cloud top heights ≥ 14 km.

To assess IR-based methods traditionally used to detect penetrating and overshooting deep convection, the infrared window (IRW) brightness temperature, which serves as the cloud brightness temperature, will be examined. To determine if +BTD signatures (introduced in Chapter 1) occur for penetrating deep convective clouds, the BTD signature is examined according to the relation:

$$BTD = BT_{6.7} - BT_{11} \qquad \textbf{3.1}$$

where $BT_{6.7}$ represents brightness temperatures at the 6.7 μm infrared water vapor absorption band and BT_{11} represents brightness temperatures in the infrared window (IRW) at 11 μm. Brightness temperatures in the IRW and IR water vapor absorption band are derived using the CloudSat MODIS-AUX product, which provides a 3 km x 5 km (across track x along track) subset of Aqua MODIS-L1B data along the narrow dimension of the CloudSat orbit (see Figure 2.3 described in Chapter 2). In accordance with Fujita [1992] and Brunner et al. [2007] who note that the geometrical size of an overshooting top is usually less than 10 km in diameter, the entire 3 km x 5 km subset provided by the CloudSat MODIS-AUX product is not used. Instead, brightness temperatures are based on the mean 3 km x 3 km subset of the MODIS-AUX data that overlaps and surrounds the CPR footprint. Although Aqua MODIS data is given at multiple wavelengths, IRW and BTD signatures are calculated using Aqua-MODIS radiances from band 31 at ~11 μm and band 27 at 6.7 μm. In this calculation, radiances are scaled and converted to brightness temperatures using the inverse of the Planck function. All observations are recorded with date, time, and geolocation information.

In our final stage of evaluation, observations from the CPR are expanded from their conventional use in providing cross sectional profiles, to a more focused view of each CPR footprint. This application of the CPR is adapted here since penetrating deep convective clouds, which include overshooting tops, are often as small as 1 km^2. Thus, the CPR is not just measuring a vertical cross-section but rather, the complete or near-complete volume of the penetrating top. Since the CPR has an instantaneous footprint of 1.8 km x 1.4 km (along track x across track) each observation from the CPR corresponds to a geometrical area of 2.52 km^2. By grouping consecutive CPR profiles of penetrating deep convective clouds and using the CPR along track dimension of 1.8 km, two approaches are used to estimate the size distribution of penetrating and overshooting tops. In the first approach, the area of the instantaneous CPR footprint is used to estimate the areal size distribution of penetrating tops. In the second approach, we assume that the penetrating top has the geometrical structure of a uniform plume where the length of its x and y cross-sections is equivalent to the length given by the number of consecutive footprints.

3.3 Results from CloudSat Observations of Penetrating Deep Convection

CloudSat observations are used to validate that penetrating and overshooting deep convection are observed, provide evidence of their vertical extent and characterize their geospatial and seasonal properties, areal size distribution, hydrometeor cloud top height, IRW brightness temperature, and BTD signature.

3.3.1 Evidence of Vertical Extent

In this analysis, 736,443 CPR profiles were identified as deep convective clouds with radar-lidar cloud top heights ≥ 14 km**.** To provide evidence of their vertical extent, a concatenated image of 10,000 of the 736,443 CPR profiles is provided in Figure 3.1. Close

inspection of Figure 3.1 shows that many of these profiles reach higher than 15 km. Another obvious feature of this image is a broken pattern of strong echo returns near the surface that is due to rather strong attenuation of the radar beam. According to Battaglia and Simmer [2008], strong attenuation can be assessed by examining each radar reflectivity profile. Some of these profiles are provided in Figure 3.2 where surface echoes have been divided into four categories to highlight differences between profiles with strong surface echoes (20 to 30 dBZe), moderate surface echoes (10 to 20 dBZe), weak echoes (6 to 10 dBZe), and very weak echoes (< 6 dBZe). Among all profiles, strong surface echoes are present in 47%. Surface echoes ranging from strong to weak are present in 78.03% and 21.96% have very weak surface echoes (to no surface echo at all). The presence of a surface echo suggests that the radar beam is not completely attenuated. Despite multiple scattering, radar profiles with surface echoes can be used to sufficiently estimate the cloud base height to more fully evaluate the vertical extent of each penetrating deep convective cloud.

For observations provided in Figure 3.1, Table 3.1 provides multi-satellite statistics corresponding to cloud base height, cloud top height, cloud brightness temperature, BTD signature, maximum radar reflectivity ($\overline{dBZe}_{max}$), and number of cloud layers for CloudSat observations of deep convection reaching and penetrating 14 km and 16.9 km over 20°N - 20°S and 35°N - 35°S. As indicated by the number of cloud layers, observations included in this analysis are uncontaminated by multilayer clouds. This includes thin cirrus distinguishable by the Calipso lidar. Differences between mean cloud top height and cloud base height show strong vertical development suggestive of deep convective cores. As indicated by Weisz et al. [2007], the mean radar-lidar cloud top height is greater than the radar height. This is expected due to the differences in measuring capabilities between Calipso and CloudSat (see Chapter 2). For

observations at 14 and 16.9 km, the total number of observations between 35°N - 35°S are ~ 12.6% more than the total number between 20°N - 20°S. While these observations show that cross tropopause transport occurs not only in the tropics but also the extratropics, the characteristics of penetrating deep convection in extratropical regions differ negligibly from most of the statistics between 20°N - 20°S.

Between 20°N - 20°S and 35°N - 35°S, the mean cloud brightness temperature of deep convective clouds reaching 14 km and 16.9 km is 213.5 K and 197.4 K respectively. The mean maximum reflectivity, $\overline{dBZe}_{max}$, from ~ 2 km to ~ 20 km is ~13.25 dBZe. The BTD signature of deep convective clouds at 14 km is slightly negative at -0.5 while deep convective clouds reaching 16.9 km show more positive values. When compared with penetrating deep convective clouds ≥ 14 km, deep convective clouds with cloud tops ≥ 16.9 km have +BTD values due to their close proximity to the cold point tropopause. According to Schmetz et al. [1997], +BTD signatures are likely characteristics of deep convective clouds with rather high cloud top heights and is supported by this result. However, Schmetz et al. also show that positive BTD depends on the amount of water vapor above the tropopause region and on the temperature lapse rate in the stratosphere. For deep convective clouds with very strong updrafts, large BTD values may also be due to the injection of water vapor into the lower stratosphere.

3.3.2 Geographical and Seasonal Distribution

The geographical frequency distributions of penetrating deep convection at 14 and 16.9 km are provided in Figures 3.3a and 3.3b. As expected, dominant regions in the distribution are associated with the large-scale dynamical structure of the tropical atmosphere [Webster and Chang, 1988]. The highest densities are found over the Indian and west tropical Pacific Oceans, South and central America and Africa. Although only ~ 4% of all penetrating deep convection

between 20°N-20°S and 35°N-35°S reaches 16.9 km, the largest contributions to the 16.9 km distribution occur over the tropical west Pacific Ocean and Indian and Australian Monsoon regions.

Figure 3.3a differs from Liu et al. [2005, 2007], who used the Tropical Rainfall Monitoring Mission (TRMM) precipitation radar to evaluate 20-dBZe echo-top heights reaching 14 km and showed that the largest fractions of deep convection reaching 14 km occur over continental regions including Africa and South America. Differences between CloudSat and TRMM are likely due to the 1:30 a.m./p.m. equatorial crossing of CloudSat, which prevents the CPR from sampling the complete diurnal cycle of deep convection. Incomplete sampling of the diurnal cycle and differences in the detection capabilities of TRMM and CloudSat likely produce discrepancies between the two datasets. Although the extent to which a full sampling of the diurnal cycle would modify the results of Figures 3.3a and 3.3b is unclear, the geographical distribution of penetrating deep convection from CloudSat is consistent with IR studies (e.g. Gettelman et al., 2002; Rossow and Pearl, 2007) that are based on synoptic observations that do fully sample the diurnal cycle.

The seasonal distribution of penetrating deep convection from CloudSat is shown for December-February (DJF) in Figure 3.4a and for June-August (JJA) in Figure 3.4b. The distribution of penetrating deep convection follows the migration of the ITCZ by shifting south of the equator near 10°S in January to north of the equator near 15°N in July. By characterizing the vertical extent and geospatial and seasonal distributions of penetrating deep convection these observations provide evidence on the nature of the systems contained in this analysis.

3.3.3 Passive Sensor Cloud Top Brightness Temperature and BTD Signature

Since penetrating deep convection distinguished from passive sensor satellite radiometers are based on +BTD signatures and cloud brightness temperatures these observations are provided with respect to cloud top height in Figures 3.5a and 3.5b. As already described, the mean cloud brightness temperature of all penetrating deep convective clouds is ~ 213.5 K. However, relatively warm cloud brightness temperatures that lead to highly negative BTD signatures are also observed. As shown in Figures 3.5a-3.5b penetrating deep convective clouds with relatively warm cloud tops produce a range of cloud top brightness temperatures compared with height. This wide range makes the evaluation of cloud top height with cloud top temperature and BTD signature obscure. To minimize such obscurities, temperature thresholds are applied in Figures 3.5c─3.5f to delineate clouds that may be colder than the base of the TTL. By applying brightness temperature thresholds of 210 K (Figures 3.5c and 3.5d) and 200 K (Figures 3.5e and 3.5f) the observations become more consistent with the traditional view that colder clouds reside at higher levels. After the 210 K brightness temperature threshold is applied the mean cloud top temperature within the distribution becomes colder with a value of ~ 203 K and BTD signatures become more positive with a value of 1.1 K. As described in Section 3.3.1 the coupling of positive BTD signatures and relatively low cloud top brightness temperature thresholds appears to be a reasonable approach for the detection of penetrating deep convection. Table 3.2 shows the percent occurrence of penetrating deep convective clouds detected using IRW brightness temperature thresholds of 235 K, 210 K and 200 K and +BTD signatures. According to Table 3.2, within the tropics (20ºN - 20ºS) 56.6% of all deep convective clouds reaching 14 km have IRW brightness temperatures between 235 K and 210 K, ~39.89%(10.35%) have IRW brightness temperatures ≤ 210 K(200 K) and ~59.42% exhibit the +BTD signature.

While Chung et al. [2008] show that 96% of all cases of deep convective clouds with cloud top heights > 14 km and cloud depths > 6 km exhibit the +BTD signature, it is not clear if warm high clouds were detected in their examination or how these clouds were treated. However, more positive BTD signatures are obtained for specific observations of penetrating deep convection when brightness temperature constraints are also applied.

3.3.4 Areal Size Distribution

As described in Section 3.2, two approaches are used to estimate the size distribution of penetrating and overshooting tops. In the first approach the areal extent is calculated from the area associated with the number of consecutive CPR footprints. In the second approach, the penetrating top is assumed to be a uniform plume where the length of its x and y cross-sections are both equivalent to the length given by the number of consecutive footprints.

The areal size distributions corresponding to these two approaches are provided in Table 3.3. Results provided in Table 3.3 show rather large differences in areal size distributions calculated using the CPR footprint verses the uniform plume assumption. However, since penetrating tops are spot-like features according to visible and IR imagery (e.g., Bedka and Minnis, 2010), the uniform plume assumption is reasonable. According to this criteria, deep convective clouds detected within 2-4 CPR footprints, where 4 footprints is the maximum, have an area of 51.84 km^2. Penetrating deep convection observed over more than four consecutive CPR footprints (i.e., 5-7, 8-10, etc.) are calculated similarly. The combination of the information provided in Table 3.3 with the relative areal size distribution of penetrating tops provided in Figure 3.6 shows that 35% of all penetrating deep convection are observed over one CPR footprint while 15.34% are detected within 2-4 CPR footprints. These statistics are provided in Table 3.3 and gives some indicate that 65-49% of penetrating deep convection are resolvable

using historical IR observations with resolutions of 10 km x 10 km. Estimations of the areal size distribution of penetrating tops provide a key element needed to evaluate the capabilities of conventional passive sensor satellite radiometers to resolve penetrating deep convective clouds. However, due to random sampling, it is unlikely that the CPR provides reflectivity profiles corresponding to the center of each deep convective cloud. It is more likely that the observations are taken at varying ranges of the outer chord. According to Table 3.4 the estimation of the plume's areal size for lengths corresponding to an outer chord, provides areal sizes even smaller than the true dimension of the uniform plume. Thus estimations of the areal size distribution provided here give a lower limit of the areal size of each penetrating top, which further supports the view that a considerable fraction of penetrating deep convective cloud tops should be detectable from the historical IR observations.

This information provides a better understanding on the capability of historical IR observations to detect penetrating deep convection so that the data may be used to develop a cloud climatology of penetrating and overshooting deep convection events that may have strong impact on variability of lower stratospheric water vapor.

3.4 Summary and Discussion

Results given in this chapter show that CloudSat provides unprecedented observations on the vertical extent of penetrating deep convective clouds. To capture deep convection the 2B-CLDCLASS product has primarily been used. This product classifies deep convective clouds according to reflectivity profiles with 10 dBZe echoes present at 5°C. When combined with the restriction that radar-lidar cloud top heights must be ≥14 km, this product serves well in providing a database of penetrating deep convection that may be used for further analysis and study.

In the remaining sections of this discussion, the results of this study are evaluated to outline the general characteristics of penetrating deep convection and specifically address the questions provided in Section 3.1

What additional insight on the characteristics of penetrating and overshooting deep convection does CloudSat/Calipso provide with regard to cross tropopause transport via tropical and extratropical deep convection?

Using CloudSat/Calipso observations deep convection that penetrates the TTL but deep convection that reaches 14 km has been differentiated from deep convection that reaches even greater altitudes. From the results presented only ~ 4% of all penetrating deep convection reach 16.9 km. However, the impact these very high reaching deep convective clouds may have on the moisture and heat distributions of the upper troposphere and lower stratosphere is not quite clear. While several studies are able to reproduce lower stratospheric water vapor distributions consistent with direct convectively driven injection of air mass into the TTL followed by slower radiative ascent during which air moves quasi-horizontally and passes through the tropopause observational evidence for direct and irreversible injection into the lower stratosphere (e.g., Alcala and Dessler, 2002), is not well documented. CloudSat observations of deep convection with cloud top heights ≥ 16.9 km may be used to further evaluate this pathway. They also provide a quantitative measure regarding the frequency of these events. In addition, observations of high reaching deep convective clouds may be used to determine the most suitable locations for regional studies.

Characterization of the seasonal and geospatial properties of penetrating deep convection provided by CloudSat show that the largest contribution occurs over the western tropical Pacific and Indian Oceans. This result is consistent with the view of penetrating and overshooting deep

convection from IR studies (e.g., Alcala and Dessler, 2002) and also the recent modeling work of Hoskins et al. [2010]. However, it is unclear how this distribution would change if the diurnal cycle of deep convection sampled from CloudSat were more fully resolved. Although the high LNB over the western tropical Pacific likely comes into play when considering deep convective clouds with cloud tops ≥ 14 km, the approach used in this analysis is consistent with other several other studies evaluating deep convection that reaches the TTL (e.g., Liu et al. 2005; 2007) . Among all observations between 35°N and 35°S ~87% occur within the tropical region between 20°N-20°S. This result shows the dominance of cross tropopause transport via tropical penetrating deep convection but also provides a quantitative assessment on the contribution to cross tropopause transport from the extratropics. This statistic is however likely to decrease if the 14 km height criteria were adjusted to compensate for lower tropopause heights that are consistent with extratopical regions.

What is the interpretation of CloudSat observations of penetrating deep convection when viewed from passive sensor satellite radiometers and according to traditional IR techniques?

Results from the combined CloudSat/Calipso and Aqua MODIS analysis have been used to characterize penetrating deep convection from passive sensor observations and according to traditional IR approaches. According to the results shown here, ~40% of all penetrating deep convective clouds are associated with cold cloud features ≤ 210 K and ~60% of penetrating deep convective clouds exhibit the positive BTD signature. Both techniques sample rather significant portions of penetrating deep convection justifying their application in many IR studies. The extent to which cold cloud features ≤ 210 K and +BTD signatures represent penetrating deep convective clouds is still unclear. It is still unknown the $BT_{11} \leq 210$ K signal represents

penetrating deep convection, which may moisten the lower stratosphere, or if the signal primarily represents cirrus-anvil cloud fractions, which may have an opposing effect on the lower stratospheric water vapor budget (e.g., Jensen et al., 1996, 2004).

Liu et al. [2007] report that only 1% of cold cloud features ≤ 210 K were associated with penetrating deep convection having 20 dBZ echoes reaching 14 km. However, CloudSat and TRMM radar characteristics are different and will likely reveal different statistics since the IR emission cloud top is typically situated above TRMM PR echo tops and below CloudSat echo tops. If the capabilities of the TRMM PR only allowed Liu et al. [2007] to weakly sample penetrating deep convective cloud tops than the statistics reported by that study serve a very limited view and provide a rather incomplete picture.

Fu et al. [1990] evaluated deep convective clouds and cirrus/anvil clouds using satellite infrared radiances from ISCCP D1 data obtained for January 1984 and July 1983. While the authors report that it is not possible to select thresholds that admit all deep convective clouds while filtering out all other cloud types, their study suggests that relatively low cloud top temperatures is a useful way to isolate deep convective clouds. Their study also suggests that a larger fraction of clouds with infrared brightness temperatures ≤ 210 K are associated with deep convective clouds which are likely reaching 14 km than suggested by Luo et al. [2007]. However, unlike the latter study, Fu et al. [1990] does not provide a quantitative description on the fraction of deep convective clouds reaching 14 km. This issue will be further addressed in Chapter 4.

What is the areal size distribution of penetrating deep convection and what does it tell us about the capabilities of conventional passive sensor satellite radiometers to distinctly resolve these events?

To evaluate the capabilities of passive sensors to detect penetrating deep convection, it is not only important to assess traditional IR techniques but it is also important to evaluate how well penetrating deep convective clouds may be spatially resolved. The latter is especially important considering that most passive sensor sounders and imagers do not have spatial resolutions as high as Aqua MODIS, which provides observations in its emissive bands at a nominal resolution of 1 km.

To evaluate the capability of conventional passive sensor satellite radiometers to spatially resolve penetrating deep convection, it is assumed that the shape of penetrating and overshooting deep convective clouds are uniform plumes with equivalent dimensions along x and y axes. Using this assumption, 49% to 65% of penetrating deep convective clouds have areas of 51.84 km^2. This indicates that for the historical IR observations with horizontal resolutions of 10 km x 10 km, which will be used in Chapter 5, a considerable fraction of penetrating and overshooting deep convective clouds is resolvable. Rossow and Pearl [2007] provide the only other study to report the size distribution of deep convection entering the TTL. However they use passive sensor observations that do not directly resolve cloud vertical structure or cloud top height. They also do not directly identify the areal sizes of penetrating tops but rather the sizes of systems with pixels defined by $BT_{11} < 220$, $BT_{11} < 200$ K and $BT_{11} < CPT$. Rossow and Pearl [2007] suggests that penetrating and overshooting deep convective clouds do not occur in systems with radii < 37 km. However, smaller systems occurring over the western tropical Pacific may also be associated with differences in observations of penetrating tops in the evaluation of CloudSat observations and TRMM. In Figure 3.7, a CloudSat cross section centered over Indonesia on October 22, 2006 shows an isolated deep convective cloud with diameter of ~ 20 km and radii of ~10 km that contains an overshooting top.

Given these results, the analysis of penetrating deep convective clouds shown here provides additional evidence on the characteristics of penetrating deep convective clouds compared with other instruments and studies. Collocated CloudSat/Calipso and Aqua MODIS observations provide more context regarding the interpretation of penetrating deep convective from IR sensors. The combined radar/lidar and IR analysis shows that most penetrating deep convective clouds have IR signatures that are consistent with traditional IR techniques and that penetrating deep convective clouds have areal extents large enough to be resolved from conventional spaceborne passive sensor radiometers.

Table 3.1: Multi-satellite mean statistics for observations of deep convection reaching and penetrating 14 km and 16.9 km over the regions between 20°N - 20°S and 35°N - 35°S. The normalized frequency distributions corresponding to these observations are provided in Figures 3.3a and 3.3b.

	20°N - 20°S		35°N - 35°S	
Cloud Properties	CTH ≥ 14 km	CTH ≥ 16.9 km	CTH ≥ 14 km	CTH ≥ 16.9 km
# of Observations	643,716	26,840	736,443	30,528
# of Cloud Layers	1	1	1	1
†a $\overline{CTT}$ (K)	213.47	197.12	213.69	197.38
†b $\overline{CTH}$ radar-lidar (km)	15.82	17.31	15.77	17.32
†c $\overline{CBH}$ radar-lidar (km)	0.88	0.91	0.90	0.94
$\overline{CTH}$ radar (km)	14.59	16.60	14.58	16.62
$\overline{CBH}$ radar (km)	0.88	0.91	0.90	0.94
BTD (K)	-0.47	1.246	-0.49	1.253
$\overline{dBZe}_{max}$	13.207	14.278	13.254	14.269

†aCTT=Cloud Top Temperature, †bCTH=Cloud Top Height, †cCBH=Cloud Base Height

Table 3.2 Percent of occurrence of deep convection reaching 14 km and 16.9 km for cloud brightness temperatures at varying brightness temperature thresholds and positive BTD from 20°N - 20°S and 35°N - 35°S.

CloudSat/CALIPSO-MODIS	20°N - 20°S		35°N - 35°S	
Cloud Properties	CTH ≥14 km	CTH ≥16.9 km	CTH ≥ 14 km	CTH ≥ 16.9 km
Number of Observations	643,716	26,840	736,443	30,528
DC(IRWBT ≤ 235 K)	96.49	100.0	96.42	99.19
DC(IRWBT ≤ 210 K)	39.89	94.88	38.98	94.76
DC(IRWBT ≤ 200 K)	7.8	55.76	10.35	72.65
DC(+BTD)	59.42	91.53	58.96	91.63

Table 3.3: Framework for size distribution of penetrating tops provided in Figure 3.6.

# of Consecutive CloudSat Footprints	CPR Equivalent Area (km^2)	Area of Uniform Plume (km^2)
1	2.52	3.24
2-4	10.08	51.84
5-7	17.64	158.64
8-10	25.2	324
11-13	32.76	547.56
14.17	42.84	936.36

Table 3.4 Ratio of Plume Diameter as a function of varying chord lengths.

	Chord Ratio		
	Chord 1	Chord 2/Chord1	Chord3/Chord1
Diameter	x	.9x	.75x

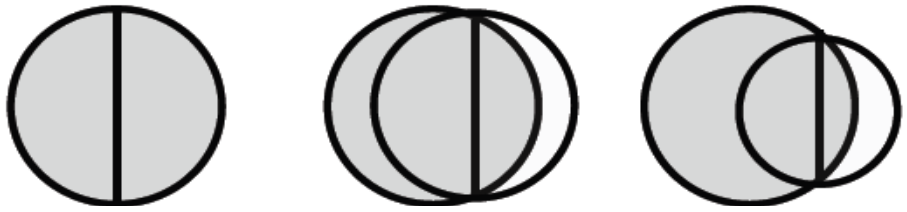

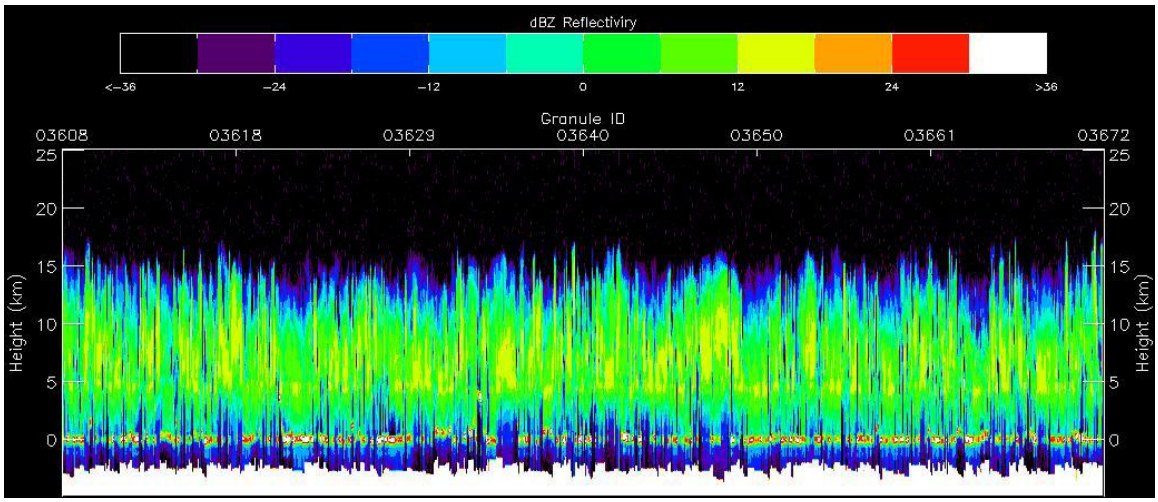

Figure 3.1: Concatenated reflectivity in dBZe of 10,000 of the 736,443 CPR profiles found with radar-lidar cloud top heights ≥ 14 km and radar heights ≥ 13 km.

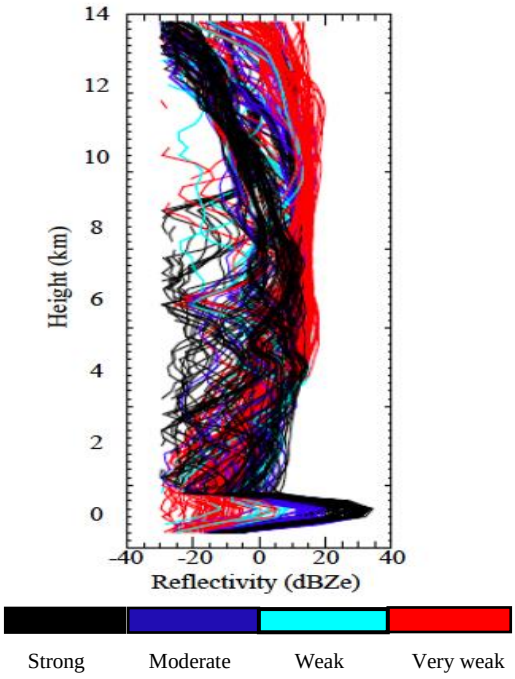

Figure 3.2: Reflectivity profiles of 200 of the 736,443 observations of penetrating deep convection classified by the strength of their surface echoes (ΔdBZe) with strong surface echoes having ΔdBZ > 20 dBZe; moderate echoes between 10 dBZe and 20 dBZe; weak echoes between 6 dBZe and 10 dBZe ; and very weak echoes < 6 dBZe.

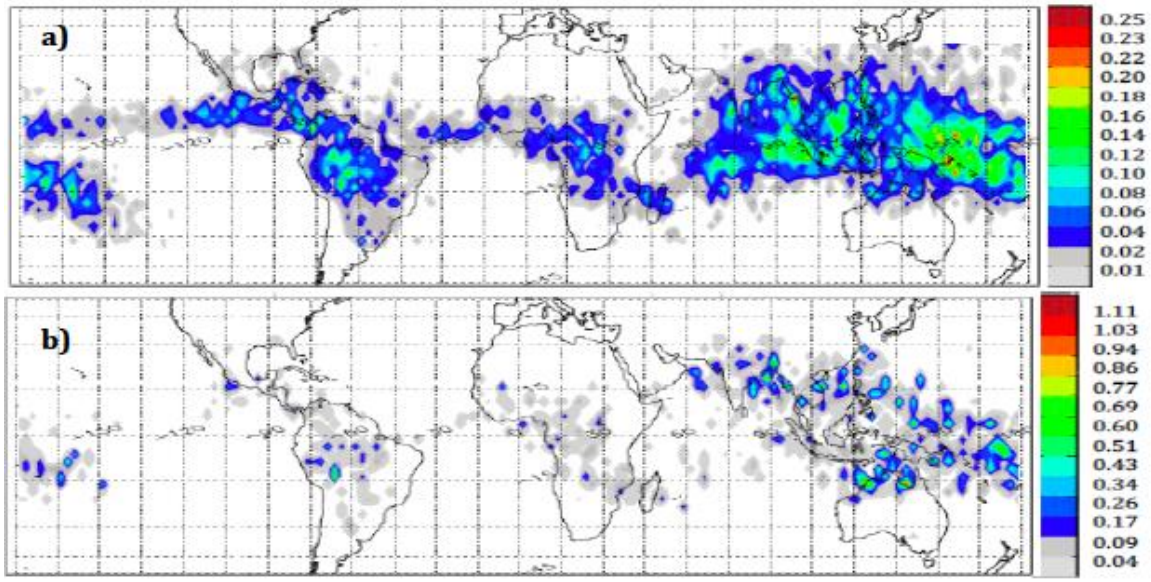

Figure 3.3: Frequency distribution of Cloudat/Calipso cloud tops a) ≥14 km and b) ≥16.9 km over 35°N ─35°S for 2007 organized according to 2.5° x 2.5° bins where the total of each distribution is 100%.

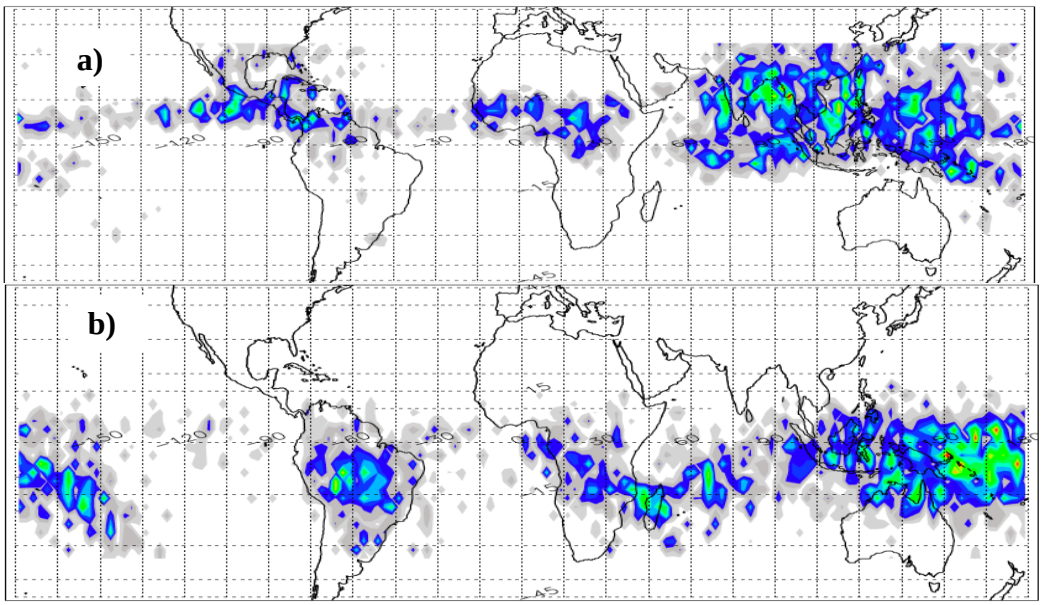

Figure 3.4: Same as Figure 3.3 except distribution is for a) June-July-August (JJA) and b) December-January-February (DJF).

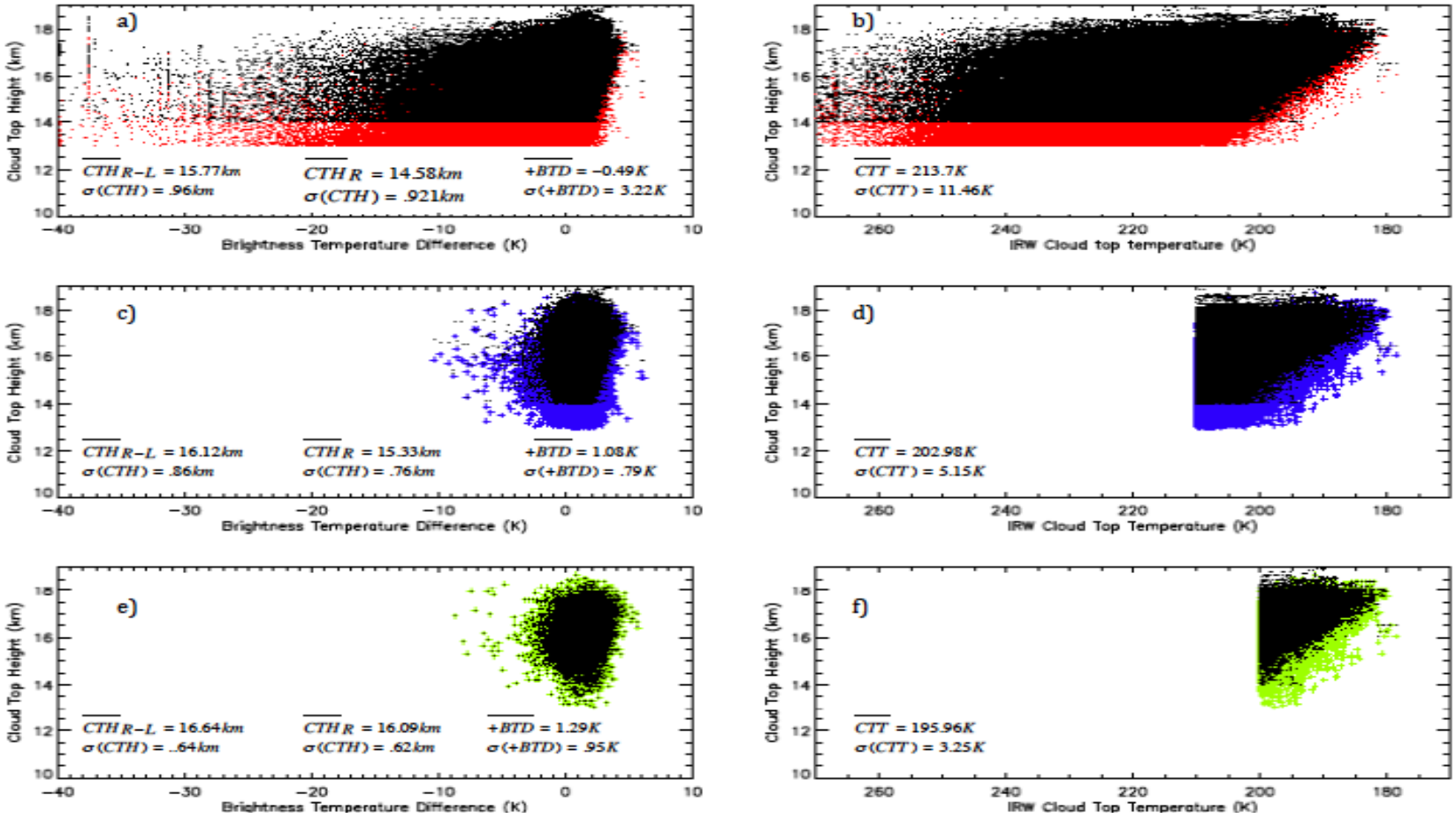

Figure 3.5 Radar-lidar (black) and radar (alternating color) cloud top height verses a) brightness temperature difference for all 736,443 observati ons b) cloud brightness temperatures for all 736,443 observations c) same as a) but with ≤ 210 K cloud brightness temperature constraint d) same as b) but with ≤ 210 K cloud brightness temperature constraint e) same as a) but for cloud brightness temperatures ≤ 200 K and f) same as b) but for cloud brightness temperatures ≤ 200 K.

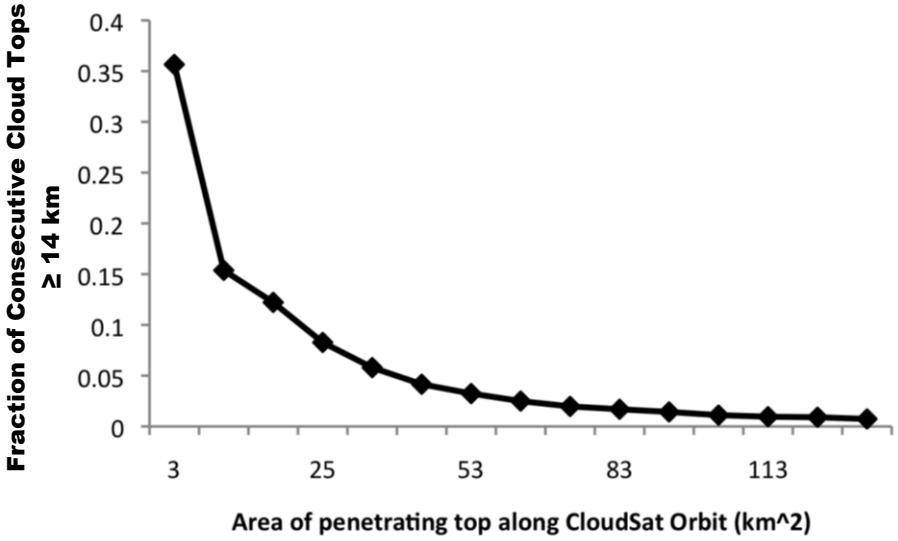

Figure 3.6: Areal size distribution in km^2 of penetrating deep convection with consecutive CPR footprints reaching 14 km. The distribution also corresponds to the criteria provided in Table 3.2 where the area associated with the penetrating deep convective cloud top is provided according to the maximum number of consecutive footprints associated with the CloudSat CPR footprint.

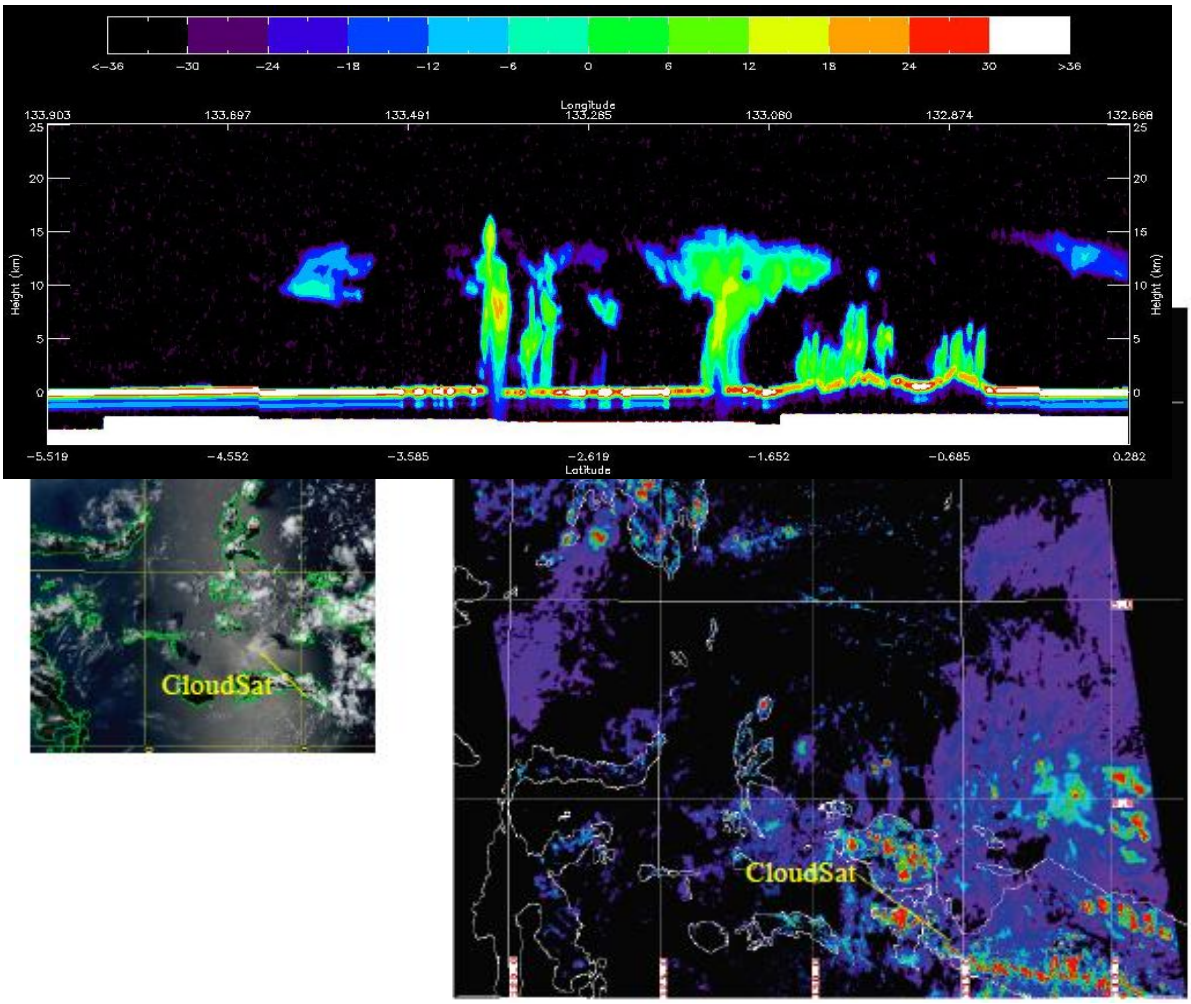

Figure 3.7: Top) CloudSat cross-section of a penetrating deep convective cloud (labeled A) with cloud top heights > 15 km and diameter of ~ 20 km. (Bottom left) Aqua MODIS (L1B) true color image with the CloudSat track corresponding to the top panel is shown in yellow and (Bottom right) Aqua MODIS cloud optical thickness from the level 2 cloud product with the CloudSat track also shown in yellow.

CHAPTER 4
EVALUATION OF TRADITIONAL IR TECHNIQUES

4.1 Introduction

Prior to the application of space-borne radar for the evaluation of deep convection reaching the TTL, several IR studies (e.g., Gettelman et al., 2002, Rossow and Pearl, 2007) evaluated the tropical frequency distribution of deep convection reaching the TTL. While those studies focused on assessing regional dominance and seasonal patterns (e.g. Rossow and Pearl, 2007), few studies evaluate the affects of penetrating deep convection on long-term trends in lower stratospheric water vapor.

To address this relationship, it is first important to assess the climatological properties of penetrating deep convection. While this is a challenge, it is not impossible. Visible and infrared observations have been collected and archived for nearly 30 years from geostationary orbit [Knapp, 2008a]; a wealth of data suited for climatological studies exist. Yet the potential information that may be obtained from such measurements is unclear. As shown in Chapter 3, the horizontal resolutions of the observations obtained from geostationary orbit will often limit the extent to which penetrating deep convection may be resolved. In addition to this limitation, brightness temperatures, which are most often used to define deep convection and penetrating deep convection, do not give an exact measure of cloud top height nor do they provide evidence of cloud vertical structure. Moreover, traditional IR techniques, which include cold cloud features and +BTD signatures, have been poorly quantified.

In Chapter 3, penetrating deep convective clouds from CloudSat showed +BTD signatures when IRW brightness temperature thresholds of 210 K and 200 K were

applied. However, there is still much uncertainty associated with the capabilities of +BTD signatures and the cold cloud feature technique to exclusively sample penetrating deep convective clouds. As described by Chou and Neelin [1999], cirrostratus and cirrocumulus are tightly connected with deep convective cloud fractions. When applying traditional IR techniques that include cold cloud features and +BTD signatures, both techniques are suggested to largely sample nonraining anvil clouds or thick cirrus in addition to the convective region. Therefore other approaches have been developed to detect penetrating deep convection from space-borne radiometers.

Aumann et al. [2011] used hyperspectral observations from the Advanced Infrared Sounder (AIRS) and the Atmospheric Microwave Sounding Unit (AMSU) to gain new insights into properties of cold cloud tops by identifying their spectral differences. The authors determined that the mix of cirrus and deep convective high clouds can be separated by noting differences between a window (8-11) channel and a channel with strong CO_2 absorption (near 14 μm). Aumann et al. found that differences between channels at these wavelengths distinguish a class of deep convective clouds characterized by a very high mean rain rate and a local upward displacement of the tropopause. The authors suggest that improved identification of penetrating cloud tops could be accomplished by adding one strong CO_2 sounding channel on future advanced geostationary satellites. Yet this approach does little to address the impact of penetrating deep convection on long-term trends in lower stratospheric water vapor from existing data.

Other newly developed techniques include objective satellite-based detection schemes presented by Bedka et al. [2010], which is reportedly less useful for historical IR

radiances that have horizontal resolutions ≥ 5 km and Berendes et al. [2008], who used visible radiances that limit the evaluation of penetrating deep convection to daytime detections only. Given these details, the techniques developed by Bedka et al. [2010] and Berendes et al. [2008] are considered here to be less appealing to adequately evaluate the climatological properties of overshooting tops using the historical data.

How then do we reduce and/or quantify the uncertainty associated with traditional IR methods that are most applicable to the historical observations? To determine how to best address this point, Alcala and Dessler [2002], Liu et al. [2007], and Luo et al. [2008] provide useful approaches on how to evaluate penetrating deep convection from space-borne IR and radar sensors. According to these studies and others like them, a multisensor view from space-borne sensors is a more accurate way to evaluate IR-based distributions and techniques used to detect penetrating deep convection. Such a view incorporates rather direct measures of cloud vertical structure and cloud top height from radar with passive sensor observations that indirectly provide cloud top height based on radiative transfer modeling and a priori assumptions of surface and atmospheric quantities. The benefit of the combined radar-IR approach is that it goes beyond the traditional top-down view associated with IR-imagers and has already been shown to yield insightful results (e.g., Luo et al., 2008; Luo et al., 2010; Chung et al., 2008). However, the scope of IR properties investigated in most radar-IR examinations of penetrating deep convective clouds limit themselves to IRW brightness temperatures while other optical and microphysical parameters such as optical depth (τ), cloud top pressure, effective particle radius, etc., are also available. It is interesting to evaluate whether the inclusion of additional optical and microphysical properties of cold cloud

features/pixels with $BT_{11} \leq 210$ provides the necessary evidence to better distinguish between the deep convective cloud core and corresponding anvil/cirrus cloud fractions.

In the assessment of the general macro- and microphysical properties of deep convection by Yuan and Li [2010], the authors define deep convective clouds with IRW brightness temperatures less than 243 K and cloud optical thickness greater than 40. Yuan and Li suggest that these thresholds screen out relatively thick, isolated cirrus clouds not associated with an active deep convective cloud, but keep portions of the anvil clouds associated with the deep convective systems. Kubar et al. [2007] suggests that anvil clouds have cloud tops colder than 245 K and optical depths between 4 and 32. However these descriptions of anvil clouds are rather arbitrary. Since CloudSat provides vertical cloud structure, the combination of CloudSat/Calipso and Aqua MODIS observations may be used to disentangle the description of deep convective cores from the surrounding cloud fraction to more objectively decipher between anvil and cirrus clouds. Using CloudSat, Aqua MODIS and the Advanced Microwave Scanning Radiometer for the Earth Observing System (AMSR-E), Yuan and Houze [2010] quantitatively mapped the frequency of anvil clouds within mesoscale convective systems (MCS) and non-MCS anvils over the entire tropics. However, they do not provide a complete range of microphysical and optical properties with which to distinguish penetrating tops and anvil clouds from radiometric observations.

Given these details, cold cloud features/pixels and positive BTD signatures are compared with penetrating deep convective clouds gathered in Chapter 3. The comparison of these three sets of observations are used to statistically characterize the extent to which traditional passive sensor approaches are able to exclusively capture

overshooting deep convection and to evaluate, to the extent possible, the percentage of other types of high level clouds (i.e., anvil clouds, pileus clouds, jumping cirrus, lower level deep convection, etc.) that may be present in the IR distributions. In addition, Chapter 4 also compares the microphysical and optical properties of penetrating deep convection with other types of high clouds. By evaluating these properties the capabilities and information content of IR-based distributions of penetrating deep convection are better understood and their capability to detect penetrating deep convective cloud tops is revealed. More specifically, the combination of CloudSat/CALIPSO and Aqua MODIS observations are used to address the following:

1. *To what extent is penetrating deep convection exclusively captured using traditional IR methods and does this information change the perception of the frequency distribution of penetrating deep convection as presented in other IR studies?*
2. *What are the microphysical and optical properties of penetrating deep convection in comparison with other high level clouds? How does the incorporation of these parameters aide in the evaluation of penetrating deep convective clouds using traditional IR techniques?*

To address these questions, section 4.2 provides additional background information on traditional IR techniques and the studies that have used them to investigate penetrating and overshooting deep convection. Section 4.3 describes the data and methods that have been developed to conduct these analyses. In Section 4.4 the results of the analysis are presented where we focus on the two questions outlined above.

Finally, section 4.5 summarizes the chapter and ideas for future work (i.e., a prelude to Chapter 5).

4.2 Characterization of Penetrating Deep Convection from Spaceborne IR Data

Much work has been done to detect and characterize the influence of overshooting deep convection on the tropical tropopause layer and lower stratospheric water vapor budget (e.g., Jiang et al., 2004; Hong et al., 2005; Heymsfield and Fulton,1988; Cifelli et al., 2002; Nesbitt et al. 2006; Bedka and Minnis, 2010). While all these studies have contributed to the understanding of penetrating deep convection, below the focus is on studies that used observations from space-borne satellite IR imagers/sounders.

Two approaches are commonly used to gauge the frequency and distribution of penetrating/overshooting deep convection using data from conventional passive-sensor satellite radiometers. They include, cold cloud features/pixels (e.g., Mapes and Houze 1993; Liu et al, 2007; Rossow and Pearl, 2007) and positive brightness temperature differences between the water vapor absorption band at ~6.7 μm and the IR window at ~11 μm (e.g., Schmetz, 1987; Soden, 2000; Setvak et al., 2003; 2007; Chung et al., 2008). While these approaches have been briefly discussed we now offer a more physical explanation of the two techniques.

The physical basis for the cold cloud feature approach is associated with classical parcel theory and observations showing that once deep convection overshoots its level of neutral buoyancy the cloud top is much cooler than its environment [Johnston and Solomon, 1979]. Consequently, deep convective clouds colder than their level of neutral

buoyancy, or some other critical level, have been estimated to have cloud tops that lie at higher altitudes.

In the second approach, positive brightness temperature differences (+BTD) occur when deep convective clouds with very strong updrafts force water vapor and ice into the lower stratosphere. The water vapor that enters the lower stratosphere emits radiation in the infrared water vapor absorption band (5.7 ─7.1 μm) at warmer stratospheric temperatures while the infrared window (~11 μm) brightness temperature is emitted from the lower and colder physical cloud top. The +BTD signature associated with overshooting deep convection was first detected by Fritz and Lazlo [1993] who used the High Infrared Resolution (HIRS)/TIROS-N Satellite Sounder to monitor very high clouds. Fritz and Lazlo [1993] also used the atmospheric radiation code (ATRAD) to make theoretical radiance calculations in effort to physically explain the nature of the +BTD signature. By placing optically thick clouds at the base of the tropical tropopause level the authors simulate brightness temperatures in both the IRW (~11 μm) and in the infrared water vapor absorption band (~6.7 μm) that support their interpretation of the +BTD signature.

Using cold cloud features/pixels and +BTD signatures from IR observations, many details of the global frequency distribution of overshooting convection distinguished as the coldest deep convective cores and cirrus/anvil cloud fractions have been presented. To disentangle deep convective cores and cirrus/anvil cloud fractions Fu et al. [1990] used ISSCP radiance data for July 1983 and January 1984 over the equatorial Pacific. Their results show that when cloud brightness temperature becomes warmer than 220 K the distribution of deep convective cloud cover shifts to lower

reflectance which is indicative of cirrus and anvil cloud fractions. Fu et al. [1990] that an IRW brightness temperature of 220 K is a good threshold to isolate deep convective clouds. However, Hong et al. [2006] analyzed the diurnal cycle of deep convective clouds using the infrared threshold technique and suggest that the peak in $BT_{11} \leq 210$ K and $\leq$ 235 K distributions has a 2-hour lag behind the maximum TRMM PR deep convective cloud fractions. The authors suggest that this 2-hour lag is a consequence of anvil cloud shield expansion, indicating that the 210 K distribution is influenced by cirrus-anvil cloud fractions.

For the evaluation of penetrating tops within the deep convective core, Gettelman et al. [2002] used a combination of cold cloud features less than the cold point tropopause temperature to show that tropical overshooting deep convection occur more frequently over the tropical oceans compared with continental regions and that the highest frequencies occur over the western tropical Pacific. Gettelman et al. [2002] also integrated the global frequency distribution of overshooting events to estimate what percentage of overshooting tops that occur within the larger distribution of deep convective clouds. Using observations with a 50 km horizontal resolution, their study suggests that approximately 0.5% (± 0.25%) of all deep convection fits the description of overshooting deep convection. Yet it is difficult to apply observations with a 50-km resolution to evaluate updrafts and penetrating towers with diameters that are typically on the order of 1–10 km. Gettelman et al. state that differences in the scale of penetrating and overshooting deep convection verses the horizontal resolution of the data introduce uncertainties when estimating the cloud fraction of overshooting deep convection from the global cloud imagery.

Rossow and Pearl [2007] used IR data from the ISCCP-DX dataset to conduct a 22-year survey of deep convection penetrating the TTL. They show that land events exhibit a diurnal cycle while oceanic events do not exhibit this same character. Rossow and Pearl [2007] also add that penetrating deep convection predominantly occurs in the larger, organized mesoscale convective systems and that the interannual variations in the seasonal patterns of overshooting events are "not very large". Using 5 km observations subsampled to a 30 km horizontal resolution they report that ~ 2% of deep convection penetrates the TTL. Results of IR and radar studies that have sampled penetrating deep convection and provide estimates of their fractional coverage are given in Table 4.1. As indicated, the fraction of penetrating deep convection ranges from values as high as 5% from radar studies [Alcala and Dessler, 2002] to values as low as 0.5% (±.25%) in IR studies [Gettelman et al., 2002]. With the exception of Liu et al. [2007] none of the studies given in Table 4.1 quantify what fraction of the cold cloud features/pixels correspond to penetrating deep convective clouds.

4.3 Data and Methods

The characteristics of penetrating/overshooting deep convective clouds are evaluated with high/cirriform, deep convection, and anvil clouds for January 2007 over 35°N to 35°S. The same CloudSat products used in Chapter 3 are used to identify all four cloud types but with a few modifications. Here, the CloudSat 2B-CLDCLASS product is used to determine the locations of cirriform and deep convection. These two cloud classes are identified by the 2B-CLDCLASS product as cloud classes 1 and 8, respectively (refer to Table 2.2). Anvil and penetrating deep convection are not characterized by the 2B-CLDCLASS product but are subcomponents of the larger deep convective cell. These

two cloud classes are identified by considering the vertical and spatial properties of each deep convective cloud that is captured along the CloudSat profile (see Figure 4.1).

The criteria for penetrating and overshooting deep convection were presented in Chapter 3. For anvil clouds it is important to consider the distribution of cloud classes within the deep convective cell as they relate to each vertical range gate. A schematic view of the classification of the anvil cloud, the penetrating top, and the main body of the deep convective cloud are shown in Figure 4.1 with examples of vertical and horizontal range gates given. As indicated in Figure 4.1 anvil clouds are identified when deep convective clouds (8) are present with high cirriform (cloud class 1) connected to them and no cloud (0 - not shown) beneath. For each of the four cloud groups the 2B-GEOPROF product is used to evaluate cloud top height, cloud base height, and cloud masks values, where cloud masks values ≥ 30 are again required to confirm the presence of the cloud. Each cloud's vertical boundaries are further characterized using the 2B-Lidar-GEOPROF product with the condition that only 1 cloud layer may be present in the CPR profile. All observations are recorded with date, time, and geolocation information in order to evaluate other microphysical and optical properties associated with each cloud group from MODIS-AUX and MAC06S0 products. Data sampling from the MODIS-AUX product is the same as in Chapter 3. For the MAC06S0 product, which provides effective radius, cloud top pressure, particle phase, and optical depth, sampling works differently. As described in Chapter 2, the MAC06S0 product provides 3 pixels by 11 pixels with an approximate resolution of 15 km x 10 km. Given these details, MAC06S0 pixels that are geographically closest to each CloudSat observation are used to a provide

an averaged 5 km x 5 km view of effective radius, cloud top pressure, particle phase, and optical depth.

In addition to gathering observations of the four cloud classes for January 2007, IR observations of cold cloud features ≤ 235 K and ≤ 210 K, and +BTD (with $BT_{11} \leq 235$ K) for all of 2007 are sampled and compared with observations of penetrating deep convective clouds. In this part of the approach, all MODIS-AUX observations where the innermost 3 km x 3 km subset has an average IRW brightness temperature (BT_{11}) ≤ 235 K and ≤ 210 K is used to identify cold cloud features ≤ 235 K and ≤ 210 K. Positive BTD (+BTD) signatures are similarly evaluated. Observations are recorded with time, date, and geolocation information. MODIS-AUX observations of cold cloud features and +BTD are then cross-referenced with CloudSat observations of penetrating deep convection to determine the extent to which traditional IR techniques exclusively sample penetrating deep convection.

4.4 Observations from Aqua MODIS

In this section, the optical and microphysical properties of penetrating deep convection from MODIS is compared with other types of high clouds and distributions of cold cloud features ≤ 210 K and +BTD signatures are also characterized.

4.4.1 Penetrating Deep Convective Clouds Compared with Other High Clouds

Mean optical and microphysical properties listed in Section 4.3 are provided in Table 4.2 for high/cirriform, deep convection (with radar-lidar cloud top heights < 14 km), anvil clouds, and penetrating deep convection where penetrating deep convection is evaluated according to cloud top heights ≥ 14 km and ≥ 16.9 km observed during January 2007. As shown in Table 4.2, rather strong distinctions associated with each

cloud type occur for cloud top pressure, IRW brightness temperature, BTD signature, and optical thickness. While the definition of high clouds and deep convection from the 2B-CLDCLASS product is different from the classification of high clouds (i.e., cirrus, cirrostratus, and deep convection) provided from the ISCCP scheme, the average statistics of the four cloud types examined in this study suggest that the sampling technique is highly useful. With the exception of IRW brightness temperatures, which are reported here in lieu of cloud top temperature, statistical means reported in Table 4.2 are consistent with values reported in other studies (e.g., Hong et al., 2007; Rossow and Schiffer, 1999). Additional information on each cloud class has been gathered by examining how these microphysical and optical properties are distributed about their means.

In Figure 4.2, the normalized frequency distribution of a) BTD signature, b) IRW brightness temperature, c) cloud optical thickness (τ), d) infrared water vapor brightness temperature e) cloud top pressure and f) effective particle radius is given. According to the BTD distribution, there is general agreement among deep convection, penetrating deep convection, and anvil clouds where each of these cloud types has peak BTD values between ± 2 K. For IRW brightness temperatures, penetrating deep convection ≥ 16.9 km has a narrow distribution and a peak value around 193 K while penetrating deep convection ≥ 14 km has a broader distribution of IRW brightness temperatures that range from 190 K to 230 K. Anvil clouds have a peak IRW brightness temperature of 237 K suggesting that on average, anvil clouds are warmer than penetrating deep convection although some anvil clouds do have relatively low temperatures where penetrating deep convection (≥ 14 km and ≥ 16.9 km) dominates. In comparison to all deep convection,

observations of cirrus clouds have relatively warm IRW temperatures (i.e., $BT_{11} > 220$ K) when compared with all of deep convection and anvil clouds.

For each of the four cloud classes the spectrum of optical thickness is skewed towards low values. For cirrus, anvil clouds, deep convection and penetrating deep convection the mean optical depth is 6.8 ± 13.7. While low optical thickness is characteristic of cirrus and even anvil clouds, low optical thickness is not characteristic of deep convective clouds. This aspect of the observations likely represents a problem with spatial sampling since optical thickness from the MAC06S0 product is reported at a 5 km resolution and deep convective clouds typically have optical thickness > 23 (see Figure 2.2). While the 5-km spatial resolution may be too large to accurately identify the properties associated with relatively small deep convective cells, as in the case of Figure 3.7, optical depth measurements may be very useful in characterizing penetrating deep convective clouds from IR observations. On the other hand, these rather low optical depth values may be due to the criteria for deep convective clouds that is utilized in the 2B-CLDCLASS product (see Chapter 2). Therefore the relationship between IRW brightness temperature and optical thickness is evaluated in Figure 4.3. This figure shows that IRW brightness temperatures for both cirrus and deep convective clouds are typically warmer when optical thickness is low. Approximately 79% of all IRW brightness temperatures > 235 K had optical depths less than 23 while this value is 65% for all IRW brightness temperatures ≤ 235 K. Since these two statistics are similar the oddities in optical depth may again be due to the 5 km sampling.

The distribution of IR water vapor brightness temperature in Figure 4.4 shows the lowest peak values for penetrating deep convective clouds. Distributions of cloud top

pressure show that the majority of penetrating deep convection ≥ 16.9 km have cloud top pressures < ~120 mb. As in the case of IRW brightness temperature, penetrating deep convection ≥ 14 km also has a broad distribution in cloud top pressure. The distribution of effective particle radius is somewhat similar for all cloud types although the largest values occur for penetrating deep convection (≥ 14 km and ≥ 16.9 km).

To further illustrate the variability IRW brightness temperature, IR water vapor brightness temperature, and +BTD as a function of cloud type from collocated Aqua MODIS and CloudSat measurements provided in Figure 3.7 (shown in Chapter 3) is used again and are provided in Figure 4.4. As shown in Figure 4.4, CloudSat granule ID 2757 is used to highlight observations of a stratocumulus cloud (labeled A), deep convective clouds (labeled B and C) and a cirrus cloud (labeled D). As indicated, penetrating deep convective clouds are the only cloud types within the cross section with IRW brightness temperatures ≤ 210 K. Anvil clouds are at levels slightly below 14 km. Although the anvil portion of the deep convective cloud does not have IRW brightness temperatures below 210 K, some observations of anvil clouds do have IRW brightness temperatures that are this low.

The BTD profile corresponding to the CloudSat cross section shows slightly positive values for the stratocumulus cloud (cloud A) referenced in Figure 4.4. Slightly positive BTD values show that while +BTD signatures are often associated with deep convective clouds, +BTD signatures can also occur in the presence of other optically thick cloud types. This suggests that +BTD signatures explained by an increase in water vapor entering the lower stratosphere due to the transport of water vapor rich air from the updrafts of deep convective cores, does not suitable in all cases where +BTD signatures

occur. More highly positive +BTD signatures may be related to lower stratospheric water vapor pumping as in the case of the overshooting deep convection cloud (cloud B) labeled in Figure 4.4. However, more research is necessary to provide evidence that supports this explanation.

While results provided in this section are only for January 2007, they have been used to statistically characterize and investigates IRW brightness temperatures and other microphysical and optical properties of penetrating deep convection with other types of high clouds. Characterization of cold cloud features and positive BTD signatures are provided in the next section.

4.4.2 Characterization of cold cloud features and positive BTD signatures

The frequency distribution of MODIS-AUX cold cloud features ≤ 235 K and ≤ 210 K are provided for 35°N to 35°S and are given in Figure 4.5 along with the seasonal properties of the 210 K distribution during December-February and June-August. Regional similarities in the distribution of cold cloud features ≤ 210 K largely agree with the distribution of deep convection penetrating 14 km (Figure 3.3) provided in Chapter 3 and is also consistent with the distribution of +BTD signatures between 35°N – 35°S provided in Figure 4.6.

Dominant regions in distributions of cold cloud feature (≤ 235 K and ≤ 210 K) and +BTD are both associated with the large-scale dynamical structure of the tropical atmosphere [Webster and Chang; 1988]. Regional patterns in Figures 4.5 and 4.6 are consistent with IR studies (e.g., Gettelman et al, 2002) that show that the highest densities of deep convective clouds are found in the Indian and west tropical Pacific Oceans, over South and central America and Africa. In addition, the seasonal distribution of +BTD and

cold cloud features ≤ 210 K also show the migration of the ITCZ as in the case of penetrating deep convective clouds shown in Figure 3.5. Although these results provide a good basis for qualitative comparison, it is important not to limit the observations to qualitative comparisons only. Without quantitative information that compares cold cloud feature and +BTD distributions with the distribution of penetrating deep convective clouds we limit new possibilities for interpretation that might otherwise go unutilized.

4.4.3 Cold cloud features and +BTD compared with CloudSat observations

The spatial and vertical properties of penetrating deep convection are provided in Chapter 3. Results reported in Chapter 3 Table 3.3 show that within the tropics (20º N-20º S) 57% of all deep convective clouds reaching 14 km have IRW brightness temperatures between 235 K and 210 K, ~40% have IRW brightness temperatures ≤ 210 K and ~59% exhibit the +BTD signature. These statistics identify what fraction of the complete distribution of deep convection reaching 14 km is observed using each technique. However, they do not quantify what fraction of all cold cloud features and +BTD are penetrating deep convection. Quantifying this information is necessary to determine the extent to which cold cloud features and +BTD exclusively sample penetrating deep convective events. These results are provided in Table 4.3.

Results from Table 4.3 were determined by cross-referencing observations of MODIS-AUX cold cloud features ≤ 235 K and ≤ 210 K and +BTD with CloudSat (radar-lidar) penetrating deep convection. As shown in Table 4.3, the percentage of cold cloud features ≤ 235 K and ≤ 210 K and +BTD that occur as penetrating deep convection reaching 14 km is ~ 26%, 66% and 55% respectively. For cold cloud features ≤ 210 K, the value of 66% reported here is much higher than the value of 1% reported by Liu et al.

[2007], who provide the only other study that used radar observations to address the relationship between cold cloud features ≤ 210 K and penetrating deep convection. Given these differences it is important to further investigate the validity of the quantitative results by evaluating the types of high clouds that we expect to observe at $BT_{11} \leq 210$ K. Here, CloudSat granule ID 2575 previously provided in Figure 3.7 (Chapter 3) and Figure 4.4 is further assessed. However, in this case MODIS L1B (MYD021KM) IRW brightness temperatures sampled to a 5 km x 5 km resolution and corresponding cloud top temperatures from the level 2 Aqua MODIS Cloud Product (MYD06_L2) are evaluated and shown in Figure 4.7.

As shown in the images of cloud top temperature and IRW brightness temperature provided in Figure 4.7, cloud top temperature and BT_{11} values ≤ 210 K and ≤ 235 K have been distinguished by yellow and red contour shading. The image of cloud top temperature has ~6% more pixels with temperatures ≤ 210 K and 17% more pixels with cloud top temperatures ≤ 235 K. The difference in the percentage of pixels ≤ 235 K and ≤ 210 K that exists between the two images is largely based on the CO_2 slicing method which is used to derive MODIS L2 cloud top temperature. Using the CO_2 method, a considerable fraction of optically thin cirrus clouds are better represented in the image of cloud top temperature. This indicates that thin cirrus, which makeup a considerable fraction of all high clouds, are radiometrically less visible in the IRW region.

According to Figure 4.7 approximately 0.4% of pixels with IRW brightness temperatures ≤ 235 K are also ≤ 210 K. When IRW brightness temperatures ≤ 210 K are compared with the corresponding image of optical thickness (provided in Chapter 3 Figure 3.7) where $\tau \geq 23$, all pixels with IRW brightness temperatures ≤ 210 K occur

with pixels that have optical depths ≥ 23. This relationship suggests that the majority of clouds with IRW brightness temperatures ≤ 210 K are also deep convective clouds. This relationship has also been evaluated in Figure 4.8, which shows the normalized frequency distribution of optical depth ranging from 0 to 100 for all observations of BT_{11} ≤ 210 K sampled from 5 km resolution data from the Aqua MODIS L2 Cloud Product during October 2007. According to Figures 4.7 and 4.8 the most probable cloud class with IRW brightness temperatures ≤ 210 K is deep convection with rather high optical depth. This finding is further supported by Table 4.5 which shows that ~85% of all pixels with BT_{11} ≤ 210 K are associated with deep convective clouds. While anvil clouds may be optically thick and classified as deep convection, a statistical evaluation of their macro and microphysical properties (i.e., optical depth, cloud top pressure, and cloud top height) have not been reported in any other studies. According to the analysis performed in the previous section anvil clouds have mean IRW brightness temperatures of 237± 21.9 K and have optical thicknesses of 6.8 ±13.7. These values indicate that some of the cloud features observed at IRW brightness temperatures ≤ 210 K may be associated with anvil clouds especially since 30.8 % of pixels with BT_{11} ≤ 210 K have optical depths le 34.2. Given these details, the high fraction (i.e., 66%) of cold cloud features ≤ 210 K that are associated with deep convective clouds with (radar-lidar) cloud top heights ≥ 14 km is a reasonable result. Other IR thresholds are also considered in Table 4.4. These results show that at sufficiently low IR thresholds, BTD signatures are also positive.

4.5 Summary and Discussion

There is no precise definition of a deep convective cloud from passive remote sensing measurements that admits all penetrating deep convective clouds while filtering out all other cloud types. However, the fraction of cold cloud features/pixels with $BT_{11} \leq$ 210 K and +BTD signatures that are penetrating tops may be quantified to enhance the information content and applicability of these techniques for climatological studies. For cold cloud features ≤ 210 K the only existing estimate on the fraction of cold cloud features ≤ 210 K is rather low according to Liu et al., [2007] and rather high for positive BTD signatures according to Chung et al., [2008]. As a consequence, the distribution of cold cloud features ≤ 210 K and +BTD signatures have been evaluated against radar and IR microphysical and optical cloud properties associated with penetrating deep convection and other types of high clouds to evaluate extent to which penetrating deep convection is exclusively captured using traditional IR methods. According to this evaluation, ~ 66% of cold cloud features/pixels with IRW brightness temperatures ≤ 210 K are associated with penetrating deep convective clouds. This conclusion is further supported by the evaluation of $BT_{11} \leq 210$ K pixels with cloud optical depth for October of 2007 which shows that ~ 86% of all clouds with $BT_{11} \leq 210$ K have optical depths greater than 23. Since several studies suggest that IR techniques sample considerable fractions of thick cirrus and non-raining anvil clouds in addition to the deep convective region a description of microphysical and optical properties of anvil clouds was provided in section 4.4.1. According to the observations associated with this cloud type, anvil clouds may have optical depths of 6.7±13.7, which at two standard deviations is τ=34. $BT_{11} \leq 210$ K with $\tau \leq 34.1$ is 30.7% of the $BT_{11} \leq 210$ K distribution and still supports,

the evaluation that 66% of cold cloud features ≤ 210 K is associated with penetrating deep convective clouds. Yet for the analysis of these statistics it is also important to note that optical depth provided from MODIS suffers from a poor dynamical range especially in comparison to ISCCP which characterizes deep convective clouds with optical depths as high as 379 (see Figure 2.2) since MODIS cloud optical depth retrievals saturate at 100.

The implication of the cold cloud feature result suggest, for example that IR based studies which propose that penetrating deep convection is 0.5%±0.25% of all deep convection (cf., Gettelman, 2002), is a rather low estimate that is more so due to the horizontal resolution of the observations combined with the spatial scale of penetrating tops, rather than inadequacy of the cold cloud feature technique. However, it has also been shown that a considerable fraction of penetrating tops do not have cloud brightness temperatures ≤ 210 K according to the results of Chapter 3 which are consistent with *Luo et al*., [2008]. These issues prevent a more accurate estimate of the penetrating top cloud fraction to be revealed from IR observations especially in comparison to radar studies that report values as high as 5% [Alcala and Dessler, 2002] (see Table 4.1).

To better understand the types of clouds that are observed from cold cloud features ≤ 210 K and positive BTD signatures, four different types of high clouds were analyzed. This analysis shows that cirrus, anvil clouds, deep convection and penetrating deep convection, all have distinctions in optical and microphysical properties that could be used to better separate penetrating deep convection from other high cloud classes and has been used to further support the interpretation of the cold cloud feature ≤ 210 K distribution. The evaluation of +BTD, show that these signatures are present in cases of

optically thick high clouds, higher +BTD thresholds of (>.5K) are evident for penetrating deep convective clouds and may serve as a more useful application of BTD signatures. Although each cloud type was observed to have a range of IRW brightness temperatures penetrating deep convection (≥ 14 km and ≥ 16.9 km) have the lowest mean IRW brightness temperatures. This result is in agreement with the cold cores outlined by Yuan and Houze [2010] who quantitatively mapped the areal extent of MCS anvils, by distinguishing between the deep convective cloud and surrounding cloud fractions.

An interesting outcome in the analysis of high clouds does however show that some observations characterized by the 2B-CLDCLASS product as deep convection, do not have corresponding MAC06S0 optical depths > 23. This suggests that in some cases, either the 5 km x 5 km spatial resolution is too coarse to provide collocated measurements of optical thickness and other microphysical and optical properties or the LWP > 0 (see Chapter 2) criteria may not be suitable enough to specifically sample deep convective clouds characterized by optical depths ≥ 23. According to the analysis of cirrus and deep convective clouds as a function of BT_{11} and optical depth, we do not agree with Hong et al. [2006], who suggest that deep convective clouds and cirrus clouds with similar cloud top altitude cannot be distinguished. Here, it has been shown that in general, high clouds with varying degrees of optical thickness will have different IRW emission temperatures. Cirrus clouds typically have rather warm IRW brightness temperatures, while deep convective clouds, are a bit more complicated due to the different dynamic and thermodynamic processes.

In the analysis of cold cloud features ≤ 210 K with observations of penetrating deep convective clouds, the evaluations shown in Chapter 4 suggests that 66% of clouds

with IRW brightness temperatures ≤ 210 K are associated with penetrating deep convective clouds. While this statistic is much higher than the values reported by Liu et al., [2007], observations of $BT_{11} \leq 210$ K have also been analyzed with observations of optical depth. By using these two parameters, it has been shown that most observations of $BT_{11} \leq 210$ K are associated with deep convective clouds, of which the majority have very high optical depth. Although a few studies characterize the properties of anvil clouds, the mean optical depth of anvil clouds have not been shown to be associated with optical depths this high. Given these results, cold cloud features (≤ 210 K) and +BTD signatures, are both techniques that provide observations of penetrating deep convective clouds in comparison to other cloud types. This indicates that the IR threshold technique is a very useful approach to sampling and characterizing penetrating deep convective clouds. It is also indicates, that although Aumann et al. [2010] suggests that an additional CO_2 channel be added to geostationary satellites to observe severe weather associated with penetrating deep convective clouds it is likely unnecessary.

Table 4.1: Shows the relevant information for nine of the most popular studies on penetrating deep convection. These studies consist of passive and active space borne remote sensing.

Author	Year	Data Type	Data	Resolution	Vertical Resolution	Frequencies (GHz)	λ(μm)	Scope	Length	Penetrating Criteria	% Penetrating Convection
Schmetz	1997	IR	Meteosat-5	5 km x 5 km			6.7, 11	3.7°N-14.3°S, 17°E-36.2°E	January 22, 1996 06:OO UTC and 17:00 UTC	+BTD	1% (Meteosat)
Soden	2000	IR	GOES				6.7, 11	South and Central America	3 months, 06-08/97	+BTD	Not Reported
Gettelman	2002	IR	Global Cloud Imagery (Salby, 1991)	50 km x 50 km			11	30°N-30°S	3.5 years (October 1986 to February 1989 and October 1991 to September 1992)	GCI BT_{11}< Zonal Mean - Cold Point Tropopause	~0.5% (±0.25%)
Alcala and Dessler	2002	Radar and IR	TRMM-1C21 TRMM-2A23 VIRS-1B01	4.3 km X 4.3 km 4.3 km x 4.3 km 2 km x 2km	250 m 250 m n/a	13.8	10.8	30°N-30°S	4 months (January1998, July 1998, January 1999, July 1999)	Vertical Profile of 12 dBZ > 14 km	5%
Hong, et al.,	2005	Microwave	AMSU-B	15 km x 15 km		183.3±1, 183.3±3, 183.3±7		30°N-30°S	1 year (March 2003 to February 2004)	[⌘]$\Delta T_{17} \geq \Delta T_{13} \geq \Delta T_{37} > T_O$	~0.08%
Liu and Zipser	2005	Radar	TRMM-3A25	4.3 km x 4.3 km	250 m	13.8		35°N-35°S, 20°N-20°S	~5 years (01/98-11/01, and 12/01-12/03	Precipitation Features w/ 20 dBZ > 14 km	~0.008%
Rossow and Pearl	2007	IR	ISCCP-DX	5 km x 5 km (subsampled-30 km)			11	45°N-45°S	22 year (July 1983- June 2005)	Convective Clusters w/ a Mnimum Cloud top Temperaure > Cold Point Tropopause Temperature	2%
Liu et al.	2006	Radar and IR	TRMM-3A25 TRMM-VIRS	4.3 km x 4.3 km 2 km x 2 km	250 m n/a	13.8	10.8	36°N-36°S, 20°N-20°S	6 years [§](1998–2001 and 2003–2004)	Precipitation Features w/ 20 dBZ > 14 km	Tropical Tropopause Layer - 1.3% Cold Point Tropopause - 0.1%
Luo et al.	2008	Radar and IR	CloudSat MODIS	1.4 km X 1.8 km 1 km x 1 km	30 m n/a	94	11.08	15°N-15°S 15°N-15°S	1 year (January 2007 - December 2007)	Radar-Precipitation Features w/ 20 dBZ > 14 km IR- Cold Cloud Features (< 210 K)	Tropical Tropopause Layer - 1.9% Cold Point Tropopause - 1.3%

[⌘]Subscripts of ΔT represent the ± offset associated with the three 183.3 GHz channels

[§] In the 6-yr data August 2001 is replaced with August 2002 data.
(~17.92 km2 before the satellite orbit change and ~20.35 km2 after the orbit boost)

Table 4.2: Mean optical and microphysical properties for various types of high clouds derived from MODIS L2 Cloud Product along the CloudSat orbital track (MAC06S0) for January 2007.

Cloud Type	High Cloud	Deep Convection	Penetrating Deep Convection		Anvil
Cloud top height	> 12 km	< 14 km	≥ 14 km	≥ 16.9 km	> 12
Cloud top Pressure (mb)	215.504	276.177	143.0	112.023	187.66
IRW Brightness Temperature (K)	264.277	240.725	211.001	199.31	237.64
Optical Thickness	2.629	27.241	24.1074	27.23	6.8081
Effective Radius (μm)	24.5843	28.956	29.422	29.396	26.56
Cloud Particle Phase	2.271	2.751	2.008	2.0004	2.069
+BTD (K)	-30.5585	-7.841	-0.1951	1.3701	-11.766
Cloud Fraction (%)	0.9444	0.9993	0.9999	1	0.9925
# of Cloud Layers	1	1	1	1	1
Lidar Cloud Base Height (km)	10.779	0.777	0.945	0.958	4.162
Lidar Cloud Top Height (km)	14.885	11.769	16.218	16.871	15.94

Table 4.3: Percent of occurrence of deep convection reaching 14 km and 16.9 km with cold cloud features from 20°N─20°S and 35°N─35°S.

a) MODIS – CloudSat/CALIPSO	20°N - 20°S	35°N – 35°S
No. CCF ≤ 235 K	2,397,205	3,248,761
No. CCF ≤ 210 K	422,026	471,416
No. +BTD	699,789	829,973
%CCF(DC14) ≤ 235 K	25.91	22.67
%CCF(DC16.9) ≤ 235 K	1.12	0.93
%CCF(DC14) ≤ 210 K	65.49	60.90
%CCF(DC16.9) ≤ 210 K	6.03	6.14
%+BTD(14)	54.66	52.33
%+BTD(16.9)	3.51	3.37

Table 4.4**:** Properties of cold cloud feature distributions and penetrating deep convection reaching 14 km and cold cloud features from 20°N ─20°S and 35°N ─35°S.

IR Threshold	CPR Height (km)			Lidar Height (km)			MODIS IRW BT (K)			BTD			%POT	% CCF≤235K
	min	mean	max	min	mean	max	min	mean	max	min	mean	max		
IRWBT ≤ 235	5.16	13.61	18.71	6.15	14.89	18.94	178.62	217.24	235.0	-16.52	-0.78	6.15	25.91	100%
IRWBT ≤ 230	5.16	13.86	18.71	6.15	15.10	18.94	178.62	214.99	230.0	-14.03	-0.25	6.15	25.14	99.09
IRWBT ≤ 225	5.16	14.16	18.71	6.15	15.35	18.94	178.62	212.36	225.0	-12.11	0.22	6.15	28.72	80.3
IRWBT ≤ 220	5.17	14.49	18.71	6.15	15.60	18.94	178.62	209.45	220.0	-12.11	0.60	6.15	38.53	51.77
IRWBT ≤ 215	5.17	14.84	18.71	7.00	15.85	18.94	178.62	206.34	215.0	-10.37	0.88	6.15	51.86	30.04
IRWBT ≤ 210	5.17	15.20	18.71	7.57	16.09	18.94	178.62	203.06	210.0	-10.37	1.07	6.15	65.49	16.35
IRWBT ≤ 205	5.17	15.59	18.71	11.90	16.35	18.94	178.62	199.61	205.0	-10.37	1.19	5.69	78.81	7.93
IRWBT ≤ 200	5.27	16.02	18.71	13.81	16.64	18.94	178.62	195.96	200.0	-8.719	1.30	5.69	93.67	3.1

Table 4.5: Percent of $BT_{11} \leq 210$ K pixels provided according to cloud type and cloud optical thickness for different latitudinal bands where data was derived from the Aqua MODIS Level 2 Cloud Product for October 2007.

	Cloud Optical Depth								
	Cirrus		Cirrostratus		Deep Convection				
Region	0	3.6	9.4	20	23	43	63	83	100
15°N-15°S	.12	1.59	10.38	3.64	24.44	14.44	8.62	3.29	33.46
20°N-20°S	.12	1.59	10.25	3.62	24.63	14.92	8.51	3.22	33.12
35°N-35°S	.12	1.53	9.86	3.49	24.22	15.46	8.70	3.25	33.36

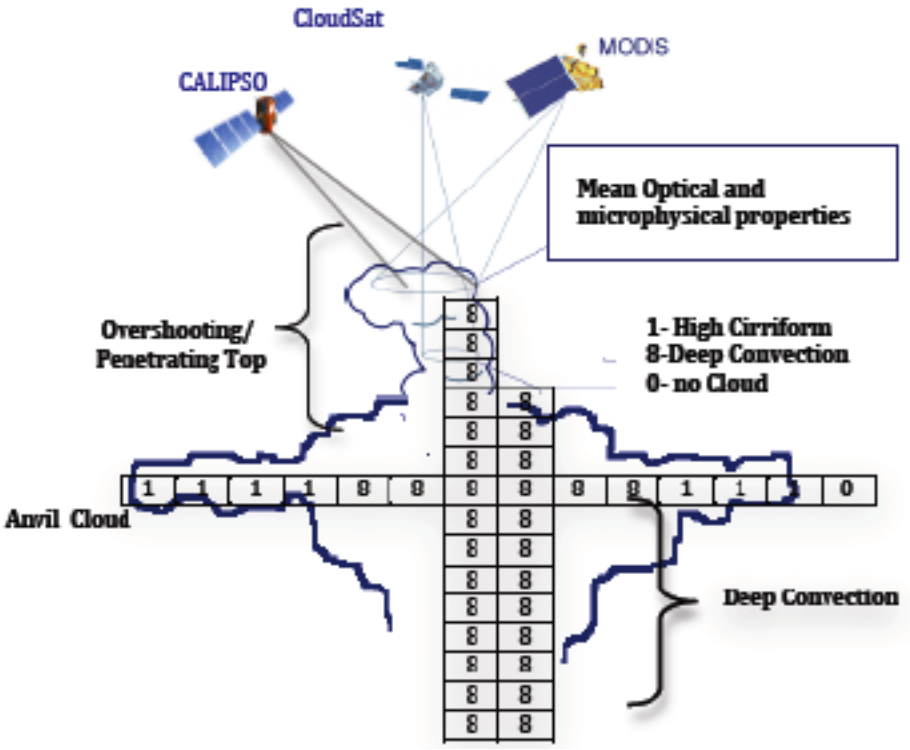

Figure 4.1: To better describe the function of the CloudSat 2B CLDCLASS product, relevant vertical range gates depicting the classification of the anvil cloud, the penetrating top, and the main body of the deep convective cloud are shown. Anvil clouds, which are not classified by the 2B CLDCLASS product are determined when deep convective clouds (8) are present and have high cirriform (cloud class 1) connected to them and no cloud (0 - not shown) beneath them.

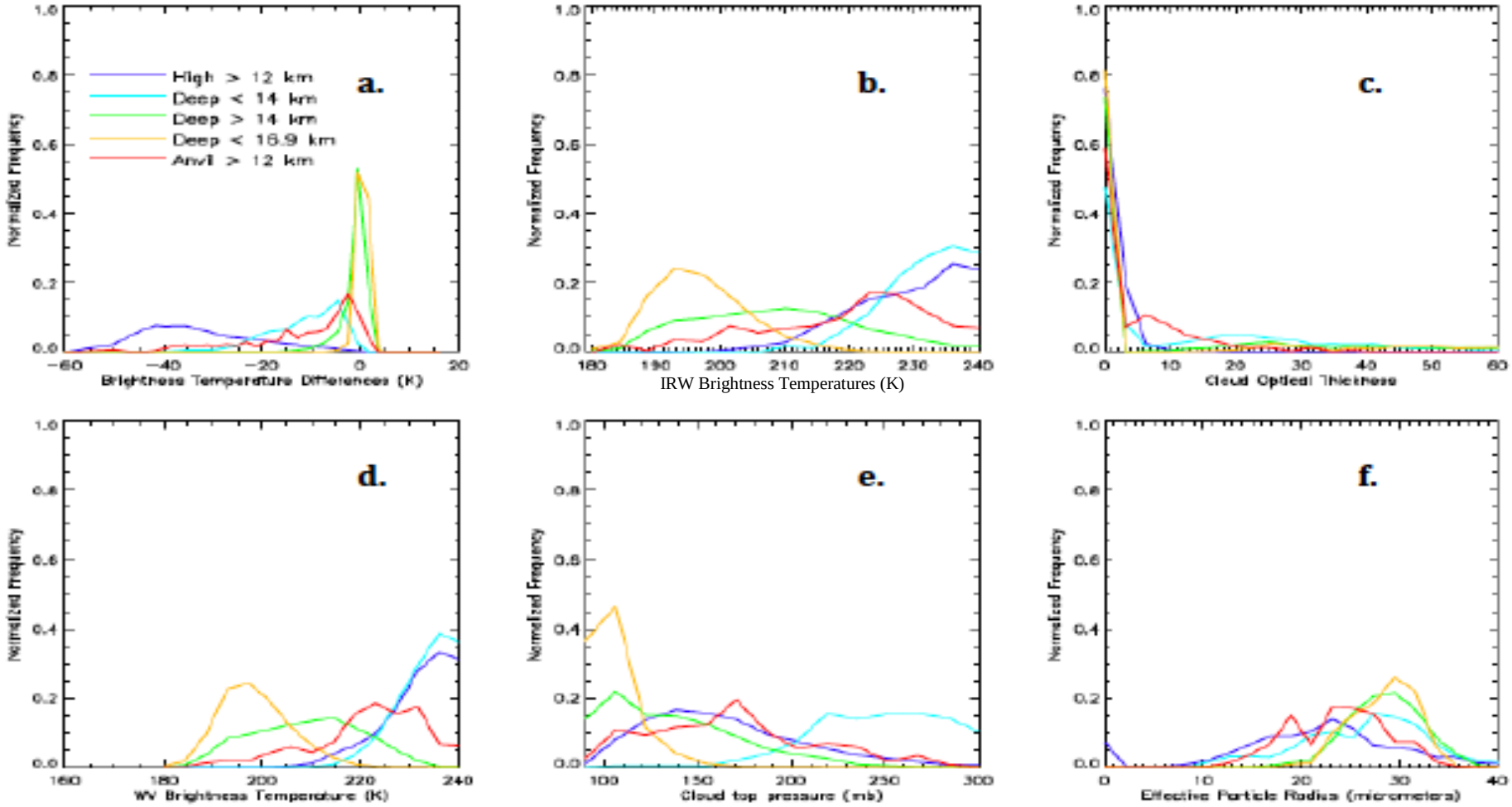

Figure 4.2: Frequency Distributions of a) BTD, b) IRW (cloud) brightness temperature, c) optical thickness, d) WV Brightness Temperature e) cloud top pressure and f) effective particle radius for all the cloud types described in Table 3.2 where the overlap associated with each cloud property is shown for each cloud type.

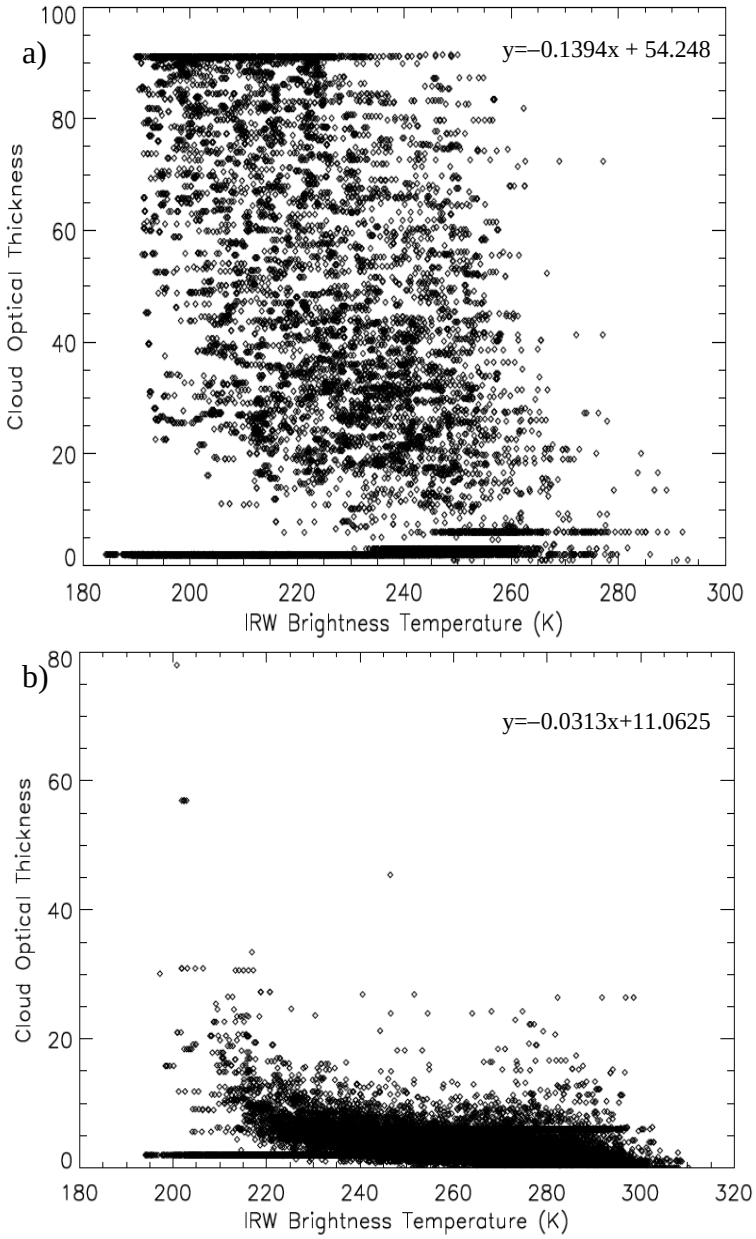

Figure 4.3: Distribution of IRW brightness temperatures verses cloud optical thickness for a) Deep convective clouds and b) cirrus clouds sampled from January 2007 statistics. For both profiles a slightly negative slope of the linear line fit given by the equations a) and b) show that values of brightness temperature generally decrease with increasing cloud optical thickness.

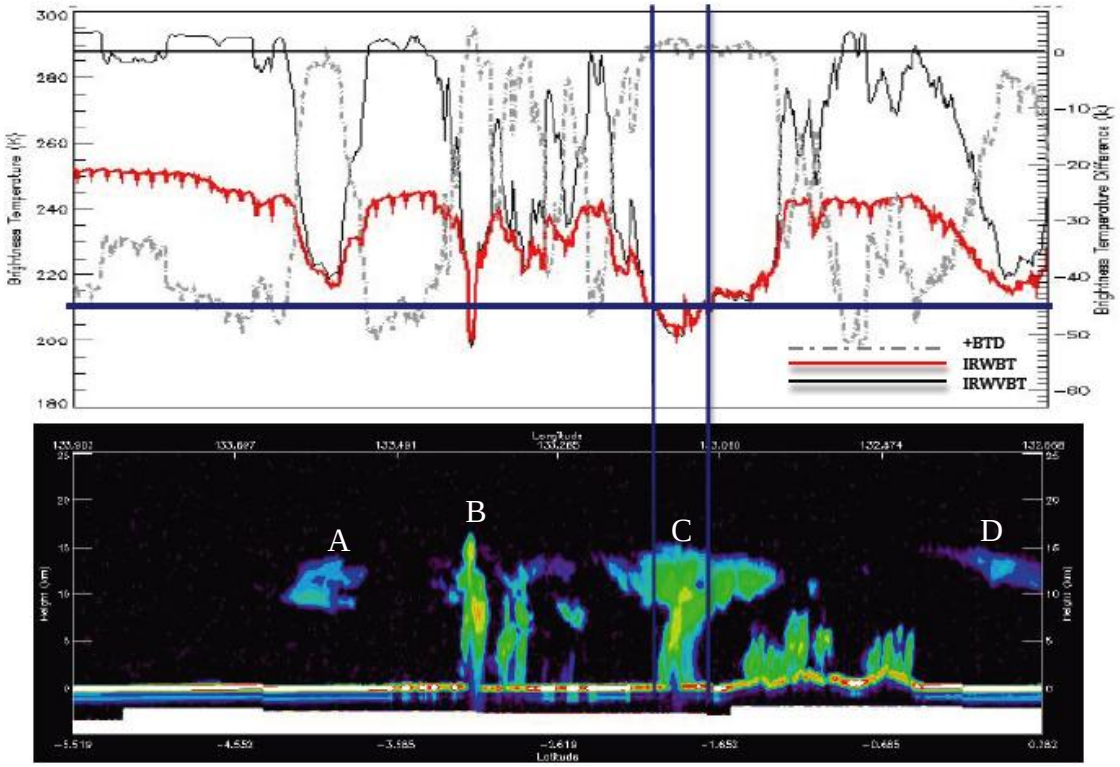

Figure 4.4: CloudSat cross section on October 22, 2006 showing variability of cloud brightness temperatures (IRWBT), IR water vapor brightness temperatures (IRWVBT) and +BTD for stratocumulus cloud (cloud A), overshooting deep convective cloud (cloud B), penetrating deep convective cloud (cloud C), and a cirrus cloud (cloud D).

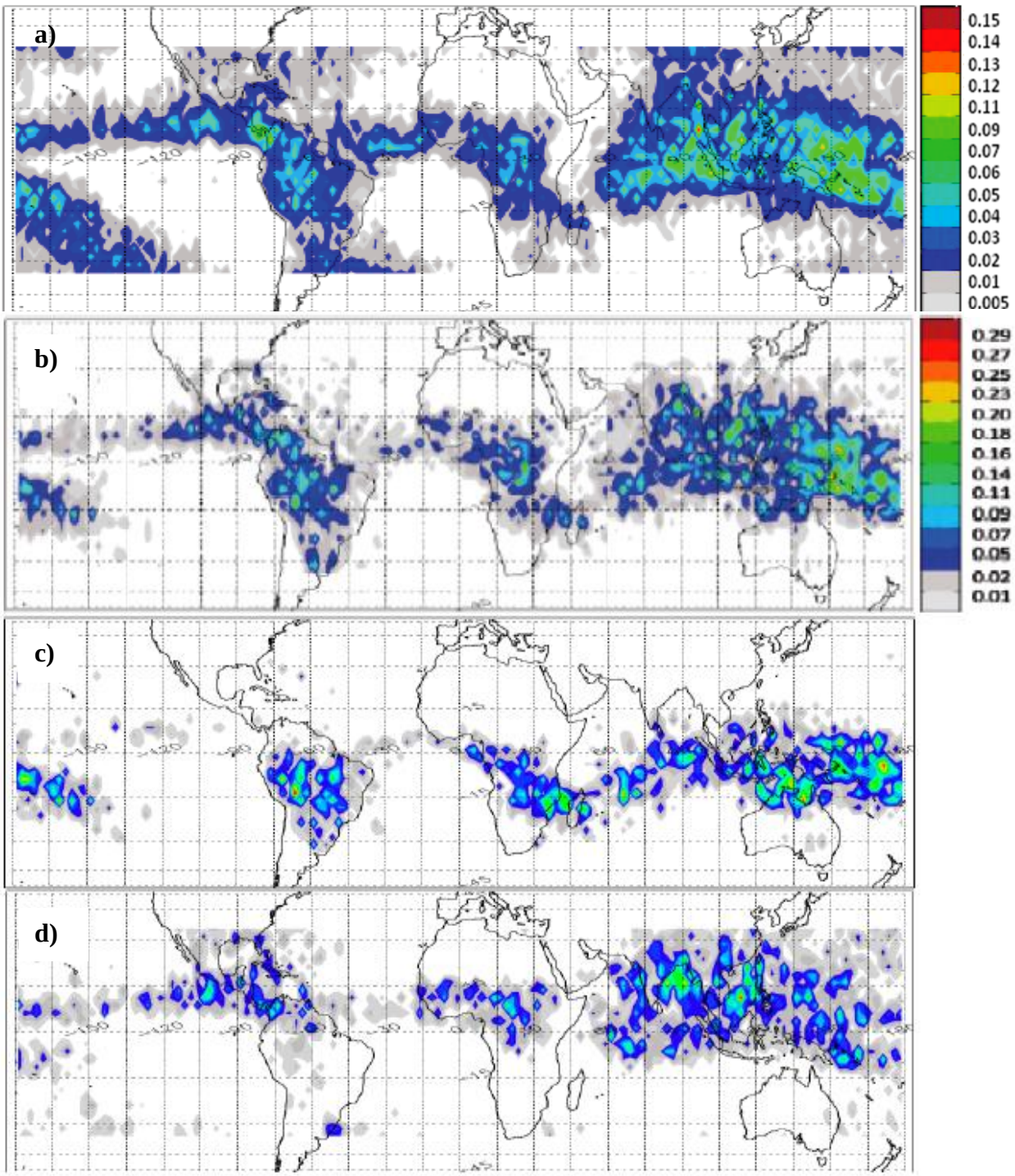

Figure 4.5 Frequency distribution between 35°N–35°S of all cold cloud features a) ≤ 235 K b) ≤ 210 K and seasonal patterns of cold cloud features ≤ 210 K for c) December-February (DJF) and d) June-August (JJA).

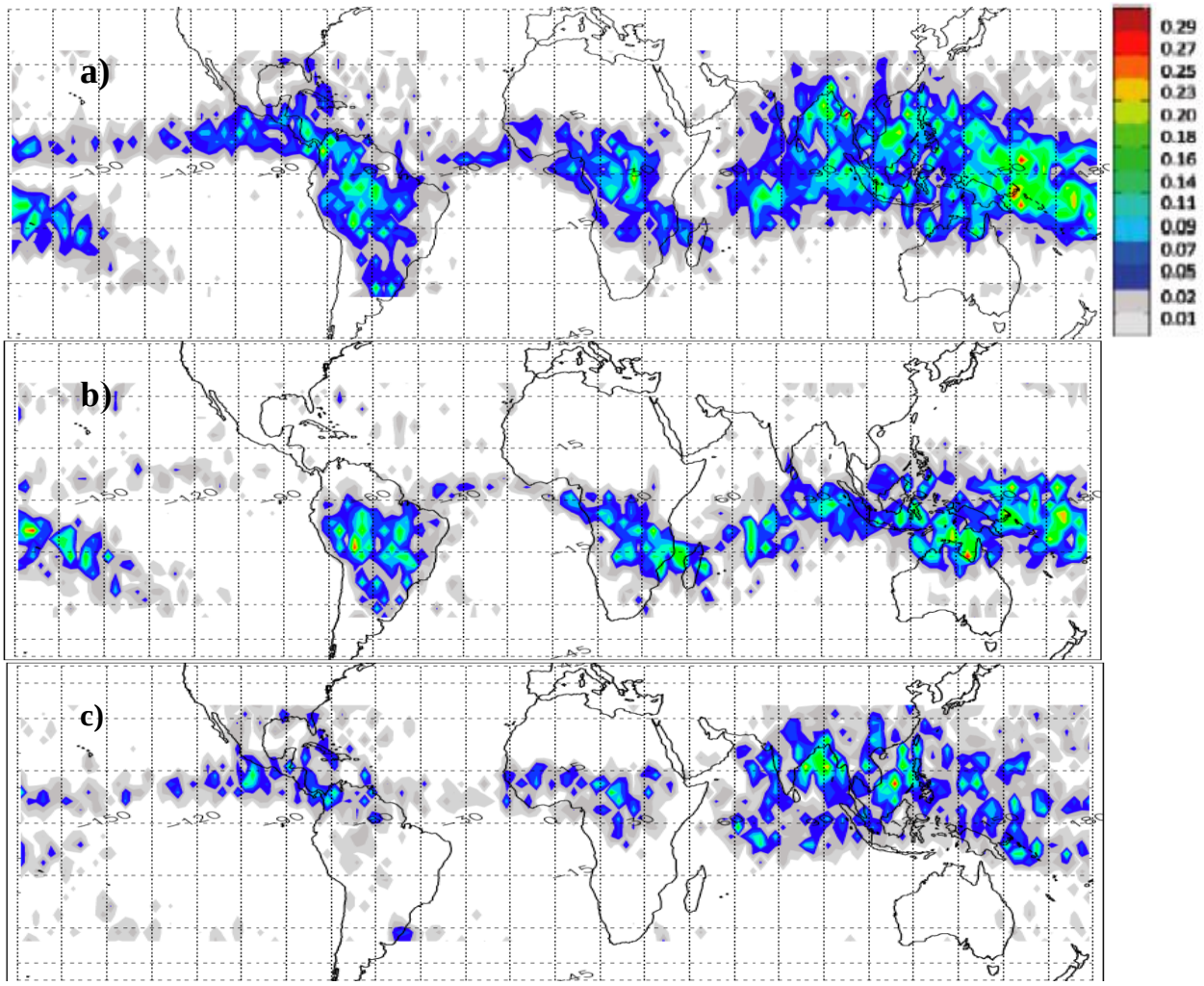

Figure 4.6: Frequency distribution between 35°N─35°S of a) +BTD signatures (with BT_{11} < 235 K) and seasonal patterns of +BTD for b) December-February (DJF) and c) June-August (JJA).

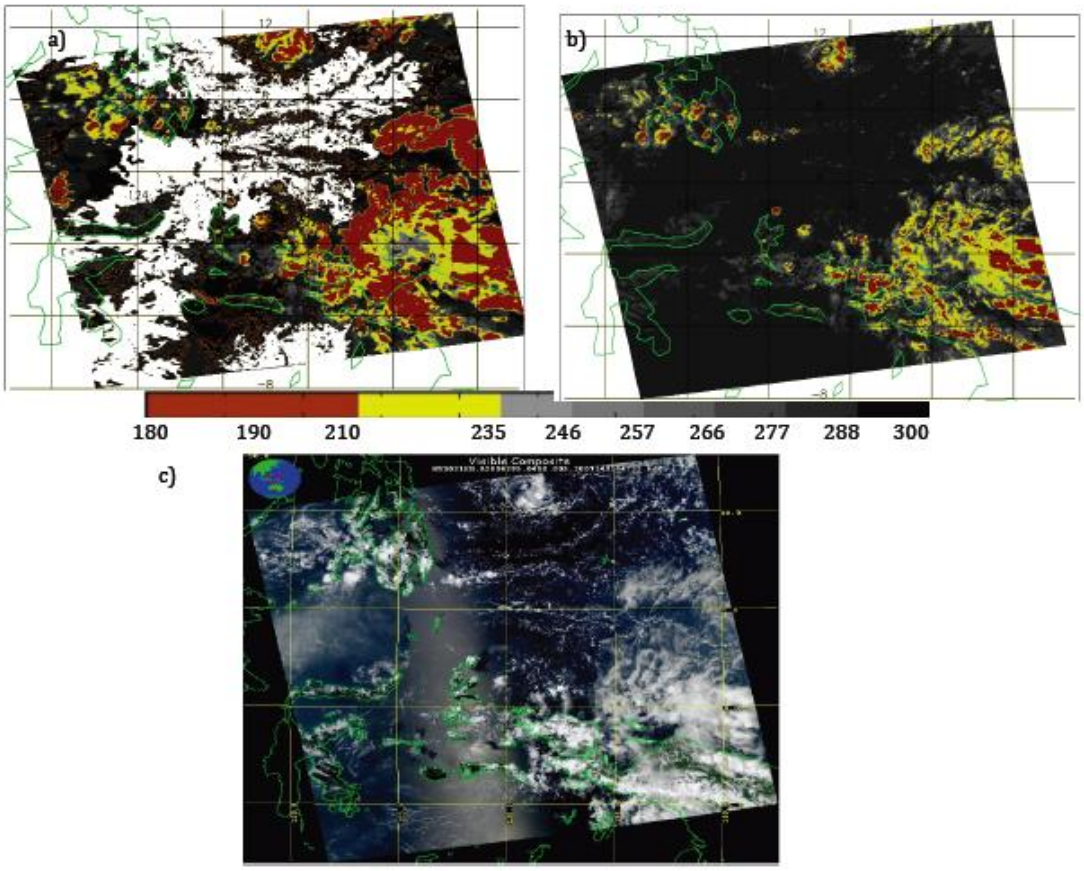

Figure 4.7: Images of a) MODIS L2 Cloud top temperature b) IRW Brightness Temperature and c) visible true color images corresponding to CloudSat granule ID 2575 on October 22, 2006 and time stamp 0450.

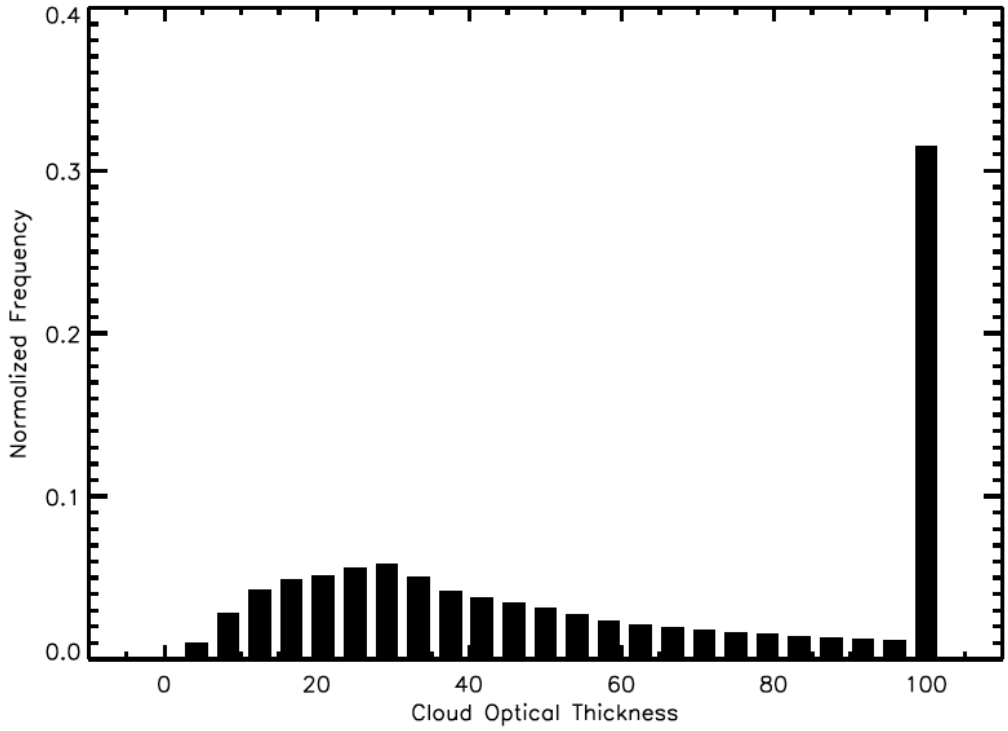

Figure 4.8: Normalized frequency of cloud optical depth for all pixels between 15 N-15 S with BT11 ≤ 210 K for October 2007.

CHAPTER 5

CLIMATOLOGY OF PENETRATING DEEP CONVECTION

5.1 Introduction

The regional and seasonal characteristics of penetrating deep convective clouds have been investigated using radar (e.g., Liu and Zipser., 2005) and IR (e.g., Rossow and Pearl, 2007) observations. The details of those investigations have already been provided in previous chapters. Here we specifically note that according to Rossow and Pearl [2007 penetrating deep convective clouds exhibit five major regions of concentration─ over the maritime continent (east Indian and west Pacific Oceans), in the western end of the South Pacific Convergence Zone and in the eastern end of the Pacific Intertropical Convergence Zone, and over South America and Africa. Rossow and Pearl [2007] note that the distribution of deep convection reaching the TTL does not change when a threshold relative to the tropical cold point tropopause or the base of the TTL, is used. They also report that the seasonal and geographic distribution of penetrating convection is very similar to that provided by Gettelman et al. [2002] and other studies using satellite infrared radiances. They conclude that such similarities indicate that interannual variations in these patterns are not very large.

Tselioudis et al. [2010] performed a time series analysis of tropical penetrating deep convective clouds from July 1983 to June 2008. The authors report that when using ISCCP-D1 data for this period, deep convective clouds penetrating the lower stratosphere show no significant long-term trends. However, the authors also evaluated the time dependent properties of weather state 1 (WS1), which includes the larger mesoscale convective systems but consist largely of considerable amounts of optically thinner, high,

and middle top clouds. It is described by the morphology of relatively high cloud optical thickness (τ) and cloud top pressure (see details as given by Rossow et al., 2005). According to the time series analysis of WS1, Tselioudis et al. conclude that deep convection in the Indian Ocean and the western-central Pacific regions had increases in frequency from 1983 to about 2000 and has remained at a nearly constant level after that. The sharpest increase in deep convection occurred between 1993 and 2000. The authors conclude that stratospheric water vapor trends come from the overall moistening of the tropical upper troposphere rather than from direct transport by convection penetrating into the lower stratosphere.

The ISCCP DX data used by Tselioudis et al. [2010] and Rossow and Pearl [2007] are both produced from the analysis of infrared (IR) and visible (daytime only) radiances from weather satellite images with ~ 5 km horizontal resolution that are sub-sampled to a 30 km horizontal resolution at 3 hr intervals. While it is suggested that the statistics obtained for the ISCCP-DX data set converge to those obtained from the full 5 km dataset, this is only true if the sample population size is large [Seze and Rossow, 1991]. So, for penetrating deep convection that is reportedly representative of ~ 2% of all deep convection and largely characterized by relatively small areal extents (see Chapter 3), it is not clear if the ISCCP DX data, with its coarser resolution, provides reliable results regarding the trends or variability of penetrating deep convective clouds.

Little information is available on the time dependent properties of penetrating deep convective clouds because of the difficulties associated with techniques and the low resolution of the available data. The longest history of observations that may be capable of elucidating the linkages between penetrating deep convection and lower stratospheric

water vapor trends occurring from 1980 to 2008 is associated with conventional passive sensor satellite radiometers analogous to the observations used in the aforementioned studies. However, while ISCCP-DX data is commonly used to deduce global cloud and surface properties, the DX data is not the highest resolution of ISCCP data available. A higher resolution of ISCCP data is available from the GridSat product. This product has been derived from ISCCP B1[1] data and provides global coverage for infrared window (IRWIN) observations dating back to ~ 1980 and infrared water vapor (IRWVP) coverage dating back to 1998. The horizontal and temporal resolution of this data is provided at 10 km every 3 hours. Given these details, GridSat observations are likely to be more useful in analyzing the time dependent properties of penetrating deep convection compared to Rossow and Pearl [2002] and Tselioudis et al. [2010]. More specifically, the GridSat observations will be investigated to determine what (if any) linkages exist between the temporal variability of penetrating deep convective clouds and lower stratospheric water vapor changes. In addition, since radar and IR studies have shown differences in regional maxima of penetrating deep convection and unfortunately coarse temporal sampling of CloudSat observations provided in Chapter 3 do not fully resolve the diurnal cycle, it is still unclear where deep convection reaching the TTL is most dominant.

In Chapter 5 of this thesis, the time dependent properties of penetrating deep convection as obtained from GridSat observations are used to address the following:

[1] International Satellite Cloud Climatology Project (ISCCP) B1 data are geostationary imagery from

1. *How well do positive BTD signatures and cloud brightness temperatures ≤ 210 K from GridSat observe annual, interannual and diurnal variability of penetrating deep convective clouds?*
2. *When resolving the diurnal cycle of penetrating deep convection, where do observations show that overshooting deep convection is most prevalent over the western tropical Pacific or over Africa?*
3. *Do significant trends or patterns of penetrating deep convection exits? If so, how do these trends correspond to changes in lower stratospheric water vapor?*

5.2 Data and Methods

Since July 1983, the International Satellite Cloud Climatology Project (ISCCP) has collected infrared and visible radiances obtained from imaging radiometers carried on the international constellation of weather satellites[2]. By 1998, the constellation enhanced its spectral characteristics with nearly global coverage of upper tropospheric water vapor at ~ 6.7 μm. Observations from ISCCP have primarily been used to better characterize how clouds alter the radiation balance of Earth [Schiffer and Rossow, 1983]. However, ISCCP has also been used to obtain cloud optical and microphysical properties, including cloud fraction, cloud optical depth, cloud type, cloud top pressure and temperature, etc. (for the full list see http://isccp.giss.nasa.gov/cloudtypes.html). ISCCP-B3 data is the primary dataset from which subsequent data products (e.g., pixel level; DX; and gridded

[2] The international constellation of weather satellites includes, EUMETSAT for the Meteorological Satellite (METEOSAT); the Japanese Meteorological Agency (JMA) for the Geostationary Meteorological Satellite (GMS); the Atmospheric Environment Service of Canada for Geostationary Operational Environmental Satellite-East (GOES-East); Colorado State University (CSU) for the GOES-west; and the National Oceanographic and Atmospheric Administration (NOAA) for the polar orbiters.

cloud products C1, C2, D1, and D2) originate. It primarily contains reflected and emitted radiances in regions of the visible (~0.6μm), IR window (~11μm) and IR water vapor (~6.7μm) channels. However, the ISCCP-B3 data is a reduced resolution product that has been subsampled to ~ 30 km due to limitations in computing power that existed in the 1980s. After sampling the radiances to reduce data volume, they are calibrated, navigated, and placed in a common data format (e.g., hdf and netcdf).

In contrast to the ISCCP-B3 data which is calibrated against NOAA-9 Advanced Very High Resolution Radiometer (AVHRR), ISCCP-B1 data has been calibrated using the High Resolution Infrared Radiation Sounder (HIRS) as an independent analysis of the satellite intercalibration performed by (ISCCP) so that biases between ISCCP-B1 observations and HIRS are minimal. These observations are then spatially averaged to ~10 km resolution and nominally referred to as the GridSat product. GridSat provides synoptic observations of reflected and emitted radiances at the same wavelengths as ISCCP-B3 data but at a finer resolution. Although the ISCCP-B1 data extends back to 1978 and the GridSat product is new, these datasets have not been frequently used in research studies. Knapp [2008a] provides more information on the development of ISCCP-B1 data, and Knapp [2008a; 2008b] outlines the potential uses of ISCCP-B1 data for climate studies.

GridSat data is used to evaluate the discernable trends or patterns of variability in the +BTD signature and cold cloud features ≤ 210 K. From the application of techniques described in previous chapters, a climatology of tropical penetrating deep convection is developed for years 1998─2008. As shown by Knapp [2008b], these years correspond to the earliest near global coverage (i.e., not including the poles) of ISCCP B1 observations

in the IR window region centered at ~11μm and the IR water vapor absorption band centered at ~6.7 μm. Moreover, several years (i.e., 1999─2001 and 2007─2008) cover abrupt changes in lower stratospheric water vapor.

Although cold cloud features defined by 3 km x 3 km subsets were used in Chapter 4, GridSat observations are provided at a horizontal resolution of 10 km. To resolve penetrating deep convective cloud tops, no additional averaging is performed. All evaluations made in this chapter of the analysis are based on frequency counts which are evaluated on the basis of 2.5° × 2.5° grids between 35°N to 35° S. For each observation, the frequency per grid is used to evaluate the frequency per region where specific regions (following Tselioudis et al., 2010) include Africa (0°-45°E), the Indian Ocean (45°E-105°E), west Pacific Ocean (105°E-150°E), central Pacific Ocean (150°E-160°W), East Pacific Ocean (160°W-80°W), South America (80°W-45°W), and the Atlantic Ocean (45°W-0°). Standardized monthly anomalies for each region are determined by subtracting the long-term monthly mean from the monthly frequency and dividing by the corresponding monthly standard deviation. By calculating the standardized anomaly, the influences of seasonal changes in the average monthly frequencies are minimized to show the year-to-year variability in the monthly frequencies. This procedure is also repeated for tropical (15°N-15°S) monthly zonal averages of water vapor mixing ratio values at 82.5 mb. Prior to mid-2004 this dataset is based on observations from the Upper Air Research Satellite Halogen Occultation Experiment (UARS HALOE) but has been shifted to match the Aura Microwave Limb Sounder (MLS). Observations of 82mb mixing ratios post-mid-2004 are based on Aura MLS. Similar measurements have been documented by Rosenlof and Reid [2008], Solomon et al., [2010], and Ray and Rosenlof

[2007] with further documentation of Aura MLS data given by Waters et al. [2006] and further documentation on UARS HALOE observations given by Russell et al. [1993].

5.3 Results

5.3.1 Evaluation of Climatological Data

GridSat is a relatively new dataset. While rigorous calibration testing of the IRWIN channel has motivated its use in several other studies (e.g., Bain et al., 2010; Kossin et al., 2007), the calibration of both the IRWIN and IRWVP channels at low cloud brightness temperatures (i.e., ≤ 210K) is questionable due to the limited number of calibration matchups provided by NOAA HIRS. Since the general characteristics of deep convection are well documented, it is important to test that observations from GridSat provide the same general characteristics of deep convection provided in other studies.

To evaluate the signature of penetrating deep convection from +BTD signatures and cloud brightness temperatures ≤ 210 K, their annual frequency distributions are provided for years 1998─2008 in Figures 5.1 and 5.2, respectively. Comparison of the observations show that maxima in +BTD signatures most often occur over central Africa and in the Indian Ocean just west of Indonesia. In comparison, cloud brightness temperatures ≤ 210 K have maxima over Africa, the central Pacific, and west Pacific. Evaluation of all +BTD annuals provided in Figure 5.1 show expected patterns in occurrence frequencies from 1998–2001 and 2008 while annual frequency distributions for 2002─2007 show a lack of positive BTD signatures over Indonesia and the western tropical Pacific Ocean. In comparison, cloud brightness temperatures ≤ 210 K show annual distributions with expected patterns in occurrence frequencies for all years between 1998 and 2008. While there is some interannual variability in regions of

maximum frequencies within the western tropical Pacific and central Pacific, it is not clear if this variability has a strong correlation with La Niña (1999, 2000 and 2008) and El Niño (1998, 2002, 2004, and 2006) years, which could potentially shift maxima in penetrating deep convection from the western Pacific to the central Pacific.

Since both +BTD signatures and cloud brightness temperatures ≤ 210 K should have similar patterns, the 2002─2007 BTD annuals reveal inconsistencies that are specifically due to the IRWVP channel and thus dataset driven. While the exact source of the problem is not clear, the 2002─2007 distributions of +BTD signatures are most deficient in regions that correspond to GOES-W. Given these results, the remaining sections of Chapter 5 will not focus on +BTD signatures. Instead, penetrating deep convection will be evaluated from cloud brightness temperatures ≤ 210 K, which appear to be consistent with the general distribution of penetrating deep convection provided in other studies.

To further evaluate observations of penetrating deep convective clouds, cloud brightness temperatures ≤ 210 K are also compared with Russo et al. [2010], who used observations of cloud top height, upper tropospheric/lower stratospheric water vapor, and surface precipitation estimates to evaluate the performance of nine different models to represent penetrating deep convection. Among the results presented by Russo et al. we specifically focus on the evaluation of monthly mean cloud top height in the maritime continent (15°N-15°S and 90°E-150°E). These results utilize observations of cloud top height from ISCCP (-D1), MODIS Terra and Aqua for November 2005. These observations are provided in Figure 5.3(a-c) and compared with the GridSat observations of brightness temperatures ≤ 210 K for the same region and period in Figure 5.3(d). The

results of Figures 5.3(a-c) qualitatively show that the ISCCP-D1 data is less capable of representing cloud top structure compared with both MODIS Aqua and Terra satellites in terms of regional structure and vertical extent. ISCCP-D1 observations show that for November 2005, the region does not have cloud top heights > 9 km. On the other hand, MODIS Aqua and Terra observations show heights up to 12 km. Obviously MODIS Aqua and Terra monthly mean cloud top structures do not show penetrating deep convection since these events are rather rare. Thus it is not expected that pronounced features suggestive of penetrating deep convective cloud tops would be found within the monthly mean. Although there are differences in the spatial and temporal sampling of MODIS (Terra and Aqua) and GridSat, in general, they have good agreement. Although the observations provided in Figures 5.3(a-c) do not show the time-averaged frequency of deep convective clouds reaching the TTL, these results do show that the most frequent observations of cloud brightness temperatures ≤ 210 K occur in regions that are associated with higher cloud top heights.

The most fundamental modes of variability of the global climate system are the diurnal and seasonal cycles. The seasonal cycle of penetrating deep convective clouds has been addressed in Chapter 3 (Figure 3.3) and Chapter 4 (Figure 4.5 and 4.6) for Northern Hemisphere winter (DJF) and summer (JJA). GridSat observations of cloud brightness temperatures ≤ 210 K for the same periods are in good agreement with the seasonal distributions that have already been provided. On the other hand, coarse temporal sampling associated with the Aqua orbit did not enable the full diurnal cycle of deep convection to be evaluated from CloudSat and MODIS-AUX observations. In addition, it was unclear how a full sampling of the complete diurnal cycle would impact the

CloudSat distribution, which showed that the highest frequencies of penetrating deep convection were centered over the Indian Ocean and western tropical Pacific. The diurnal cycle is therefore evaluated for Africa, the Indian Ocean, South America, and the western Pacific Ocean in order to compare the variability of penetrating deep convective clouds over tropical land regions and the tropical oceans.

As shown in Figure 5.4, the land regions of Africa and South America have a pronounced diurnal cycle that peaks in the late afternoon to early evening while only a slight diurnal cycle exists over the Indian and western tropical Pacific Oceans, of which the later also shows peak frequencies during the early morning. These results are consistent with other studies (e.g., Soden, 2000; Yang and Slingo; 2000) and indicate that temporal sampling may have an impact on the regional analysis of penetrating deep convection, especially over land. They also support the interpretation that the $BT_{11} \leq 210$ K distribution is dominated by deep convective clouds verses other types of high clouds since deep convective clouds are considerably forced by daytime solar heating. Although cirrus anvil clouds can make up a third of the $BT_{11} \leq 210$ K distribution cirrus clouds have longer lifetimes than deep convection. Thus it is still, unclear whether poorly resolved temporal sampling may have a strong impact on the regional dominance of deep convection. To make this evaluation, the regional dominance of deep convection is evaluated for all regions in Figure 5.5.

According to the monthly normalized frequencies of all cloud brightness temperatures ≤ 210 K occurring within each of the seven regions described in Section 5.2 the largest frequencies of the $BT_{11} \leq 210$ K signal occurs of the western-central Pacific and Indian Oceans. The quantitative estimates of the contribution each region makes to

the total tropical signal is provided in Table 5.1 with linear regression statistics that identify the strength and significance of each region when evaluated against the tropical signal. The highest frequencies of penetrating deep convective clouds are consistently over the western Pacific, central Pacific and Indian Oceans accounting for 24.2%, 18.3%, and 17.5% respectively. Following these regions are Africa (14.9%) and South America (11.0%) and lastly the eastern Pacific (8.9%) and Atlantic Oceans (5.3%), which in Figure 5.5 show very strong seasonality compared with the western Pacific, central Pacific and Indian Oceans where frequencies are the highest. Regional analysis according to linear regression statistics where the autocorrelation[3] of the noise ($\hat{\phi}$) and standard deviation of the noise ($\hat{\sigma}_N$) have been considered as in the approach of Weatherhead et al. [1998] is provided in Table 5.2. According to this information, slightly negative trends occur in the tropics and most other regions between 1998─2008, with the exception of Africa, the central Pacific, and the Atlantic Ocean. However, these trends are not significant at the 95% confidence level and would require much more data to meet this criteria. The trends are represented in Figure 5.6 for the tropics and individual regions. Considering the dominance of the western-central Pacific and Indian Ocean and the significance of their relationships to the tropical signal at the 95% confidence level, a closer evaluation of these particular regions is made in the following section to evaluate anomalies in monthly water vapor mixing ratios at 82 mb.

5.3.2 Penetrating Deep Convection and Lower Stratospheric Water Vapor

As stated in Section 1.1 lower stratospheric water vapor mixing ratios are largely

[3] Autocorrelation is the cross-correlation of a signal with itself. When the noise within a time series is said to be autocorrelated, the time series violates the assumption of independence of errors. Autocorrelation of the noise $\hat{\phi}$ and a large standard deviation of the noise $\hat{\sigma}_N$ make any trend within a time series more difficult to detect.

controlled by the seasonal variation in zonal mean tropical tropopause temperature. According to Highwood and Hoskins [1998], the average JJA zonal mean in tropical tropopause temperature is ~ 6°C warmer than the DJF zonal mean. Since tropical tropopause temperatures impact water vapor mixing ratios in accordance with the Clausius-Clapeyron relation, the seasonal cycle is the most dominant feature of the 1998-2008 time series of lower stratospheric water vapor at 82 mb provided in Figure 5.7. Based on this seasonal variation, water vapor mixing ratios at 82 mb range from about 2 ppmv in DJF to about 5.5 ppmv in JJA. The monthly anomalies in 82 mb water vapor mixing ratios in Figure 5.8 is associated with decreasing trend of -0.1178 ppmv/month but would take ~ 15 years to be significant at the 95% confidence level.

Monthly frequency anomalies of cloud brightness temperatures ≤ 210 K were evaluated with monthly anomalies in the water vapor mixing ratios at 82 mb according to linear regression analysis for the entire tropics, western Pacific, central Pacific, and Indian Oceans. For this analysis, it is important to note that the Brewer-Dobson circulation, which lifts air through the tropopause and into the lower stratosphere is quite slow, progressing at a speed of ~20-30 m/day. Since this is an important dynamical factor modulating transport from the TTL into the lower stratosphere (e.g., Mote et al., 1995), anomalies in water vapor mixing ratio at 82 mb (~17.5 km) and $BT_{11} \leq 210$ K signals representative of penetrating deep convection with cloud top heights at ~ 15.2 (±0.91 km) km (~110 mb) were evaluated at lags of 0 to 6 months. Linear regression statistics for these evaluations are provided in Table 5.3 and show consistent downward trends for the tropics, western Pacific, and central Pacific Oceans while trends in the Indian Ocean are more positive.

For each region evaluated, the strongest and most significant relationships were most consistently observed for lags between 2 – 3 months. At a lag of 3 months, the combined western-central Pacific had a significant anticorrelation where the largest amount of variance explained by the combined western-central Pacific monthly frequency anomalies is 8.25%. This result indicates that among all regions considered and to the extent that the coldest penetrating deep convection can be determined from the GridSat record, events within the western-central Pacific dominate the anomalies in the tropical 82 mb water vapor record. The time lag associated with this result does not drastically differ from Randel et al. [2004] who evaluated 82 mb H_2O anomalies against 10°N-10°S tropopause temperature anomalies and reported the highest correlations at a lag of 2 months. However, the meaning of the anticorrelated relationship must also be considered.

Solomon and Reid [2008] evaluated trends in the temperature and water vapor content of the tropical lower stratosphere and its connection with sea surface temperatures (SST) in the western-central Pacific. They observed a significant anticorrelation with SST anomalies that explained ~2% of the variance at lag zero in the lower stratospheric temperatures for an analysis period of 34 years (1960-1994). In their evaluation, the authors note that the major response to the variance in lower stratospheric temperatures is the quasibiennial oscillation (QBO) in the tropical stratospheric winds and suggests that the QBO signal makes it rather difficult to detect the variance within the signal that is due to other components. The data also suggests that the 1998-2008 decreasing trend in the monthly frequency of penetrating tops, which explains about 8.25% of the variance in the 82 mb water vapor anomalies, may be influencing the

decreasing trend in the 82 mb water vapor values. Removing the portion of the 82 mb water vapor anomalies that is due to the QBO may however prove to establish a more direct relationship determined by stronger correlations and a higher percentage of explained variance.

In comparison to Tselioudis et al. [2010], who have shown the convective variability of the WS1 series representing organized mesoscale convection and the presence of considerable amounts of optically thinner, high and middle top clouds, it is not clear to what extent the WS1 series represents deep convection and more importantly, there is no corresponding evaluation of changes in convective variability with changes in lower stratospheric water vapor changes. Hence, it is unclear if similar, stronger, or weaker correlations exist when we analyze changes in lower stratospheric water vapor variability against all deep convection, which Tselioudis et al. suggest is a more likely mechanism driving stratospheric water vapor variability patterns.

5.4 Summary and Discussion

Results given in Chapter 5 show that although +BTD signatures from GridSat could not be used for further analysis of penetrating cloud tops because of issues with GridSat $BT_{6.7}$ observations, cold cloud features ≤ 210 K are a useful method to infer penetrating deep convective cloud activity. GridSat observations are at higher resolution than ISCCP-D1 observations, which have been used in most of the recent studies addressing the climatology of penetrating deep convective clouds. As indicated by the comparison of ISCCP-D1 and Aqua and Terra MODIS observations of cloud top structure, ISCCP-D1 data are less capable of resolving vertical cloud top structure. On the other hand, GridSat observations of cloud brightness temperatures ≤ 210 K show

similar structure as provided by MODIS Terra and Aqua. The limitations of ISCCP (D1) observations to more accurately resolve cloud top height is an obstacle for any studies seeking to use the ISCCP (D1) observations to evaluate penetrating deep convection. In the remaining sections of this discussion, the results of this study are evaluated to elaborate on the climatological characteristics of penetrating deep convective clouds and to specifically address the questions in Section 5.1.

How well do +BTD signatures and cloud brightness temperatures ≤ 210 K from GridSat observe annual, interannual, and diurnal variability of penetrating deep convective clouds? Cloud brightness temperatures ≤ 210 K are used to infer the variability of penetrating deep convective clouds. In general GridSat observations agree with both the diurnal and annual characteristics of the $BT_{11} \leq 210$ K signal evaluated in earlier IR studies. While there is interannual variability especially in the western tropical Pacific and central Pacific, it is not clear if this variability has a strong correlation with La Niña (1999, 2000 and 2008) and El Niño (1998, 2002, 2004, and 2006) years since there is no direct link to shifts in maxima frequencies from the western Pacific to the central Pacific for El Niño and events. Gettelman et al. [2002] addressed this linkage in his evaluation of penetrating deep convection from 3.5 years (from October 1986 to February 1989 and October 1991 to September 1992) of global cloud imagery but the authors did not resolve a direct linkage between the variability in El Niño and the interannual variability in penetrating deep convective cloud frequency. However, we suggests that when considering the variability of penetrating deep convection, it may be more likely that the La Niña and El Niño phase is not as important as the variability of strong events vs. weak events. This is an interesting point for future research.

When resolving the diurnal cycle of penetrating deep convection do observations show that overshooting deep convection is most prevalent over the western tropical Pacific or over Africa? This question is particularly important since several hypothesis have been used to determine where deep convective clouds penetrate into the lower stratosphere. The first hypothesis proposed by Newell and Gould─Stewart [1981] suggests that troposphere-stratosphere transport occurs over the Maritime Continent and western Pacific described as the "Stratospheric Fountain" via rather strong deep convection. With the advent of space-borne radars, Liu and Zipser [2005; 2007] argue that upper tropospheric and lower stratospheric water vapor exchange is primarily driven by deep convection over Africa. Although the original Stratospheric Fountain hypothesis suggests that air only enters the tropical tropopause in the western tropical Pacific, northern Australia, Indonesia and Malaysia between November-March, we presently know that water vapor may enter the lower stratosphere during any time of the year, and while it predominantly enters within the tropics, it also has a tendency to enter the lower stratosphere from extratropical regions via penetrating deep convection (Chapter 4) and tropopause folding[4] [Holton et al., 1995]. However, in support of the stratospheric fountain hypothesis the results shown in Figure 5.5 suggests that the western tropical Pacific has the highest occurrence frequencies of penetrating deep convective clouds supporting the results of the CloudSat distribution in Figures 3.3 and 3.4 and the results

[4] Tropopause folding is a source of midlatitude stratospheric-tropospheric exchange. It occurs in areas with large vertical shear and strong meridional thermal gradients. Downward transport of stratospheric air into the troposphere occurs along the sloping lines of constant potential temperature.

of Russo et al., [2010] who modeled the impact of deep convection on the tropical tropopause layer.

Given that +BTD signatures and cloud brightness temperatures ≤ 210 K sufficiently represent penetrating deep convection, do discernable trends or patterns of variability exists? If so, how do these trends correspond to changes in lower stratospheric water vapor? According to studies investigating the temporal variability of lower stratospheric water vapor, a positive trend totaling ~ 1 ppmv occurred between 1980─2000 (e.g., Oltmans et al., 2000; Solomon et al., 2001; Rosenlof et al., 2010). Post 2000 trends show a decrease totaling ~ 0.4 ppmv (e.g., Solomon et al., 2010). Although much interannual variability is shown throughout the tropics, negative trends in lower stratospheric water vapor at 82 mb are consistent with trends in the monthly frequency anomalies evaluated for the entire tropics and the western-central Pacific and Indian Oceans which dominates the tropical record. The explained variance provided in Table 5.3, shows that at a lag of 3 months, $BT_{11} \leq 210$ K time series of the western-central Pacific explains ~8.25% of the variance of anomalies in the 82 mb water vapor time series. Since anticorrelations suggest that increases in the frequency of penetrating deep convection decreases water vapor at 82 mb it is possible that penetrating deep convective clouds are dehydrating the lower stratosphere. However, few observations support this conclusion and both observational records show decreasing trends. Thus it is actually more justifiable to conclude that the overall impact of penetrating deep convective clouds is to hydrate the lower stratosphere; whereby fewer amounts of penetrating deep convection tend to decreases water vapor at 82 mb and larger amounts of penetrating deep convection tends to increase water vapor at 82 mb.

For these results, we acknowledge that several levels of uncertainty. For example, while we have concluded that the $BT_{11} \leq 210$ K signal is dominated by penetrating tops, it is not composed solely of penetrating tops. Furthermore, the 82 mb water vapor data is provided as monthly averages over an entire latitudinal band (15°N-15°S). It is possible that monthly means for such a wide latitudinal range may obscure some relevant information related to the influence of penetrating deep convective tops. Finally, while the QBO signal is more dominant away from the tropical tropopause rather than at the tropical tropopause, there is still some modulation of tropical tropopause temperatures and water vapor mixing ratio due to the QBO and its variability. Minimizing this influence is important to better resolve the relationship between penetrating deep convection and lower stratospheric water vapor.

Although Chapter 5 has investigated the climatology of the $BT_{11} \leq 210$K distribution from 1998-2008, other results for years prior to 1998 should also be analyzed to give a better indication of the relationship between penetrating deep convective active within the tropics and lower stratospheric water vapor variability. The comparison of this data with upper tropospheric/lower stratospheric water vapor variability should also be performed at ~ 15.5 km (~110 mb) and up to ~ 17.5 km (82 mb). A longer time series analysis at multiple levels may provide more evidence regarding the connection between lower stratospheric water vapor and penetrating deep convective clouds. It is possible that penetrating deep convective clouds have a stronger impact on lower stratospheric water vapor than these observations lead us to conclude. However, the key to better unlocking this relationship may not be obtained according to the shear frequency but some other conditions of penetrating tops such as areal extent and duration.

Table 5.1: Linear regression statistics for tropical and regional standardized frequency anomalies in monthly IRWBT ≤ 210 K where the slope/trend is equivalent to the correlation coefficient, p-value and t-stat are both standards for identifying the significance of the tropical and regional relationships and are compared to α=0.05 and a critical t-value of ±1.962.

Tropics w/	% Tropics	y-int (10^{-6})	Slope/trend	p-value	t-stat for significance of slope	Variance Explained (%)
W. Pacific	24.15	-4.110	0.425	<.001	5.348	18.032
C. Pacific	18.28	-3.305	0.213	0.014	2.480	4.516
E. Pacific	8.89	-3.752	-0.047	0.594	-0.534	0.219
Indian	17.52	-2.840	0.313	<.001	3.757	9.794
Atlantic	5.31	-3.126	0.291	0.001	3.469	8.471
S. America	10.98	-3.700	0.121	0.167	1.389	1.462
Africa	14.86	-4.029	0.159	0.069	1.834	2.523

Table 5.2: Time series regression statistics for standardized frequency anomalies in monthly IRWBT ≤ 210 K with number of years ($\hat{n}$*) of monthly data needed to detect the trend provided for each region at the 95% confidence level as a function of the autocorrelation ($\hat{\phi}_N$ **)** and standard deviation ($\hat{\sigma}_N$ **)** of the noise (Weatherhead et al., 1998).

	y-int	slope/trend	$\hat{\phi}_N$	$\hat{\sigma}_N$	$\hat{n}$*
Tropics	0.390	-0.072	0.203	0.031	14.020
W. Pacific Ocean	0.317	-0.058	0.373	0.037	18.149
C. Pacific Ocean	-0.234	0.043	0.573	0.050	26.928
E. Pacific Ocean	0.437	-0.080	0.430	0.039	15.035
Indian Ocean	0.100	-0.018	-0.105	0.023	28.694
Atlantic Ocean	-0.262	0.048	0.272	0.034	19.511
S. America	0.047	-0.009	0.082	0.028	53.715
Africa	-0.109	0.020	0.176	0.031	32.945

Table 5.3: Linear regression statistics for anomalies in monthly frequency of IRWBT ≤ 210 K and monthly anomalies in 82 mb water vapor mixing ratio at lags of 0 to 6 months for the tropics, western Pacific, central Pacific and Indian Oceans. Again, the p-value and t-stat is respectively compared to α=0.05 and a critical t-value of ±1.962.

Lag in 82 mb SWV	y-int	slope/trend	p-value	t-stat for significance of slope	Variance Explained (%)
			Tropics		
0	0.000	-0.074	0.400	-0.844	0.548
1	-0.003	-0.133	0.132	-1.516	1.742
2	-0.020	-0.143	0.100	-1.656	2.103
3	-0.031	-0.072	0.410	-0.826	0.533
4	-0.045	-0.107	0.211	-1.256	1.232
5	-0.057	-0.052	0.544	-0.608	0.292
6	-0.072	-0.048	0.572	-0.567	0.260
			western Pacific		
0	0.000	0.035	0.690	0.400	0.123
1	-0.011	-0.111	0.206	-1.270	1.232
2	-0.021	-0.129	0.138	-1.492	1.716
3	-0.032	-0.192	0.026	-2.251	3.842
4	-0.049	-0.188	0.029	-2.214	3.725
5	-0.059	-0.144	0.093	-1.690	2.220
6	-0.073	-0.163	0.055	-1.933	2.924
			central Pacific		
0	0.000	-0.244	0.005	-2.864	5.954
1	-0.008	-0.240	0.006	-2.815	5.905
2	-0.016	-0.233	0.007	-2.721	5.476
3	-0.025	-0.209	0.017	-2.426	4.410
4	-0.040	-0.175	0.044	-2.033	3.168
5	-0.054	-0.083	0.340	-0.958	0.723
6	-0.068	-0.091	0.292	-1.058	0.903
			Indian Ocean		
0	0.000	0.044	0.617	0.501	0.193
1	-0.001	0.054	0.536	0.621	0.298
2	-0.020	0.016	0.857	0.180	0.020
3	-0.029	0.079	0.372	0.896	0.628
4	-0.046	-0.013	0.887	-0.143	0.016
5	-0.058	-0.124	0.153	-1.439	1.632
6	-0.074	-0.098	0.258	-1.138	1.032

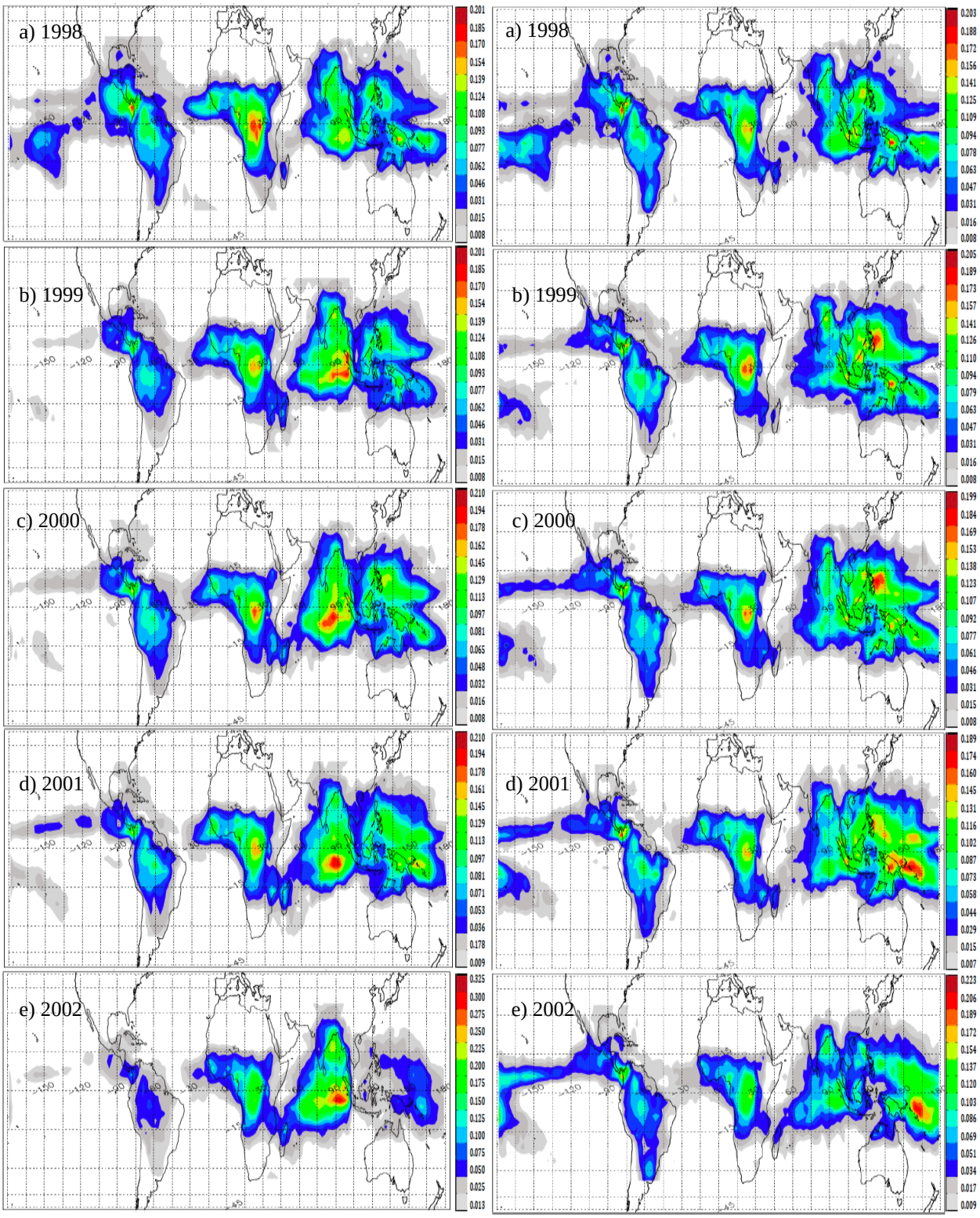

Figure 5.1: GridSat 2.5° x 2.5° annual frequency distributions of annual +BTD for years 1998-2002 and over 35°N - 35°S.

Figure 5.2: Same as Figure 5.2 except for cloud brightness temperatures ≤ 210 K for years 1998-2002 and over 35°N - 35°S.

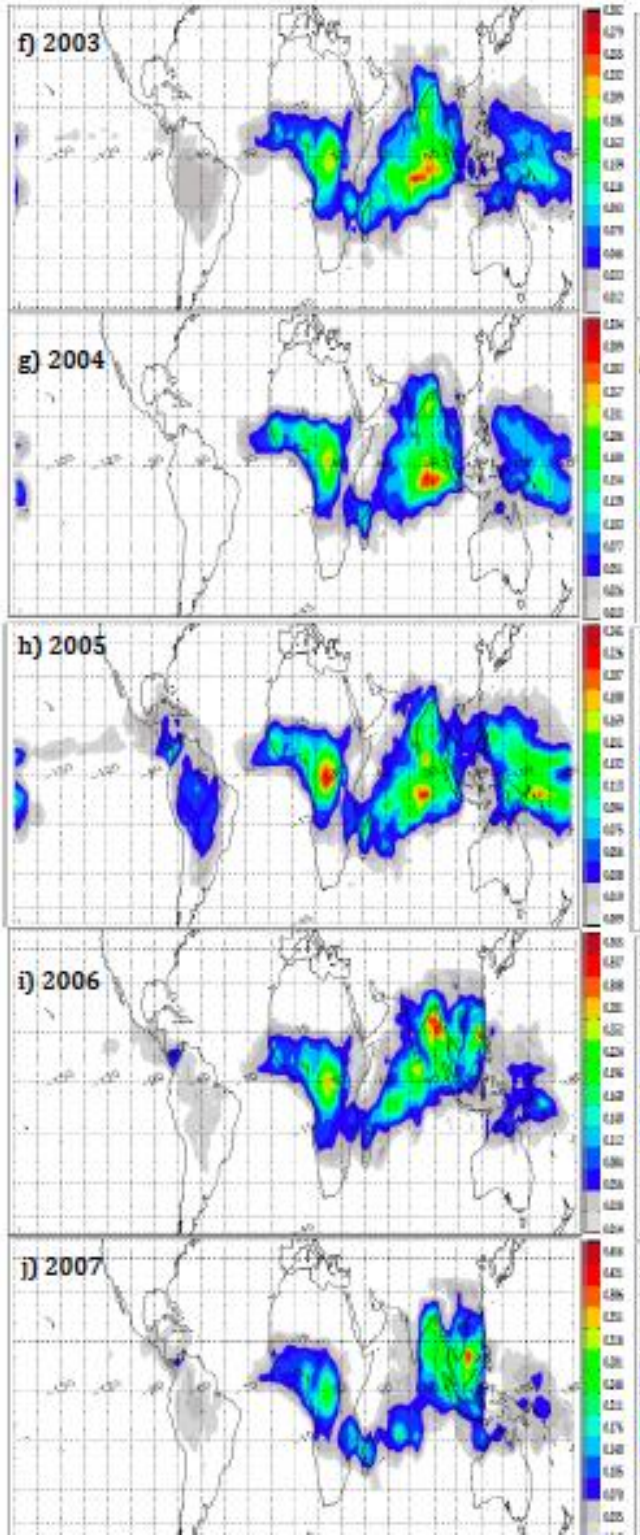

Figure 5.1: (cont.) for years 2003-2007.

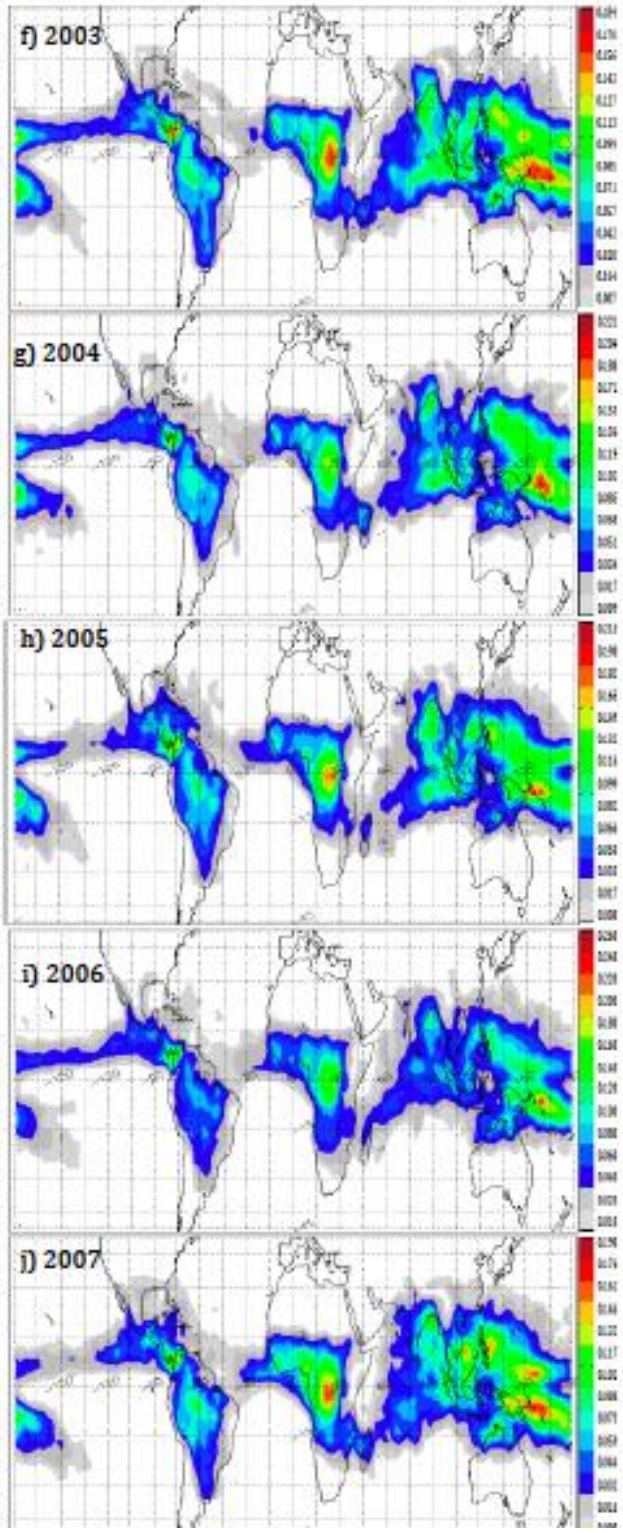

Figure 5.2: (cont.) for years 2003-2007.

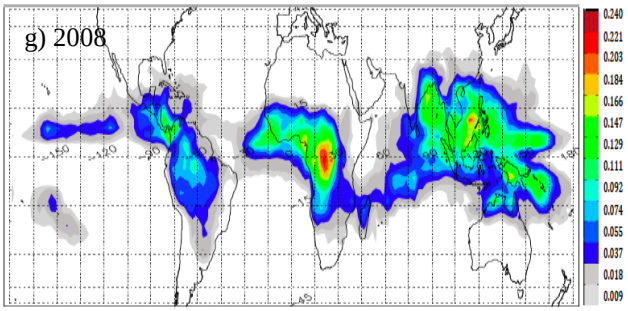

Figure 5.1: (cont.) for 2008.

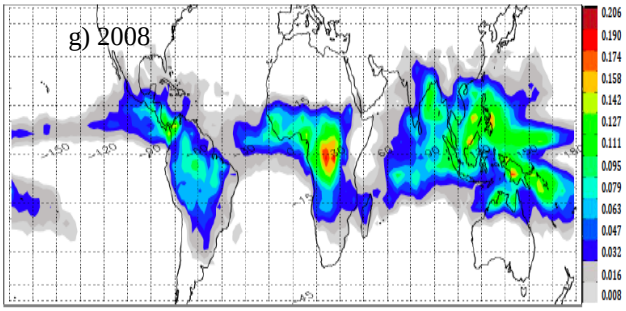

Figure 5.2: (cont.) for 2008.

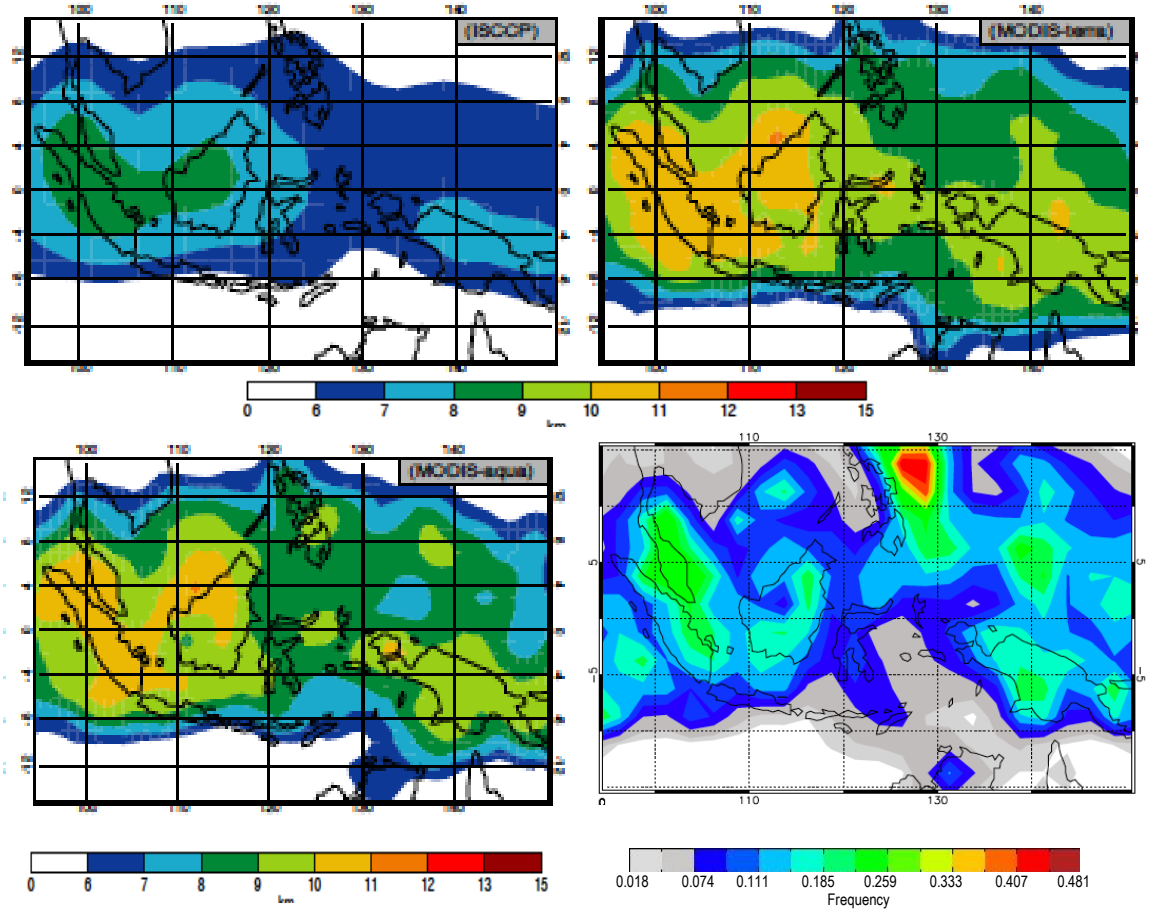

Figure 5.3: November 2005 observations for the Maritime continent (15N-15S, 90E-150E) of cloud top height from a) ISSCP (D1), b) MODIS-Terra c) MODIS-Aqua Comparison (cf., Russo et al., 2010) and cloud brightness temperatures ≤ 210 K from d) GridSat.

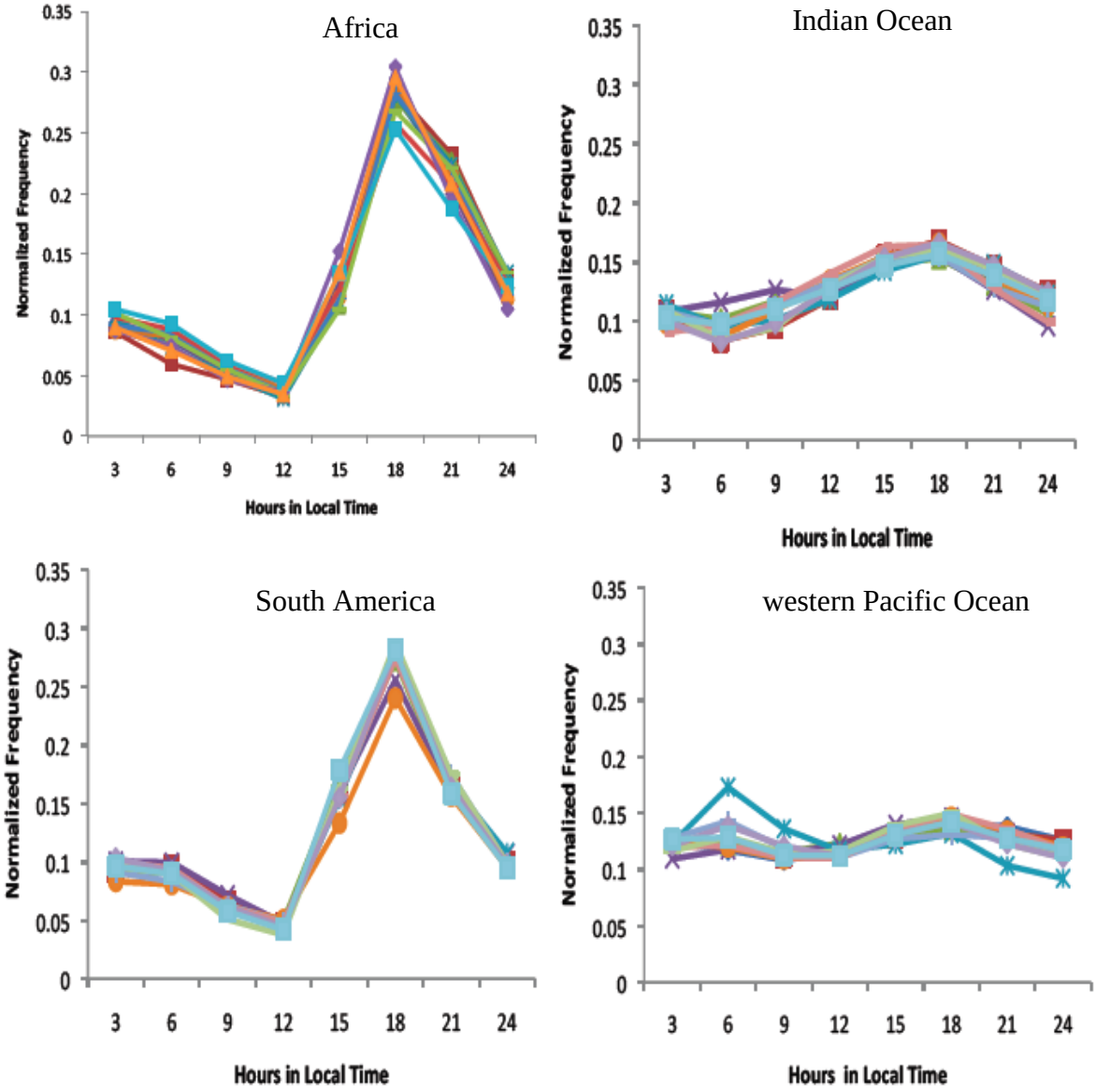

Figure 5.4: Time averaged diurnal cycle per year for tropical regions of Africa, the Indian Ocean, South America, and the western Pacific Ocean.

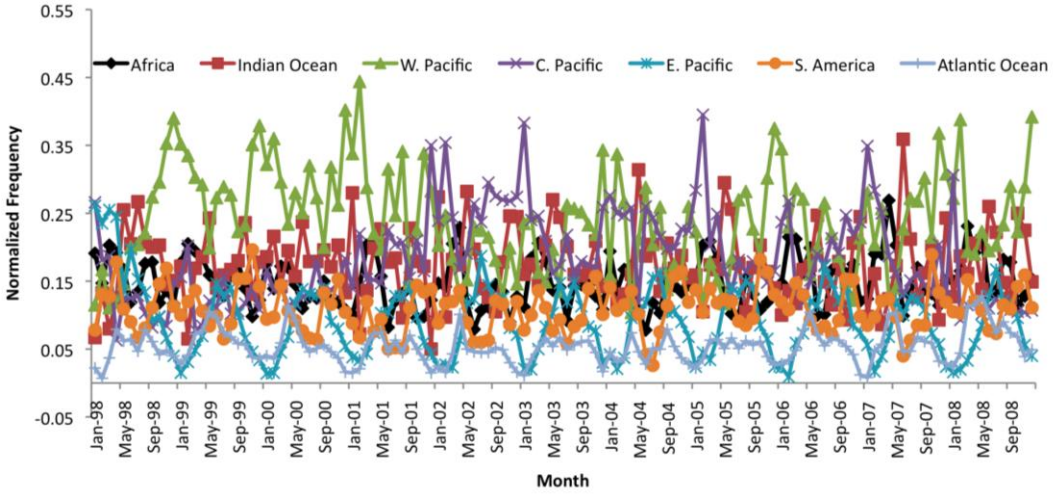

Figure 5.5 Normalized monthly frequency of penetrating tops given for all seven regions within the tropics from January 1998 through December 2008. The Western Pacific Ocean clearly has higher frequencies of penetrating deep convection among all other regions considered.

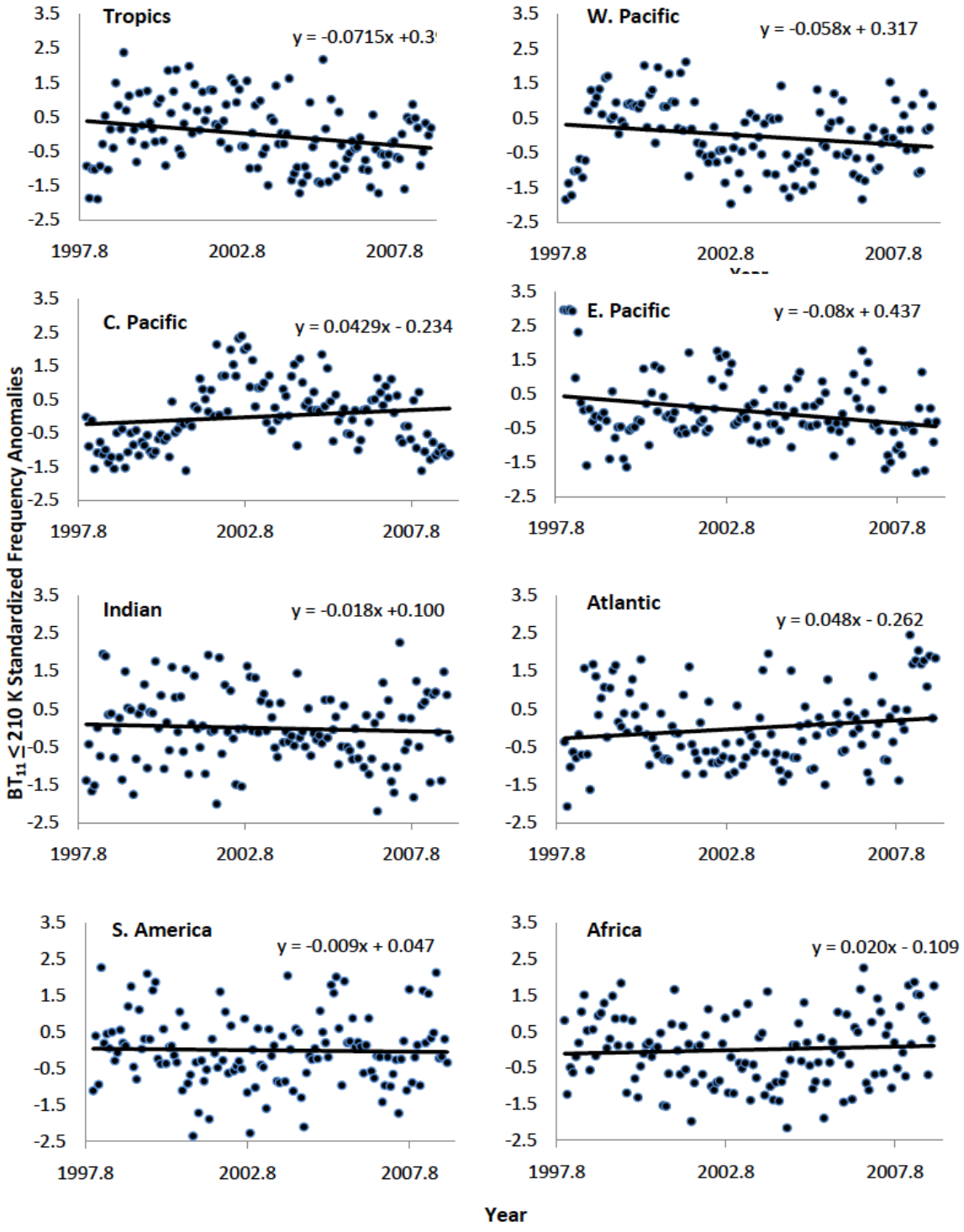

Figure 5.6: Standardized frequency anomalies for a) the Tropics (15°N-15°S) b) Africa c) the Indian Ocean d) the western Pacific Ocean e) central Pacific Ocean f) eastern Pacific Ocean g) South America and h) the Atlantic Ocean.

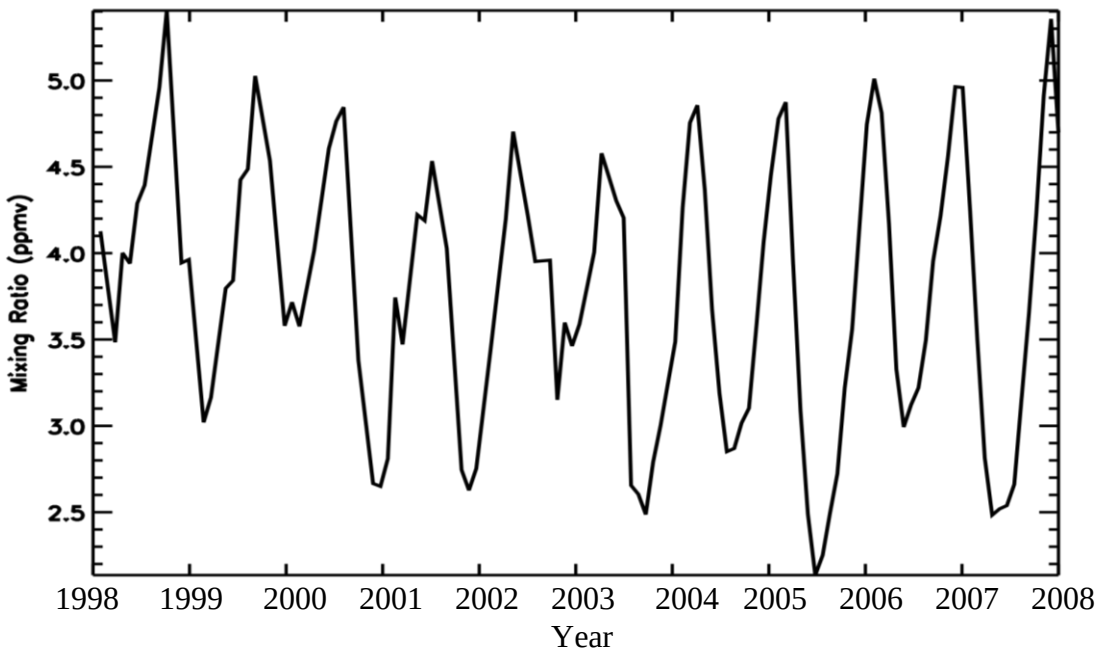

Figure 5.7: 1998-2008 monthly zonal averages of water vapor volume mixing ratio at 82mb and from 15°N-15°S.

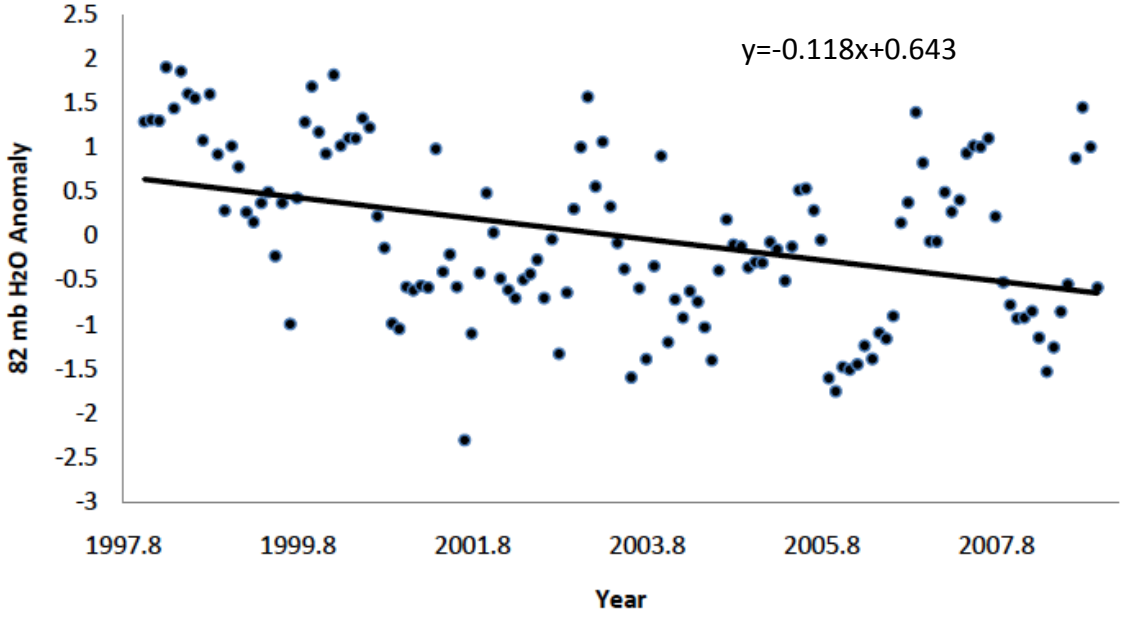

Figure 5.8: 1998-2008 anomalies in 82 mb lower stratospheric water vapor mixing ratio from 15°N-15°S shown with a slightly negative trend.

CHAPTER 6

CONCLUSIONS

This thesis evaluates deep convection penetrating the TTL using radar and IR observations to explore the hypothesis that penetrating and overshooting deep convection has a strong influence on lower stratospheric water vapor variability. More specifically, CloudSat/Calipso and Aqua MODIS observations from 2007 were used to 1) obtain a statistically robust sample of penetrating deep convection and evaluate their areal extent to determine how well penetrating deep convection may be resolved from IR sensors; 2) quantitatively compare IR and radar distributions of penetrating deep convection using traditional IR techniques to determine the extent to which traditional IR techniques capture penetrating deep convection; and 3) given the uncertainty of traditional IR techniques the variability of penetrating and overshooting deep convection is captured from 11 years (1998─2008) of GridSat observations to compare monthly frequency anomalies in penetrating deep convection with anomalies in lower stratospheric water vapor. The main findings are summarized below to specifically address science questions posed in previous chapters.

What new insights on the characteristics of penetrating and overshooting deep convection does CloudSat provide? The normalized frequency distribution of penetrating deep convective clouds from CloudSat is consistent with IR studies. However, the CloudSat distribution does not compare as well with the distribution of penetrating deep convective clouds provided from TRMM, which is based on precipitation size particles. From CloudSat estimates of the areal extent of penetrating deep convection, it is concluded that at a horizontal resolution of 10 km, about two thirds of penetrating deep

convective clouds are large enough to be detected from conventional IR sensors. Examination of the CloudSat data also suggests that penetrating deep convection occurs in the extratropics. CloudSat observations provided important insights into the interpretation IR signatures of penetrating convection. It was shown that penetrating deep convection reaching 14 km shows a range of cloud brightness temperatures > 210 K and all do not exhibit +BTD signatures. However, higher penetrating deep convective clouds consistently have cloud brightness temperatures ≤ 210 K and do exhibit +BTD signatures.

To what extent is penetrating deep convection exclusively captured using traditional IR methods and does this information change the perception of the frequency distribution of penetrating deep convection as presented in other IR studies? Cold cloud features ≤ 210 K and +BTD signatures were sampled along the CloudSat orbital track and compared with independent CloudSat/Calipso observations of penetrating deep convective clouds. This was done to better understand the information content provided from the IR distributions, since IR observations do not directly resolve cloud vertical structure and there has been some debate on their usefulness to characterize observations of penetrating tops. By comparing the IR and radar distributions, it is concluded that neither of the IR schemes completely separates between penetrating deep convection and other types of high clouds. However, the predominant fraction of +BTD signatures and cold cloud features/pixels ≤ 210 K are associated with penetrating tops. This result is in contrast to studies that suggest the majority of cold cloud features/pixels ≤ 210 K are cirrus/anvil cloud fractions that coexist with deep convective clouds.

What are the microphysical and optical properties of penetrating deep convection in comparison with other high level clouds? How does the incorporation of these parameters aide in the evaluation of penetrating deep convective clouds using traditional IR techniques? Since the fraction of cold cloud features ≤ 210 K that are also penetrating tops is so much greater in this analysis compared with previous studies, the optical and microphysical properties of other high level clouds and BT ≤ 210 K observations were analyzed to interpret the conclusions that have been made regarding the IR distributions. Comparison of deep convection, cirrus, anvil clouds and penetrating deep convective clouds showed that while cirrus clouds reside at altitudes similar to penetrating deep convection, their IR brightness temperatures are generally much warmer because they are not as optically thick. Anvil clouds occasionally have cloud brightness temperatures similar to penetrating deep convection. However, single layered anvil clouds rarely have optical depths > 34. The evaluation of all optical depth values corresponding to observations of cold cloud features/pixels ≤ 210 K shows that cloud brightness temperatures ≤ 210 K are predominantly associated with deep convective clouds of rather high optical thickness. This result further substantiates the interpretation that the 210 K cloud field is predominantly associated with deep convective cores and more importantly it does not require the use of radar data.

How well do +BTD signatures and cloud brightness temperatures ≤ 210 K from GridSat compare when diagnosing their ability to observe annual, interannual and diurnal variability of penetrating deep convective clouds? Based on differences in the interannual variations in normalized frequency distributions of +BTD signatures and cloud brightness temperatures ≤ 210 K, it was concluded that cloud brightness

temperatures ≤ 210 K are at present more suitable dataset from which to evaluate the spatiotemporal properties of penetrating deep convective clouds from the GridSat observations due to issues related to the 6.7 μm brightness temperatures.

Do significant trends or patterns of penetrating deep convection exits? If so, how do these trends correspond to changes in lower stratospheric water vapor? The annual and interannual variability of penetrating deep convection was inferred from standardized frequency anomalies in cloud brightness temperatures ≤ 210 K. It has been concluded that the western-central Pacific and Indian Oceans provide the largest contributions to the $BT_{11} \leq 210$ K signal for the entire tropics, followed by Africa, S. America, the Eastern Pacific and Atlantic Ocean. Slightly negative trends occur in the tropics and most other regions between 1998─2008, with the exception of Africa, the central Pacific, and the Atlantic Ocean. However, these trends are not significant at the 95% confidence level and would require much more data to meet this criteria.

The cross-correlation of anomalies in water vapor mixing ratio at 82 mb with monthly anomalies in the frequency of the coldest penetrating tops supports the inference that the strongest and most significant relationships were more consistently observed for lags between 2 – 3 months. At a lag of 3 months, the combined western-central Pacific had a small but significant anticorrelation, where the largest amount of variance explained by the combined western-central Pacific monthly frequency anomalies was 8.25%. This result indicates that events within the western-central Pacific variation dominate the anomalies in the tropical 82 mb water vapor record. In comparison to Tselioudis et al. [2010], it is unclear if similar, stronger or weaker correlations exist when the 82 mb monthly anomalies are analyzed against all deep convection, which Tselioudis et al.

suggests is a more likely mechanism driving stratospheric water vapor variability patterns.

The results of this study are however limited by the characteristics of the evaluated data. For example, CloudSat observations have high vertical and horizontal resolutions. In addition, it is a nadir scanning radar. By scanning such a narrow slice of the atmosphere, CloudSat is unable to observe entire large-scale cloud systems. In addition, the return period or length of its repeat cycle presents difficulties in identifying short-lived deep convective clouds and fully resolving their diurnal cycle. CloudSat's polar orbit minimizes the degree to which it observes the tropics, where penetrating deep convective clouds are most often present. Such limitations may warrant some caution with regard to the interpretation of CloudSat results that have been presented.

For the evaluation of IR properties, limitations arise due to explicit assumptions that have been made with regard to infrared window brightness temperatures at ~11 μm from Aqua MODIS and GridSat. Unfortunately, there are differences in the 11μm central wavelengths, bandwidths, and bit resolutions for Aqua MODIS and GridSat, which present challenges for the intercalibration of multiple geostationary satellites. Another layer of complication arises since observations of low cloud brightness temperatures have fewer matchups of polar and geostationary observations that are used for intercalibration purposes. This means that while CloudSat and Aqua MODIS observations have been explicitly linked via analysis of collocated observations, no such procedure has been presented here to evaluate the consistency between observations from Aqua MODIS and GridSat, nor has this relationship been provided in the referenced literature.

Finally, with regard to observations of water vapor mixing ratio at 82 mb, several

other studies that have analyzed lower stratospheric water vapor anomalies have shown that there is a clear presence of the QBO that is more obvious at higher levels extending away from the tropopause rather than at the tropopause. However, the QBO signal is likely present to some extent at the 82 mb level. Without quantifying the degree to which the QBO signal is present in anomalies of water vapor mixing ratio at 82 mb and modulates these values, the relationship between the frequency in penetrating deep convective clouds and water vapor variability is highly subject to misinterpretation

Comparison of the optical and microphysical properties of penetrating deep convection compared with other types of high clouds in Chapter 3 was only performed for January 2007. The short time period of this part of the analysis leaves some question regarding the representativeness of these results. As shown by Hong and Yang [2007], there is seasonal variability in cirrus and deep convection that is missed when we limit our evaluation to 1 month only. *What would be the outcome of a similar analysis if it were performed over a longer time period or at least for January and July?* Since no other studies have coupled CloudSat observations of vertical cloud structure and followed this process with the retrieval of optical and microphysical properties from Aqua MODIS, a more rigorous analysis of high-level clouds could be performed especially to evaluate the degree to which we may disentangle deep convective cores and surrounding anvil cloud fractions.

With additional regard to the time extent of the evaluations, it is also noted that the atmosphere is highly variable on annual and interannual time scales that are considerably modulated by the El Niño Southern Oscillation. Since the 2007 observations occurred during a moderate La Niña phase, it is also important to ask, *what is the impact*

of weak and strong El Niño and La Niña phases of the Southern Oscillation with regard to the spatiotemporal variability of penetrating deep convective clouds? A multi-year analysis that evaluates El Niño /La Niña impacts on the spatiotemporal variability of penetrating deep convective clouds may also advance our understanding of these phenomena and their impacts.

Other areas where the analysis of lower stratospheric water vapor and/or the impact of penetrating deep convection on lower stratospheric water vapor requires further evaluation includes the following:

- ***Representation of vertical convective transport in models:*** Modeling is used to evaluate our conceptual view of physical processes. Vertical transport in most models is highly parameterized and is evaluated at resolutions that are too coarse for deep convection to be explicitly represented. The evaluation of the representation of tropical deep convection in atmospheric models by Russo et al. [2011] who compare the representation of tropical deep convection to various observational data sets considered to be proxies for deep convection is an excellent basis with which to determine the schemes that are most useful for characterizing vertical transport. Then, modeling of the mass flux into the lowermost stratosphere should be improved.
- ***Cloud thermodynamics and microphysics*****:** A better understanding of cloud thermodynamics and microphysics is a very important as it relates to the regulation of observed quantities such as cloud top height and cloud top temperature. Thermodynamic parameters associated with overshooting

deep convection events and their implications for UT/LS exchange should also be analyzed to statistically characterize and evaluate environmental properties that determine the intensity and depth of penetration into the tropical tropopause layer and lower stratosphere. In addition, ice formation in atmospheric clouds influences the cloud life-cycle, precipitation processes and cloud radiative properties (e.g., Khvorostyanov and Curry, 2009). For deep overshooting convection, ice is specifically important as it participates in hydration/dehydration of the lower stratosphere. The impact of ice formation on cloud buoyancy has been addressed (Brahams, 1952; Riehl, 1979; Zipser, 2003). Yet for deep convection clouds it is rarely included in the evaluation of undilute adiabatic ascent or the analysis of thermodynamic indices designed to diagnose convective available potential energy (e.g., Luo, 2008; Liu and Zipser, 2005). Such analysis may be achieved via a simple one dimensional cloud parcel model. The details of this model are provided in Appendix B.

- ***Improved instruments that can better measure changes in the quantity of water vapor in the lower stratosphere***: There is much uncertainty in the observations of lower stratospheric water vapor since it is present in such small concentrations. To reduce the uncertainty of these measurements more accurate instruments should be developed. For example, in the evaluation of 82 mb water vapor mixing ratio we have used a combination of UARS-HALOE and Aura MLS data. For version 1.51 of the MLS water vapor data, which has an estimated precision of 20% and are reliable

at altitudes above 316 mb. The vertical resolution in the upper troposphere is roughly 3 km and the horizontal resolution is roughly 15° longitude and 1.5° latitude. To better pinpoint the impact of various processes on lower stratospheric water vapor, higher resolution measurements with less uncertainty are needed.

- ***Dehydration processes:*** According to Brewer [1949], all air entering the stratosphere must be freeze-dried near the tropical tropopause, where temperatures are regularly below 195 K. However, according to observations, the stratosphere contains less water than it would if the air entered at the average minimum tropical temperature. Understanding why the stratosphere contains less water than it would if the air entered at the average minimum tropical temperature is still eluding. While several explanations, have evolved there is still little observational evidence to strongly support any of the recently proposed processes. Determining the details of dehydration mechanisms, in conjunction with competing hydration mechanisms, is also an important area of research that remains challenging.

Future work focused on each of these areas, could make considerable contributions to our understanding of penetrating deep convection, the controls of stratospheric water vapor, and our capability to project how stratospheric water vapor may change in a warming climate.

Appendix A

More Details of the 2B-Geoprof Lidar Product

Although the lidar and radar have different vertical and spatial resolutions, the spatial domain of the output products in the 2B-Lidar GEOPROF algorithm is defined in terms of the spatial grid of the CPR, which is represented as some spatial field of probability. Figure A.1 shows a conceptual downward looking view of the spatial field of probability in blue with some number of coincident lidar footprints in red. The solid and dashed circles surrounding the lidar footprints and the solid and dashed ellipses surrounding the radar footprint represent the 1 and 2 standard deviation pointing uncertainty in the CPR and Lidar.

As also shown in Figure A.1, the probability field forms an ellipse whereby the highest probability values within the spatial field are found at the center of the profile and decrease outward from that point. Lidar observations that overlap the spatial region enclosing the 2-sigma boundary of the radar observational domain are considered to contribute to the spatial description of the overlap region. Below 8.2 km, as many as 9-10 separate lidar profiles will be included in the spatial description of the overlap region and above 8.2 km, 3-4 profiles will potentially contribute to the hydrometeor description. The degree to which a lidar observation contributes to a given radar resolution volume is calculated in terms of the degree to which that particular observation contributed to the spatial overlap in the radar observational domain. This calculation is computed using a weighting scheme that is based on the spatial probability of overlap according to:

$$w_i = \int_x \int_y P_r P_l^i \, dx dy \qquad \text{A.1}$$

where *i* counts the lidar profile in a particular radar observational domain, *x* and *y* represent spatial dimensions to form an area enclosing the radar domain, subscripts *r* and *l* represent the radar and lidar, respectively and *P* is the spatial probability that a particular element of area defined by *x* and *y* contributes to the observation. The lidar cloud fraction (C_l) within a radar footprint is expressed as a weighted combination of the lidar observations within the radar probability field according to:

$$C_l = \frac{\sum_{i=l}^{\#lidarobs} w_i \delta_i}{\sum^{\#lidarobs} w_i} \qquad \text{A.2}$$

where δ_i, the lidar hydrometeor occurrence, may have a value of 1, which indicates that hydrometeors exist or it may have a value of 0 which indicates the nonoccurrence of hydrometeor. In calculating C_l the number, *i*, of lidar observations within a particular radar resolution volume is determined by the total number of lidar profiles that could potentially contribute to the radar probability field. This quantity, C_l, effectively quantifies the partial filling of the radar volume by hydrometeors and is one of the output quantities of the radar-lidar combined product.

Here vertically connected CloudSat bins with cloud mask values (≥ 30) define a cloud layer. A layer boundary is defined as the first encounter of a cloudy range level (either radar or lidar) following the occurrence of a cloud-free range level by radar or a cloud range level with a lidar hydrometeor fraction < 0.5.

To illustrate the concept of the lidar hydrometeor fraction see Figure A.2 which denotes hydrometeor fractions by C^{n}_{h} where n denotes a lidar range number and five lidar profiles are included in the radar observational domain. A lidar range is defined as cloudy if the value $C^{n}_{h} \geq 0.5$. This indicates that at least 50% of the lidar profiles within 1 radar range level are cloudy In Figure A.2, the first cloudy layer encountered moving from bottom to top would be the second layer with $C^{2}_{h} \geq 0.6$.

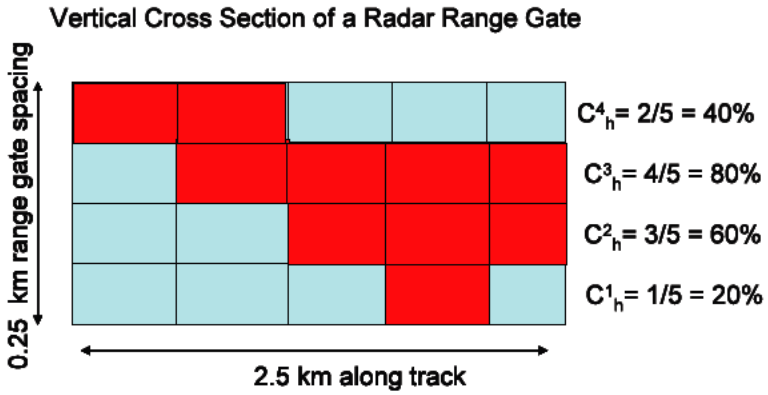

Figure A.1 (cf., Mace et al., 2007) Illustration of lidar hydrometeor fractions, C^n_h, (in red) that occur within a CPR range resolution volume (in blue). Lidar hydrometeor fractions reported for each horizontal level are reported in percentages on the right.

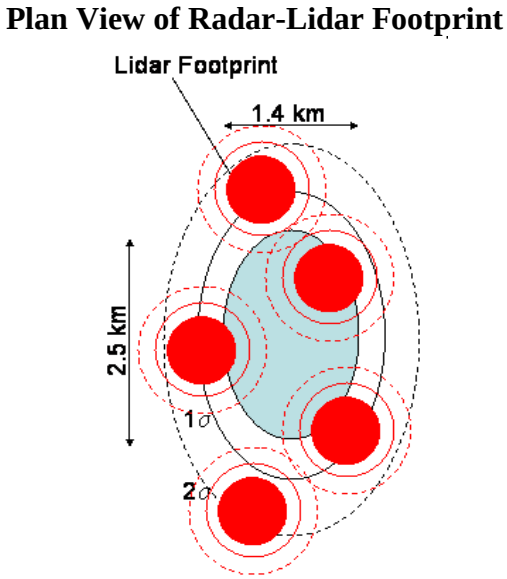

Figure A.2 (cf.,Mace et al., 2007) Conceptual view of CPR-Lidar overlap with radar footprint in blue and lidar footprints in red. The black (red) solid and dashed ellipses (circles) represent the 1 and 2 standard deviation pointing uncertainty of the radar (lidar).

Appendix B

Description of Parcel Model

An unsaturated parcel is assumed to begin its ascent absent of liquid or ice condensate. The parcel is raised from the surface in 1mb increments. For temperatures above freezing, the parcel maintains at an RH=100% and is not allowed to become supersaturated with respect to liquid (or ice). Liquid condensate is formed by converting any excess moisture above saturation with respect to liquid to liquid water according to,

$$\Delta r_v = \Delta r_{vsl} = -\Delta r_l \quad \text{B.1}$$

where r_v is the water vapor mixing ratio, r_{vsl} is the saturation mixing ratio with respect to liquid water, and r_l is the liquid water mixing ratio. At temperatures between 273.15 and 238.15 K, condensation is calculated using a modified version of the theoretical ice nucleation scheme proposed by ECMWF [2007]. The ECMWF formulation and its modifications characterize the phase state in clouds in effort to parameterize the liquid, f_l, and ice fractions, f_i, of the total condensate. The result of this formulation shows that in pure liquid clouds with warm temperatures slightly above 0 °C, f_l is observed to be close to 100 %. In the case of cold clouds where temperatures decline below T < -35 to – 40 °C clouds become purely crystalline [Borovikov et al., 1963; Pruppacher and Klett, 1997]. For the ECMWF [2007] scheme, the fraction of liquid condensate, f_l is calculated

$$f_l = [(T - T_{ice})/(T_0 - T_{ice})]^2 \quad \text{B.2}$$

and the fraction of ice condensate, f_i, is calculated,

$$f_i = 1 - f_l \qquad \text{B.3}$$

where, $f_l = 0$ at $T < T_{ice}$,, $T_0 = 273.16$ and T_{ice} has been modified from the ECMWF (2007) value of 250.16 K to 238.15 K. This modification better corresponds with the climatology of ice and liquid fractions presented by Borovikov et al. [1963] and Pruppacher and Klett [1997], ensuring that the cloud parcel is not fully glaciated until temperatures decline below -35°C. The fractions of liquid and ice phase states are shown in Figure B.1. Note, the conditions $0 \leq f_l \leq 1$ and $0 \leq fi \leq 1$ are both strictly enforced.

The mixing ratios of water vapor, ice, and liquid water are then diagnosed by the following

$$r_v = F_l r_{vsl} + F_i r_{vsi} \qquad \text{B.4}$$
$$r_i = F_i (r_t - r_v) \qquad \text{B.5}$$
$$r_l = r_t - r_v - r_i \qquad \text{B.6}$$

where saturations with respect to liquid water and ice, r_{vsl} and r_{vsi} are calculated according to, $r_{vsl} = \frac{\varepsilon e_{sl}}{p - e_{sl}}$ and $r_{vsi} = \frac{\varepsilon e_{si}}{p - e_{si}}$ and e_{sl} was fit to Wexler's results, extrapolated for $T <$ *0 ℃*, to an accuracy of 0.1% for *-30 ℃* $\leq T \leq$ *35 ℃* and e_{si} is calculated using the formulation [Bolton, 1980],

$$e_s(T) = 6.112 \exp\left(\frac{17.67}{T + 243.5}\right) \qquad \text{B.7}$$

and e_{si} is calculated using [Marti and Mauersberger, 1993]

$$e_{si}(T) = (10\text{^}(-2663.5/T) + 12.537)/100. \qquad \text{B.8}$$

The model is further constrained according to the ice liquid water potential temperature defined by Tripolli and Cotton [1981] as

$$\vartheta_{il} = \vartheta\left[1 + \frac{L_v(T_0)r_l}{c_p \max(T,253)} + \frac{L_s(T_0)r_i}{c_p \max(T,253)}\right]^{-1} \qquad \text{B.9}$$

θ_{il}, represents reversible adiabatic ascent and is conserved under vapor to liquid, vapor to ice, and liquid to ice phase changes. For pseudoadiabatic ascent, we use Bolton [1980], substituting the latent heat of sublimation for that of vaporization when necessary and also in fractions consistent with f_l and f_i. At temperatures below 238.15 K, supersaturation with respect to ice is not allowed. Ice condensate is formed by converting any excess moisture above saturation with respect to ice to ice according to

$$\Delta r_v = \Delta r_{vsi} = \Delta r_i \qquad \text{B.10}$$

As the parcel is lifted, the vertical temperature profile of the cloud is determined by solving the model equations (B1-B10) using the Broyden method of solving simultaneous nonlinear systems of equations.

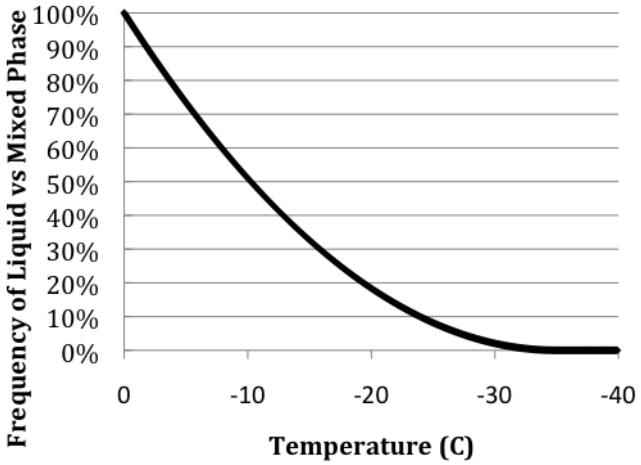

Figure B.1. Frequency of Liquid versus Mixed Phase states using modified version of ECMWF [2007]. At temperatures above 0°C the cloud condensate is all liquid water. Between 0°C and -35°C condensate is a mixture of ice and liquid water. At temperatures below -35°C the cloud is fully glaciated.

References

Adler, R. F., and R. A. Mack (1986), Thunderstorm cloud top dynamics as inferred from satellite observations and a cloud top parcel model, *J. Atmos. Sci.*, *43*, 1945–1960.

Alcala, C. M., and A. E. Dessler (2002), Observations of deep convection in the tropics using the Tropical Rainfall Measuring Mission (TRMM) precipitation radar, *J. Geophys. Res.*, *107*, 4792, doi:10.1029/2002JD002457.

Aumann, H. H., S. G., DeSouza–Machado, and A. Behrangi (2011), Deep convective clouds at the tropopause, *Atmos. Chem. Phys.*, *11*, 1167–1176.

Bain, C. L., G. Magnusdottir, P. Smyth, and H. Stern, 2010: Diurnal cycle of the Intertropical Convergence Zone in the east Pacific. *Journal of Geophysical Research*, **115,** D23116.

Barrett, E. W., P. M. Kuhn, and A. Shlanta, (1973), Recent measurements of the injection of water vapor and ozone into the stratosphere by thunderstorms, paper presented at Second Conference on the Climatic Impact Assessment Program, Department of Transportation, Washington D. C.

Battaglia, A., and C. Simmer (2008), How does multiple scattering affect the spaceborne W-band radar measurements at ranges close to and crossing the surface-range?, *IEEE Trans. Geosci. Remote Sens.*, *46*, 1644–1651.

Bedka, K. M., and P. Minnis (2010), GOES 12 observations of convective storm variability and evolution during the Tropical Composition, Clouds and Climate Coupling Experiment field program, *J. Geophys. Res.*, *115*, D00J13, doi:10.1029/2009JD013227.

——, J. Brunner, R. Dworak, W. Feltz, J. Otkin, and T. Greenwald (2010), Objective satellite-based detection of overshooting tops using infrared window channel brightness temperature gradients, *J. Appl. Meteorol. Climatol.*, *49*, 181–202.

Berendes, T. A., J. R. Mecikalski, W. M. MacKenzie, Jr., K. M. Bedka, and U. S. Nair (2008), Convective cloud identification and classification in daytime satellite imagery using standard deviation limited adaptive clustering, *J. Geophys. Res.*, *113*, D20207, doi:10.1029/2008JD010287.

Boering, K. A., E. J. Hintsa, S. C. Wofsy, J. G. Anderson, B. C. Daube, A. E. Dessler, M. Loewenstein, M. P. McCormick et al. (1995), Measurements of stratospheric carbon dioxide and water vapor at northern latitudes: Implications for stratosphere-to-troposphere transport. *Geophys. Res. Lett.*, *22*, 2737–2740.

Bolton, D. (1980), The computation of equivalent potential temperature, *Mon. Weather Rev.*, *108*, 1046–1053.

Borovikov, A. M., I. I. Gaivoronsky, E. G. Zak, V. V. Kostarev, I. P. Mazin, V. E. Minervin, A. Kh. Khrigian, and S. M. Schmeter (1963), *Cloud Physics*, Leningrad, Hydrometeoizdat, (1961), Transl. by Israel Program Scientif. Translation, U. S. Dept. Commerce, Washington, DC, 392 pp.

Borsche, M., G. Kirchengast, and U. Foelsche (2007), Tropical tropopause climatology as observed from radio occultation measurements from CHAMP compared with ECMWF and NCEP, *Geophys. Res. Lett., 34*, L03702, doi:10.1029/2006GL027918.

Brewer, A. W. (1949), Evidence for a world circulation provided by the measurements of helium and water vapour distribution in the stratosphere, *Q. J. R. Meteorol. Soc. 75*, 351–363.

Brunner, J. C., S. A. Ackerman, A. S. Bachmeier, and R. M. Rabin (2007), A quantitative analysis of the enhanced-V feature in relation to severe weather, *Weather Forecast., 22*, 853–872.

Chaboureau, J. P., J. P Cammas, J. Duron, P. J. Mascart, N. M. Sitnikov, and H. J. Voessing (2007), A numerical study of tropical cross-tropopause transport by convective overshoots, *Atmos. Chem. Phys, 7*, 1731–1740.

Chen, T., W. B. Rossow, and Y. Zhang (2000), Radiative effects of cloud-type variations, *J. Climate, 13*, 264–286.

Chou, C., and J. D. Neelin (1999), Cirrus detrainment-temperature feedback. *Geophys. Res. Lett., 26*, 1295–1298.

Chung, E. S., B. J. Sohn, and J. Schmetz (2008), CloudSat shedding new light on high reaching tropical deep convection observed with Meteosat, *Geophys. Res. Lett. 35*, L02814, doi:10.1029/2007GL032516.

Corti, T., B. P. Luo, Q. Fu, H. Vömel, and T. Peter (2006), The impact of cirrus clouds on tropical troposphere-to-stratosphere transport, *Atmos. Chem. Phys, 6*, 2539–2547.

——, B. P. Luo, M. de Reus, D. Brunner, F. Cairo, M. J. Mahoney, G. Martucci, R. Matthey et al. (2008), Unprecedented evidence for deep convection hydrating the tropical stratosphere, *Geophys. Res. Lett. 35*, L10810, doi:10.1029/2008GL033641.

Danielsen, E. F. (1982), A dehydration mechanism for the stratosphere, *Geophys. Res. Lett., 9*, 605–608.

—— (1993), In situ evidence of rapid, vertical, irreversible transport of lower tropospheric air into the lower tropical stratosphere by convective cloud turrets

and by larger-scale upwelling in tropical cyclones, *J. Geophys. Res*., *98*, 8665–8681.

Dessler, A. E. (2002), The effect of deep, tropical convection on the tropical tropopause layer, *J. Geophys. Res*., *107*(D3), doi:10.1029/2001JD000511.

—— and S. C. Sherwood (2003), A model of HDO in the tropical tropopause layer. *Geophys. Res. Lett., 31*, 2173–2181.

Donner, L. J., C. J. Seman, R.S. Hemler, and S. Fan (2001), A cumulus parameterization including mass fluxes, convective vertical velocities, and mesoscale effects: Thermodynamic and hydrological aspects in a general circulation model, *J. Climate, 14*, 3444–3463.

——, L. W. Horowitz, A. M. Fiore, C. J. Seman, D. R. Blake, and N. J. Blake (2007), Transport of radon-222 and methyl iodide by deep convection in the GFDL Global Atmospheric Model AM2, *J. Geophys. Res., 112*, D17303, doi:10.1029/2006JD007548.

Folkins, I., and R. V. Martin (2004), The vertical structure of tropical convection and its impact on the budgets of water vapor and ozone, *J. Atmos. Sci*., *62*,1560–1573.

——, M. Loewenstein, J. Podolske, S. J. Oltmans, and M. Proffitt (1999), A barrier to vertical mixing at 14 km in the tropics: Evidence from ozonesondes and aircraft measurements, *J. Geophys. Res., 104*, 22,095–22,102.

Forster, P. M. F., and K. P. Shine (1999), Stratospheric water vapour changes as a possible contributor to observed stratospheric cooling, *Geophys. Res. Lett., 26*, 3309–3312.

——, and K. P. Shine (2002), Assessing the climate impact of trends in stratospheric water vapor, *Geophys. Res. Lett, 29*, 6, doi:10.1029/2001GL013909.

Fritz., S., and I. Laszlo (1993), Detection of water vapor in the stratosphere over very high clouds in the tropics, *J. Geophys. Res., 98*, 22,959–22,967.

Fu, R., A. D. Del Genio, and W. Rossow (1990), Behavior of deep convective clouds in the tropical Pacific deduced from ISCCP radiances, *J. Climate, 3*, 1129–1152.

Fueglistaler, S., A.E. Dessler, T. Dunkerton, I. Folkins, Q. Fu, P.W. Mote (2009), Tropical Tropopause Layer, *Rev. Geophys*., 47, RG1004, doi:10.1029/2008RG000267.

——, and P. H. Haynes (2005), Control of interannual and longer-term variability of stratospheric water vapor, *J. Geophys. Res., 110*, D24108, doi:10.1029/2005JD006019.

——, H. Wernli, and T. Peter (2004), Tropical troposphere-to-stratosphere transport inferred from trajectory calculations, *J. Geophys. Res., 109*, D03108, doi:10.1029/2003JD004069.

Fujita, T. T. (1982), Principle of stereoscopic height computations and their applications to stratospheric cirrus over severe thunderstorms, *J. Meteor. Soc. Japan, 60*, 355–368.

Gettelman, A., M. L. Salby, and F. Sassi (2002), Distribution and influence of convection in the tropical tropopause region, *J. Geophys. Res., 107*, 4080, doi:10.1029/2001jd001048.

——, E. J. Fetzer, A. Eldering, and F. W. Irion (2006), The global distribution of supersaturation in the upper troposphere from the atmospheric infrared sounder, *J. Climate*, *19*, 6089–6103.

——, T. Birner, V. Eyring, H. Akiyoshi, S. Bekki, C. Brühl, M. Dameris, D. E. Kinnison et al. (2009), The tropical tropopause 1960-2100, *Atmos. Chem. Phys.*, *9*, 1621–1637.

——, M. I. Hegglin, S.-W. Son, J. Kim, M. Fujiwara, T. Birner, S. Kremser, M. Rex et al. (2010), Multi-model assessment of the upper troposphere and lower stratosphere: Tropics and global trends, *J. Geophys. Res.*, *115*, D00M08, doi:10.1029/2009JD013638.

Gierens, K., R. Kohlhepp, P. Spichtinger, and M. Schroedter-Homscheidt (2004), Ice supersaturation as seen from TOVS. *Atmos.Chem. Phys.*, *4*, 539–547.

Gould-Stewart, R. E. N. a. S. (1981), A stratospheric rountain?, *J. Atmos. Sci.*, *38*, 2789–2796.

Grosvenor, D. P., T. W. Choularton, H. Coe, and G. Held (2007), A study of the effect of overshooting deep convection on the water content of the TTL and the lower stratosphere from cloud resolving model simulations, *Atmos. Chem. Phys. Discuss.*, *7*, 7277–7346.

Hansen, J., M. Sato, R. Ruedy, L. Nazarenko, A. Lacis, G. A. Schmidt, G. Russell, I. Aleinov et al. (2005), Efficacy of climate forcings, *J. Geophys. Res.*, *110*, D18104, doi:10.1029/2005JD005776.

Hartmann, D.L., M. E. Ockert-Bell, and M. L. Michelsen (1992), The effect of cloud type on Earth's energy balance: global analysis. *J. Climate*, *5*, 1281–1304.

Heymsfield, A. J. (1993), Microphysical structures of stratiform and cirrus clouds, in *Aerosol-Cloud-Climate Interactions*, edited P. V. Hobbs, pp. 97–122, Academic

Press, New York.

Heymsfield, G. M., R. Fulton, and J. D. Spinhirne (1991), Aircraft overflight measurements of midwest severe storms: Implications on geosynchronous satellite interpretations, *Mon. Weather Rev.*, *119*, 436–456.

Highwood, E. J., and B. B. Hoskins (1998), The tropical tropopause, *Q. J. Roy. Meteorol. Soc.*, *124*, 1579–1604.

Holton, J. R., and A. Gettelman (2001), Horizontal transport and the dehydration of the stratosphere, *Geophys. Res. Lett.*, *28*, 2799–2802.

——, P.H. Haynes, M. E. McIntyre, A. R. Douglass, R. B. Rood, and L. Pfister (1995), Stratosphere-troposphere exchange, *Rev. Geophys.*, *33*, 403–439.

Hong, G., G. Heygster, J. Miao, and K. Kunzi (2005), Detection of tropical deep convective clouds from AMSU-B water vapor channels measurements, *J. Geophys. Res.*, *110*, D05205, doi:10.1029/2004JD004949.

——, G. Hyegster, and C. A. M. Rodriguez (2006), Effect of cirrus clouds on the diurnal cycle of tropical deep convective clouds, *J. Geophys. Res*., 111, D06209, doi:10.1029/2005JD006208.

——, P. Yang, B. C. Gao, B. A., Baum, Y. X. Hu, M. D. King, and S. Platnick (2007), High cloud properties from three years of MODIS terra and aqua collection-4 data over the tropics, *J. Appl. Meteorol. Climatol*., *46*, 1840–1856.

Intergovernmental Panel on Climate Change (IPCC) (2007), *Climate Change 2007: The Physical Science Basis*, edited by S. Solomon et al., Cambridge Univ. Press, New York.

Jensen, E., and L. Pfister (2004), Transport and freeze-drying in the tropical tropopause layer, *J. Geophys. Res., 109*, D02207, doi:10.1029/2003JD004022.

Jiang, J. H., B. Wang, K. Goya, K. Hocke, S. G. Eckermann, J. Ma, D. L. Wu, and W. G. Read (2004), Geographical distribution and interseasonal variability of tropical deep convection: UARS MLS observations and analyses, *J. Geophys. Res., 110*, D05205, doi:10.1029/2004JD03756.

Johnston, H. S., and S. Solomon (1979), Thunderstorms as possible micrometeorological sink for stratospheric water, *J. Geophys. Res., 84*, 3155–3158.

Kahn, B. H., M. T. Chahine, G. L. Stephens, G. G. Mace, R. T. Marchand, Z. Wang, C. D. Barnet, A. Eldering et al. (2008), Cloud type comparisons of AIRS, CloudSat, and CALIPSO cloud height and amount, *Atmos. Chem. Phys*., *8*, 1231–1248.

Khaykin, S., J.-P. Pommereau, L. Korshunov, V. Yushkov, J. Nielsen, N. Larsen, T. Christensen, A. Garnier et al. (2009), Hydration of the lower stratosphere by ice crystal geysers over land convective systems, *Atmos. Chem. Phys*., *9*, 2275–2287.

Khvorstyanov, V. I., and J. A. Curry (2009), Critical humidities of homogeneous and heterogeneous ice nucleation: Inferences from extended classical nucleation theory, *J. Geophys. Res*., *114*, D04207, doi: 10.1029/2008JD011197.

Kirk-Davidoff, D. B., E. J. Hintsa, J. G. Anderson, and D. W. Keith (1999), The effect of climate change on ozone depletion through changes in stratospheric water vapour, *Nature, 402*, 399–401.

Kley, D., J. M. Russell, and C. Phillips (2000), SPARC assessment of upper tropospheric and stratospheric water vapour, *WCRP Report No. 113, WMO/TD Report No. 1043*, World Climate Research Programme, Geneva.

Knapp, K. R. (2008a), Calibration of long-term geostationary infrared observations using HIRS, *J. Atmos. Oceanic Technol., 25*, 183–195.

—— (2008b), Scientific data stewardship of international satellite cloud climatology project B1 global geostationary observations, *J. Appl. Remote Sensing*, *2*(023458), doi: 10.1117/1.3043461.

Knollenberg, R. G., K. Kelly, and J. C. Wilson (1993), Measurements of high number densities of ice crystals in the tops of tropical cumulonimbus, *J. Geophys. Res.*, *98*(D5), 8639–8664.

Kossin, J. P., K. R. Knapp, D. J. Vimont, R. J. Murnane, and B. A. Harper, 2007a: A globally consistent reanalysis of hurricane variability and trends. *Geophysical Research Letters*, **34,** L04815.

Kubar, T., D. L. Hartmann, and R. Wood (2007), Radiative and convective driving of tropical high clouds, *J. Climate, 20*, 5510–5517.

Li, W., and C. Schumaker (2010), Thick anvils as viewed by the TRMM precipitation radar, *J. Climate*, *24*, 1718–1735.

Liu, C., and E. J. Zipser (2005), Global distribution of convection penetrating the tropical tropopause, *J. Geophys. Res., 110*, D23104, doi:10.1029/2005JD006063.

——, E. J. Zipser, and S. W. Nesbitt (2007), Global distribution of tropical deep convection: Different perspectives from TRMM infrared and radar data, *J. Climate, 20*, 489–503.

Liu, X. M., E. D. Rivière, V. Marécal, G. Durry, A. Hamdouni, J. Arteta, and S. Khaykin

(2010), Stratospheric water vapour budget and convection overshooting the tropopause: modeling study from SCOUT-AMMA, *Atmos. Chem. Phys.*, *10*, 8267–8286.

Luo, Z., G. Y. Liu, and G. L. Stephens (2008), CloudSat adding new insight into tropical penetrating convection, *Geophys. Res. Lett*., *35*, L19819, doi:10.1029/2008GL035330.

——, G. Y. Liu, and G. L. Stephens (2010), Use of A-Train data to estimate convective buoyancy and entrainment rate, *Geophys. Res. Lett*., *37*, L09804, doi:10.1029/2010GL042904.

Mapes, B. E., and R. A. J. Houze (1993), Cloud clusters and superclusters over the oceanic warm pool, *Mon. Weather Rev., 121*, 1398–1415.

Marti, J., and K. Mauersberger (1993), A survey and new measurements of ice vapor pressure at temperatures between 170 and 250 K, *Geophys. Res. Lett*., *20*, 363–366.

Murphy, D. M., and T. Koop (2005), Review of the vapor pressures of ice and supercooled water for atmospheric applications, *Q. J. R. Meteorol. Soc*., *131*, 1539–1565.

Nesbitt, S., E. Zipser, and D. Cecil (2000), A census of precipitation features in the Tropics using TRMM: Radar, ice scattering, and lightning observations, *J. Climate*, *13*, 4087–4106.

Oltmans, S., H. Vömel, D. Hoffman, K. Rosenlof, and D. Kley (2000), The increase in lower-stratospheric water vapor from balloon-borne frostpoint hygrometer measurements at Washington, D. C. and Boulder, Colorado, *Geophys. Res. Lett*., *27*, 3453–3456.

Pruppacher, H. R., and J. D. Klett (1997), *Microphysics of Clouds and Precipitation*, 2nd ed., Kluwer, Norwell, Mass.

Randel, W. J., F. Wu, S. J. Oltmans, K. Rosenlof, and G. E. Nedoluha (2004), Interannual variability of stratospheric water vapor and correlations with tropical tropopause temperatures, *J. Atmos. Sci*., *61*, 2133–2148.

——, F. Wu, H., Vömel, G. E. Nedoluha, and P. Forster (2006), Decreases in stratospheric water vpaor after 2001: Links to changes in the tropical tropopause and the Brewer Dobson circulation, *J. Geophys. Res*., *111*, D12312, doi:10.1029/2005JD006744.

Read, W. G., D. L. Wu, J. W. Waters, and H. C. Pumphrey (2004), Dehydration in the tropical tropopause layer: Implications from the UARS Microwave Limb Sounder, *J. Geophys. Res, 109*, (D06110), doi:10.1029/2003JD004056.

Riehl, H. (1979), *Climate and Weather in the Tropics*, Academic Press, London.

Roca, R., M. Viollier, L. Picon, and M. Desbois (2002), A multisatellite analysis of deep convection and its moist environment over the Indian Ocean during the winter monsoon, *J. Geophys. Res*., *107*, 8012, doi:10.1029/2000JD000040.

Röckmann, T., J. Grooss, and R. Muller (2004), The impact of anthropogenic chlorine emissions, stratospheric ozone change and chemical feedbacks on stratospheric water, *Atmos. Chem. Phys*., *4*, 693–699.

Rohs, S., C. Schiller, M. Riese, A. Engel, U. Schmidt, U. Wetter, I. Levin, T. Nakazawa, and S. Aoki (2006), Long-term changes of methane and hydrogen in the stratosphere in the period 1978-2003 and their impact on the abundance of stratospheric water vapor, *J. Geophys. Res.*, *111*, D14315, doi:10.1029/2005JD00687.

Rosenlof, K. H. (2003), How water enters the stratosphere, *Science*, *302*, 1691–1692.

——, and G. C. Reid (2008), Trends in the temperature and water vapor content of the tropical lower stratosphere: Sea surface connection, *J. Geophys. Res*., *113*, D06107, doi:10.1029/2007JD009109.

——, S. J. Oltmans, D. Kley, J. M. Russell, E. W. Chiou, W. P. Chu, D. G. Johnson, K. K. Kelly et al. (2001), Stratospheric water vapor increases over the past half-century, *Geophys. Res. Lett.*, *28*, 1195–1198.

Rossow, W. B., and C. Pearl (2007), 22-Year survey of tropical convection penetrating into the lower stratosphere, *Geophys. Res. Lett.*, *34*, L04803, doi:10.1029/2006GL028635.

——, and R. A. Schiffer (1999), Advances in understanding clouds from ISCCP, *Bull. Amer. Meteorol. Soc*., *80*, 2261–2287.

——, G. Tselioudis, A. Polak, and C. Jakob (2005), Tropical climate described as a distribution of weather states indicated by distinct mesoscale cloud property mixtures, *Geophys. Res. Lett*., *32*, L21812, doi:10.1029/2005GL024584.

Russell, J. M, L. Gordley, J. H. Park, S. R. Drayson, W. D. Hesketh, R. J. Cicerone, A. F. Tuck, J. E. Frederick et al. (1998), The halogen occultation experiment, *J. Geophys. Res.*, *98* (D6), 10,777–10,797.

Sassen, K., and Z. Wang, (2008), Classifying clouds around the globe with the CloudSat

radar: 1-year of results. *Geophys. Res. Lett., 35*, L04805, doi:10.1029/2007GL032591.

Schiffer, R. A., and W. B. Rossow (1999), ISCCP global radiance data set: A new resource for climate research, *Bull. Amer. Meteorol. Soc., 66*, 1498–1505.

Schmetz, J., S. A. Tjemkes, M. Gube, and L. van de Berg (1997), Monitoring deep convection and convective overshooting with METEOSAT, *Adv. Space Res., 19*, 433–441.

Setvák, M., and R. M. Rabin (2003), MODIS observations of deep convective cloud tops, paper presented at 2003 EUMETSAT Meteorological Satellite Conference, Weimar, Germany, <http://www.chmi.cz/meteo/sat/setvak/pub_ms.html>

——, R. M. Rabin, and P. K. Wang (2007), Contribution of the MODIS instrument to observations of deep convection storms and stratospheric moisture detection in GOES and MSG imagery, *Atmos. Res. 83*, 505–518.

Sherwood, S. C., and A. E. Dessler (2000), On the control of stratospheric humidity, *Geophys. Res. Lett., 27*, 2513–2516.

——, J.-H. Chae, P. Minnis, and M. McGill (2004), Underestimation of deep convective cloud tops by thermal imagery, *Geophys. Res. Lett., 31*, L11102, doi:10.1029/2004GL019699.

Shindell, D. T. (2001), Climate and ozone response to increased stratospheric water vapour, *Geophys. Res. Lett., 28*, 179–182.

——, G. Faluvegi, N. Bell, and G. Schmidt (2005), An emissions–based view of climate forcing by methane and tropospheric ozone, *Geophys. Res. Lett., 32*, L04803, doi:10.1029/2004GL021900

Smith, C. A., J. D. Haigh, and R. Toumi (2001), Radiative forcing due to trends in stratospheric water vapour, *Geophys. Res. Lett., 28*, 179–182.

Soden, B. J. (2000), Diurnal cycle of convection, clouds, and water vapor in the tropical upper troposphere, *Geophys. Res. Lett., 27*, 2173–2176.

Sohn, B. J., and J. Schmetz (2004), Water vapor-induced OLR variations associated with high cloud changes over the Tropics: A study from Meteosat-5 observations. *J. Climate, 17*, 1987–1996.

Solomon, S., K. Rosenlof, R. Portmann, J. Daniel, S. Davis, T. Sanford, and J. Plattner (2010), Contributions of stratospheric water vapor to decadal changes in the rate of global warming, *Science, 327*, 1219–1223.

Spichtinger, P., K. Gierens, and W. Read (2003), The global distribution of ice supersaturated regions as seen by the Microwave Limb Sounder. *Q. J. R. Meteor. Soc., 129,* 3391–3410.

SPARC (2000), Assessment of upper tropospheric and stratospheric water vapour, *WMO/TD No. 1043, (SPARC Report #2),* Geneva.

Stephens, G. L., D. G. Vane, S. Tanelli, E. Im, S. Durden, M. Rokey, D. Reinke, P. Partain et al. (2008), The CloudSat Mission: Performance and early science after the first year of operation, *J. Geophys. Res., 113,* D00A18, doi:10.1029/2008JD009982.

Stuber, N., M. Ponater, and R. Sausen (2001), Is the climate sensitivity to ozone perturbations enhanced by stratospheric water vapor feedback?, *Geophys. Res. Lett., 28,* 2887–2890.

Tripoli, G. J., and W. R. Cotton (1981), The use of ice-liquid water potential temperature as a thermodynamic variable in deep atmospheric models. *Mon. Weather Rev., 109,* 1094–1102.

Tselioudis, G., E. Tromeur, W. B. Rossow, and C. S. Zerefos (2010), Decadal changes in tropical convection suggest effects on stratospheric water vapor, *Geophys. Res. Lett., 37,* L14806, doi: 0.1029/2010GL044092.

Wang, P. K. (2003), Moisture plumes above thunderstorm anvils and their contributions to cross tropopause transport of water vapor in midlatitudes, *J. Geophys. Res., 108,* 4194, doi:10.1029/2003JD002581.

—— (2004), A cloud model interpretation of jumping cirrus above storm top, *Geophys. Res. Lett., 31,* L18106. doi:10.1029/2004GL020787.

—— (2007), The thermodynamic structure atop a penetrating convective thunderstorm. *Atmos. Res., 83,* 254–262.

——, M. Setvák, W. Lyons, W. Schmid, and H. Lin (2009), Further evidences of deep convective vertical transport of water vapor through the tropopause, *Atmos. Res., 94,* 400–408.

Wang, Z., and K. Sassen (2007), Level 2 cloud scenario classification product process description and interface control document, Version 5.0, 50 pp., <http://www.cloudsat.cira.colostate.edu/ dataICDlist.php?go=list&path=/2B-CLDCLASS>

Waters, J. W., L. Froidevaux, R. S Harwood, R. F. Jarnot, H. M. Pickett, W. G. Read, P. H. Siegel, R. E. Cofield et al. (2006), The Earth Observing System Microwave

Limb Sounder (EOS MLS) on the Aura satellite, *IEEE Trans. Remote Sens*., *44*, 1075–1092.

Webster, P. J., and H. Chang (1988), Equatorial energy accumulation and emanation regions: Impacts of a zonally varying basic state, *J. Atmos. Sci.*, *45*, 803–829.

——, G. J. Holland, J. A. Curry, and H.-R. Chang (2005), Changes in tropical cyclone number, duration, and intensity in a warming environment, *Science*, *309*, 1844–1846.

Weisz, E., J. Li, W. P. Menzel, A. K. Heidinger, B. H. Kahn, and C.-Y. Liu (2007), Comparison of AIRS, MODIS, CloudSat and CALIPSO clout top height retrievals, *Geophys. Res. Lett*., *34*, L17811, doi:10.1029/2007GL030676.

Yuan, J., and R. A. Houze, Jr., and A. Heymsfield (2011), Vertical structures of anvil clouds of tropical mesoscale convective systems observed by CloudSat, *J. Atmos. Sci.*, doi:10.1175/2011JAS3687.1, in press.

——, and R. A. Houze, Jr. (2010), Global variability of mesoscale convective system anvil structure from A-Train satellite data, *J. Climate*, *23*, 5864–5888.

Yuan, T., and Z. Li (2010), General macro- and microphysical properties of deep convective clouds as observed by MODIS, *J. Climate*, *23*, 3457–3473.

Zipser, E. J. (2003), Some view on "hot towers" after 50 years of tropical field programs and two years of TRMM data, in *Cloud Systems Hurricanes, and the Tropical Rainfall Measuring Mission (TRMM)*, edited by W.-K. Tao and R. Adler, *Meteorol. Monogr.*, *29*, 49–58.

——, D. J. Cecil, C. Liu, S. W. Nesbitt, and D. P. Yorty (2006), Where are the most intense hurricanes on Earth?, *Bull. Am. Meteorol. Soc*., *87*, 1057–1071.